I. Equation of State of Molten Mid-Ocean Ridge Basalt
II. Structure of Kilauea Volcano, Hawaii

Thesis by

Linda Rose Rowan

In Partial Fulfillment of the Requirements

for the Degree of

Doctor of Philosophy

Acknowledgements

I would like to thank my thesis advisors Tom Ahrens, Ed Stolper and Rob Clayton for their support, patience and guidance throughout my graduate career. The opportunities afforded to me in the shock wave laboratory and in the computer room were without bounds and would not have been available to me without the dedicated efforts of my advisors for which I offer my sincere gratitude. I was very fortunate to have an excellent academic advisor in George Rossman, who took time to discuss class and career options with me. Last, but not least, I would like to thank the fifth member of my defense committee, Jim Westphal for his advice and enthusiasm.

The shock wave laboratory consists of a hard working, friendly staff of capable technicians who helped make my experiments successful. My sincere thanks go to Papo Gelle, Michael Long and Alberto Devora for their help and sunny dispositions even in the face of impending experimental disaster (i.e., student panic). I also wish to thank (and apologize to) the machinists Dick Wickes, Bart Pelsue and Jose Anzueto for precisely machining many parts most of which I soon destroyed, leaving no trace of their workmanship. Also the technical drafting and advice of Bill Barber was appreciated, as was the technical guidance and spare parts given to me by Vic Nenow. The computer system of the Seismo Lab is constantly growing and changing

many students including Jon Nourse, Ken Herkenhoff, David Bell, Laurie Watson, Laszlo "The Wrecker" Keszthelyi, Hari Nair, Phil Shaller, Jack Sheng, Ariel Anbar, Jon Holt and many others.

Early morning basketball with Jim Watson, Phil Ihinger, David Pickett, Mike Wolf, Sterling Wiggins, Tom Duffy, Jim Kubicki, Dan Sykes, Gary Huss, Craig Scrivner and the rest of the guys and soccer with Sharon Kedar, Neil Humphrey, Huw, Mike W., Carey Gazis, Flavio, Richard, Matt and others was fun and also got me out of bed in the morning. Playing on the Caltech Women's Volleyball Club was a unique and fun experience and I'll never forget all the times we got lost on the way to games, all the food fights, Julie's sidewalk driving techniques etc.... Thanks for the good times and friendships, Julie, Julia, Jen, Jessica, Laurieann, T, Carey, Maureen and the rest of the team. A special thanks goes to Julie Moses and Mark Hofstadter who introduced me to a great circle of friends outside of Caltech at Westside (Sandy, Stacey, Naoto, Paul, Maida, Brandon, Anthony) and at Abbott, besides being truly great, supportive friends themselves. I also owe a special thanks to my tap-dancing, singing, boxing officemate, Sharon Kedar, who provided a great deal of support and help when the going got tough.

Of course none of this would have been possible without the love and support of my family. My parents, James and Gloria Rowan, were always very supportive and understanding throughout my long tenure as a student. I promise I'll get a real job so you can stop sending financial support and retire to some tropical paradise. To my sister, Jean and her husband John, thanks for having the kids to entertain the folks and I appreciate all your help organizing family affairs and such things. To

my sister, Kathy, thanks for the visits and birthday reminders. To my grandmother, Helen Rowan, thanks for all the fun times in Phoenix and L.A. and thanks for letting me have the big, RED truck. And finally, to my nephews, Tony and Kyle, you guys are nuts and I've enjoyed all the laughter and fun we've had.

Abstract

Linda Rose Rowan, Ph.D.

California Institute of Technology 1993

Basalts are the most ubiquitous rocks erupting at the earth's surface at the present time and they provide an important probe of the subsurface processes occurring within planetary interiors. Recent advances in both mineral physics and seismic analysis have allowed me to undertake two independent studies related to the genesis and eruption of basaltic magmas. Chapters 1 and 2 are part of an experimental study conducted in the shock wave laboratory on the equation of state of molten mid-ocean ridge basalt and the chemical interactions of the shocked liquid with its Mo container. My advisors for this project were Thomas Ahrens and Edward Stolper. Chapter 3 is a travel time tomography study of the three-dimensional structure of Kilauea Volcano, Hawaii in collaboration with Robert Clayton. Chapter 3 is currently in press in the Journal of Geophysical Research.

The EOS of molten MORB to 20 GPa was accomplished using the innovative silicate liquid shock wave measurement technique on the 40 mm propellant gun developed by *Rigden* [1986] and *Miller* [1990]. This technique has been used to determine the EOS for four synthetic melts and this thesis applies the technique to a natural

melt, a MORB dredged from the Juan de Fuca ridge. The resulting EOS indicates that the MORB liquid is very compressible and therefore has a low bulk modulus of 11.7 GPa. These results are consistent with low pressure static compression experiments on similar basalts, but are not consistent with the results of ultrasonic interferometry. The compressible nature of the MORB liquid is related to its composition and this may be expressed best by comparing the MORB Hugoniot to the Hugoniot determined for $An_{36}Di_{64}$ and komatiite. The MORB and $An_{36}Di_{64}$ Hugoniots show significant increase in density at low pressure followed by a stiffening at high pressures where the liquid Hugoniot approaches its respective dense oxide high pressure composition. This may be related to gradual coordination changes from four-fold to six-fold for the Si^{+4} and Al^{+3} which are essentially complete at the high pressure where the curve stiffens. The MORB is much more compressible than the komatiite and overtakes the komatiite in density at a low pressure of 2.5 GPa. This is a compositional effect caused by the enrichment of the MORB in Al_2O_3 and SiO_2 and depletion in MgO compared to komatiite. The compressible nature of the MORB allows it to become denser than the surrounding mantle near the base of the low velocity zone and therefore it is unlikely that MORB can be derived from very deep in the earth's upper mantle.

For most shock wave experiments, the sample is not recovered and nothing can be determined about its structure or composition due to the passage of the shock wave. In a few of my EOS experiments on molten MORB, however, the shocked sample was recovered and could be studied in detail. Observations of impact-induced interactions between the silicate liquid and its Mo container provide insight into

planetary impact and differentiation processes involving metal-silicate partitioning. The shocked liquids showed extreme reduction and with increasing pressure the FeO content of the initial melt was reduced to almost nothing by reaction with the Mo. These reactions produced metallic particles enriched in Mo, Fe and Si. These particles show a similar texture as those found at impact sites on the earth and moon and provide clues to the impact origin of metallic particles.

A travel time tomography study of local P wave data from Kilauea Volcano, Hawaii, was undertaken to determine the lateral heterogeneities produced by its intricate magmatic and tectonic environment. The technique proved to be a powerful probe of the volcano's intrusive plumbing because the presence of a dense seismic array and many local earthquakes allowed for excellent coverage of complex subsurface features. Analysis and interpretation of the tomographic images leads to the following inferrred model. The main shallow magma reservoir is delineated by a slow anomaly centered 2 km southeast of Halemaumau caldera. There is a distinct high velocity region centered northwest of the summit from 0 to 2 km depth that may represent a dense wall and/or cap of intrusive rock that acts as a barrier or containment structure for the northern part of the reservoir. We suggest that the shallow reservoir is a narrow, compartmentalized region of sills and dikes because of the closely spaced high and low velocity anomalies near the summit. The rift zones of Kilauea are imaged as major, high velocity entities, widening to the south with depth until 6 km. These fast anomalies may be related to the sheeted dike complexes along the rifts. On a finer scale, magma pockets centered at 0–2 km depth have been inferred beneath Makaopuhi, Mauna Ulu and Puu Oo, along the east rift zone. The

Hilina and Kaoiki fault zones, are imaged as slow features at shallow depths (< 6 km), related to their tensional structures that produce the open fractures and cracks in the basaltic edifice. The Koae fault system is imaged as a slightly fast shallow structure (< 6 km) possibly related to intrusive diking from the adjacent rift zones. Continued inversions with the immense amount of seismic data collected for Hawaiian events will allow the detailed development of a three-dimensional velocity model for Kilauea. Such a model will be extremely useful to seismologists and petrologists alike for understanding the tectonic growth and magmatic evolution of this dynamic shield volcano.

Table of Contents

List of Tables

List of Figures

Chapter 1

EOS of Basaltic Liquids

We have determined the equation of state of a mid-ocean ridge basalt liquid and found it to be a very compressible melt. The extrapolated bulk sound speed, 2.10 km/s and slope of the $U_s - U_p$ relation, s=1.68, along with the calculated initial denisty of this liquid at 1400^oC, give a very low isentropic bulk modulus of 11.7 GPa and a K' of 5.7. The compressible nature of this liquid may be attributed to its composition which is enriched in SiO_2 and Al_2O_3 and relatively poor in alkaline earths. At low pressures, the Si^{+4} and Al^{+3} may undergo coordination changes from four-fold to six-fold in a gradual but significant amount. At high pressures (~ 20 GPa) these changes are probably complete as noted by a stiffening of the Hugoniot curve and the convergence of the liquid density to that of its dense oxide equivalent. The alkaline earths, CaO and MgO, are compactly bounded structures that do not undergo any significant coordination changes and therefore any increase in these oxides in the liquid should decrease the compressibility of the melt. This is why the mafic, MgO-poor basalt is more compressible than the ultramafic, MgO-rich

komatiite as a function of increasing pressure. The MORB Hugoniot shows a density crossover at ∼2.5 GPa with the komatiite Hugoniot and the MORB is denser than the komatiite throughout the rest of the mantle. This has important implications for magma genesis. Comparing the MORB Hugoniot to PREM indicates that the liquid becomes denser than the average solid mantle near the base of the low velocity zone and it may be possible to concentrate magma in this zone. Furthermore, any basaltic magma that is brought down below the LVZ will stagnate at some level and re-equilibrate with the mantle, thereby providing a mode for enriching the mantle. For the shallow genesis of MORB, the equilibrium crystal phases, olivine, clinopyroxene, orthopyroxene and garnet, in the melt are all denser than the liquid while plagioclase is always lighter. The olivine crossover for the MORB occurs at ∼7 GPa near the base of the LVZ, while the pyroxenes have a crossover near 5 GPa. These density contrasts are consistent with the origin of MORB magmas at shallow levels (0.5 - 2.0 GPa) because a large density contrast between the melt and solid residue allows for efficient segregation and rapid buoyant ascent of the magma within the solid mantle. If basalts are derived from deeper levels (> 3 GPa), then larger percentages of partial melts are required because the density contrast rapidly decreases due to the compressible nature of the MORB and thus segregation and buoyant escape are hindered for small melt fractions.

1.1   Introduction

The determination of the equation of state (EOS) of the earth's most common magmatic composition, molten basalt, was undertaken because the density of silicate

liquids as a function of pressure, temperature and composition is a crucial parameter needed to model the evolution of planetary interiors and the dynamics of magmatic systems. The EOS can be used to derive other important physicochemical parameters of the liquid including its bulk sound speed, isentropic bulk modulus and its derivatives and the Grüneisen parameter. This work is a continuation of the silicate liquid shock wave techniques developed by *Rigden* [1986] and advanced by *Miller* [1990]. To date, a limited number of compositions have been examined at relatively high pressures (< 40 GPa) using shock wave techniques and these equations of state provide a compositional database from which to compare the effects of different oxide components on the liquid's compressibility at high pressures. Furthermore it is useful to compare the EOS and its extrapolation to zero pressure properties with measurements made at low (≤6 GPa) to ambient pressures using other techniques, such as sink/float density measurements and sound speed measurements using ultrasonics.

1.2 Experimental Technique

1.2.1 Materials and Synthesis

The starting material was a mid-ocean ridge basalt (MORB) from the Juan de Fuca Ridge located in the northeastern Pacific Ocean off the coasts of Washington and Oregon. The dredging was done by the University of Washington, R/V T. G. Thompson (TT152), in 1980 [*Delaney et al.*, 1981]. The starting sample (dredge # 75-2) was recovered from a depth of 2260 m along segment 3 (S3); the distal edge of the south rift zone of Axial Seamount. Axial Seamount is considered to be the current expression of the Cobb Hotspot, although there is limited evidence of an enriched

mantle plume source in the erupted lava, the composition of the basalt is slightly different from the average Juan de Fuca basalt (Table 1.1). Dredge #75 is further distinguished from a typical Juan de Fuca basalt and the generally homogeneous basalts erupted at the summit of Axial Seamount by its relatively primitive (high Mg#, low SiO_2 and low TiO_2) composition and unusually porphyritic texture [*Delaney et al.*, 1981]. It has been suggested that this basalt was derived from a greater depth of the melting column beneath Axial Seamount and that it by-passed the main Axial Seamount magma chamber and erupted along it's south rift zone instead [*Rhodes et al.*, 1990].

Our sample consists of approximately 15 – 20% plagioclase phenocrysts (ranging in size from 1 – 5 mm) and minor amounts of smaller (<3 mm) olivine crystals. The starting glass disks were synthesized from the bulk rock sample by melting the basalt powder in a molybdenum crucible in a gas mixing furnace at 1280 ± 5°C, in a reducing atmosphere held at approximately the iron-wustite (IW) buffer for a minimum of 12 hours.

A core (diameter~10 mm) of basaltic glass was drilled from the Mo crucible and sliced to the appropriate thickness (~3.3 mm) for the experiment. The major element chemistry of some of the extra slices from these cores were measured on the Caltech JXA superprobe electron microprobe. The typical probe conditions were an operating voltage of 15 KeV with a beam current of 20 nA, a collection interval of <60 s per oxide and a relatively defocussed beam diameter of 20 μm to avoid significant alkali loss during analysis. Mineral standards were used for the major oxides and Mo metal for MoO_3 . The analyses presented in Table 1.2 indicate that the glass

Oxide	XRF		Electron
Wt %	2a	2b	Microprobe
SiO_2	48.57	48.15	49.24
TiO_2	1.07	1.05	1.25
Al_2O_3	17.63	17.80	15.27
FeO	0.00	0.00	8.72
Fe_2O_3	10.32	10.07	1.94
MgO	7.29	7.29	7.73
CaO	12.99	12.80	12.73
K_2O	0.10	0.12	0.09
Na_2O	2.32	2.55	2.69
MnO	0.16	0.16	0.19
NiO	N.A.	N.A.	N.A.
P_2O_5	0.10	0.12	0.10
S	N.A.	N.A.	0.13
TOTAL	100.55	100.09	99.92

Table 1.1: Chemical analysis of Juan de Fuca Ridge dredge sample TT152-75-2. The first two columns are X-ray fluorescence analyses by *Rhodes et al.* [1990] and the third column is unpublished electron microprobe analysis by Delaney and others.

samples were homogeneous, with minor contamination from the Mo crucible, and no significant chemical variation between the cores.

The average composition of the MORB derived from these analyses (Table 1.2) was used to determine the initial density of the liquid using the partial molar volumes and their temperature derivatives from *Lange and Carmichael* [1987] and *Kress and Carmichael* [1991]. At the initial temperature of the experiments, 1400°C, the calculated initial density of the MORB liquid is 2.66 ± 0.01 gm/cc.

The MORB disks were encapsulated in Mo containers (Figure 1.1) by electron beam welding, under vacuum. The thickness of the glass disk (3.2 – 3.45 mm) used for each container was based on the available volume in the Mo container and the volume of the MORB liquid at 1400°C. The coefficient of thermal expansion, α, for Mo metal is $2.373 \pm 0.1 \times 10^{-5} K^{-1}$ [*Touloukian et al.,* 1970]. For the MORB liquid, $\alpha = 6.34 \pm 1.3 \times 10^{-5} K^{-1}$, was calculated from the predictive models of *Lange and Carmichael* [1987] and *Kress and Carmichael* [1991]. On average, the cold Mo containers were filled to about 85% of their initial volume and since the MORB liquid will expand $\sim 6\%$ more than the hot Mo metal, about 91% of the volume of the container was filled at 1400°C. The excess free volume should keep the Mo container from deforming at high temperature due to overfilling. Bowing of the Mo container (particularly the Mo cap) due to sample expansion and the strength of the weld were checked by placing the sealed container in a Deltech furnace at 1350°C in the presence of a nitrogen gas flow. Containers that showed no distension or leakage of basalt along the weld were polished to an approximately flat, reflective surface on the Mo driver upper surface and the Mo cap (side mirrors and center

Table 1.2: Electron Microprobe analysis of homogenized MORB glass disks used for shock wave experiments. The reported values are the mean and standard deviation of the mean for a series of points along transects in each disk. The number at the top of each column is the core # and the letter indicates the position of the disk in the core, top (t), middle (m) or bottom (b). Also listed at the bottom is the shot number for disks cut from a given core.

	MORB Glass					
Oxide Wt %	7b	11t	11b	12t	16m	17m
SiO_2	48.50 ± 0.06	48.37 ± 0.16	47.44 ± 0.06	48.13 ± 0.09	48.12 ± 0.07	48.51 ± 0.16
TiO_2	1.035 ± 0.002	1.05 ± 0.01	1.059 ± 0.004	1.05 ± 0.007	1.062 ± 0.009	1.064 ± 0.005
Al_2O_3	17.71 ± 0.02	17.94 ± 0.07	17.79 ± 0.02	17.88 ± 0.05	18.03 ± 0.07	17.81 ± 0.06
FeO	8.96 ± 0.01	8.95 ± 0.03	9.07 ± 0.03	8.96 ± 0.02	8.94 ± 0.03	9.06 ± 0.03
MgO	7.24 ± 0.01	7.42 ± 0.05	7.30 ± 0.04	7.39 ± 0.01	7.38 ± 0.02	7.41 ± 0.04
CaO	12.52 ± 0.02	12.54 ± 0.04	12.59 ± 0.03	12.54 ± 0.02	12.46 ± 0.03	12.74 ± 0.01
K_2O	0.100 ± 0.001	0.058 ± 0.004	0.065 ± 0.005	0.056 ± 0.004	0.058 ± 0.004	0.069 ± 0.003
Na_2O	2.566 ± 0.004	2.51 ± 0.02	2.43 ± 0.01	2.55 ± 0.01	2.46 ± 0.01	2.47 ± 0.02
MnO	0.157 ± 0.002	0.159 ± 0.007	0.16 ± 0.01	0.163 ± 0.008	0.163 ± 0.004	0.165 ± 0.005
NiO	N.A.	0.004 ± 0.002	0.007 ± 0.005	0.005 ± 0.003	0.009 ± 0.004	0.009 ± 0.004
MoO_3	0.080 ± 0.003	0.07 ± 0.02	0.13 ± 0.01	0.06 ± 0.01	0.21 ± 0.02	0.19 ± 0.01
TOTAL	98.96 ± 0.09	99.06 ± 0.31	98.05 ± 0.10	98.79 ± 0.19	98.88 ± 0.08	99.50 ± 0.26
Points	28	9	9	7	10	10
Shot	739	823, 833	833, 834	None	825	826

mirror respectively in Figure 1.1a).

1.2.2 Shock Wave Experiment

The shock wave experiments were conducted using the 40 mm bore propellant gun at Caltech. The general characteristics of this gun have been described previously by *Ahrens et al.* [1971]. The gun has a range of projectile velocities from 0.3 – 2.5 km/s which along with a range of flyer plate materials, allows the sample to be compressed to upper mantle pressures (1 – 25 GPa). The shock wave technique for measuring the EOS of molten silicates was developed by *Rigden et al.* [1988], who determined the compressibility of liquids in the anorthite – diopside compositional regime. The technique has been further advanced and described by *Miller et al.* [1991a], who measured the EOS of komatiitic liquid.

Briefly, a Pt–90%Pt10%Rh thermocouple is press fit into a pin size hole next to the sample Mo shoulder wall (Figure 1.1a) and the Mo target is fitted into a Zircar alumina (90-85% Al_2O_3, 10-15% SiO_2) ceramic holder. The fibrous alumina is used because it is machinable, resists cracking and shrinking to about 1650^oC and has a high melting point ($T_m \sim 1900^oC$). The target assembly is vertically hung in the gun tank and aligned with the gun barrel, the water-cooled copper induction coil and the optical equipment (Figure 1.2). After alignment, the gun tank is closed and evacuated to less than 100 μm Hg ($\sim$0.1 torr). A relatively low vacuum is necessary for most shock wave experiments to maintain a clean path for the projectile and optical equipment. For the EOS of silicate liquids, a low vacuum is also essential during the heating phase of the experiment to prevent oxidation of the polished Mo metal or arcing of the Cu coil. The sample is heated by induction to 1400^oC using

Figure 1.1: *a.* Plan view of molybdenum sample container *b.* Cross section of container that shows the MORB liquid with a miniscus at the top and some bubbles within the sample. Both features are only schematic. The horizontal line represents the position on container where the shock transit time through the sample and cap are measured from the streak record. *c.* Cross section of container showing the possible wave interactions between the shock wave and the release waves from the outer edges of the liquid. α indicates the angle over which the release waves interfere with the shock wave in the liquid and it is determined from Eqn. 1.9 (see section 1.3.2 for a complete discussion).
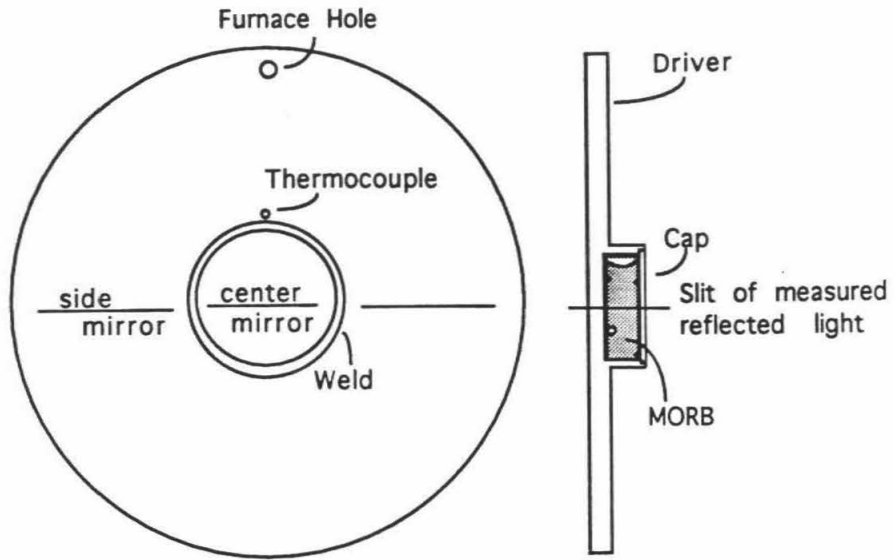
a. Plan View of Sample Container   b. Cross Section
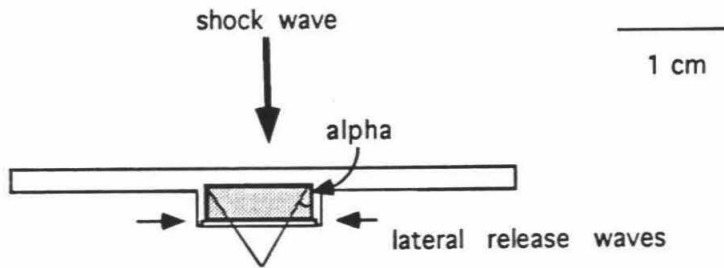
c. Wave interactions in sample along slit

a 10 kW Lepel radio frequency generator. It takes approximately 10 minutes for the target to reach 1400^oC, as measured by the thermocouple. The sample and Mo container are held at 1400 ± 5^oC for $\sim 2 - 5$ minutes while final preparations are made to fire.

Two parameters are measured during the experiment, the projectile velocity (V_{imp}) and the shock transit time (tt) through the liquid sample plus Mo cap. The projectile velocity is measured by a double exposure x-ray shadowgraph. The projectile velocity is calculated from:

$$V_{imp} = \frac{l + \delta}{M(\triangle t)} \tag{1.1}$$

where l is the distance between the metal flyer images on the shadowgraph, δ is the parallax, M is the film magnification and $\triangle t$ is the pre-set time delay between x-rays. Using this method the projectile velocity is accurate to $\pm 2\%$ [*Rigden et al.,* 1988].

The shock transit time, tt, is determined from the streak record which records the change in reflectance on the Mo driver (side mirrors) and the Mo cap (center mirror) due to the arrival of the shock wave at the free surface. Just before impact, a xenon flash lamp light source illuminates the polished Mo surface. This light is reflected and focussed through a horizontal slit (Figure 1.1a,b) into a continuous writing streak camera. A typical streak record is shown in Figure 1.3. By measuring the distance between the cut-off on the side mirrors and the cut-off on the cap mirror, the tt is obtained from:

$$tt = \frac{\text{print distance}}{\text{writing rate}} = \frac{d/M}{4\pi RCr} \tag{1.2}$$

Figure 1.2: Cross sectional view of experimental set-up in 40 mm bore gun tank. For our experiments the flyer plate material was either 2024 Al or Cu in a lexan projectile. The Cu induction coils were used to heat the sample to $1400^{\circ}C$ and a Pt–90%Pt10%Rh thermocouple measured the temperature prior to impact.

Projectile

Al Flyer

Al Ceramic Holder

Thermocouple

Mo container

Cu Induction Coils

1 cm
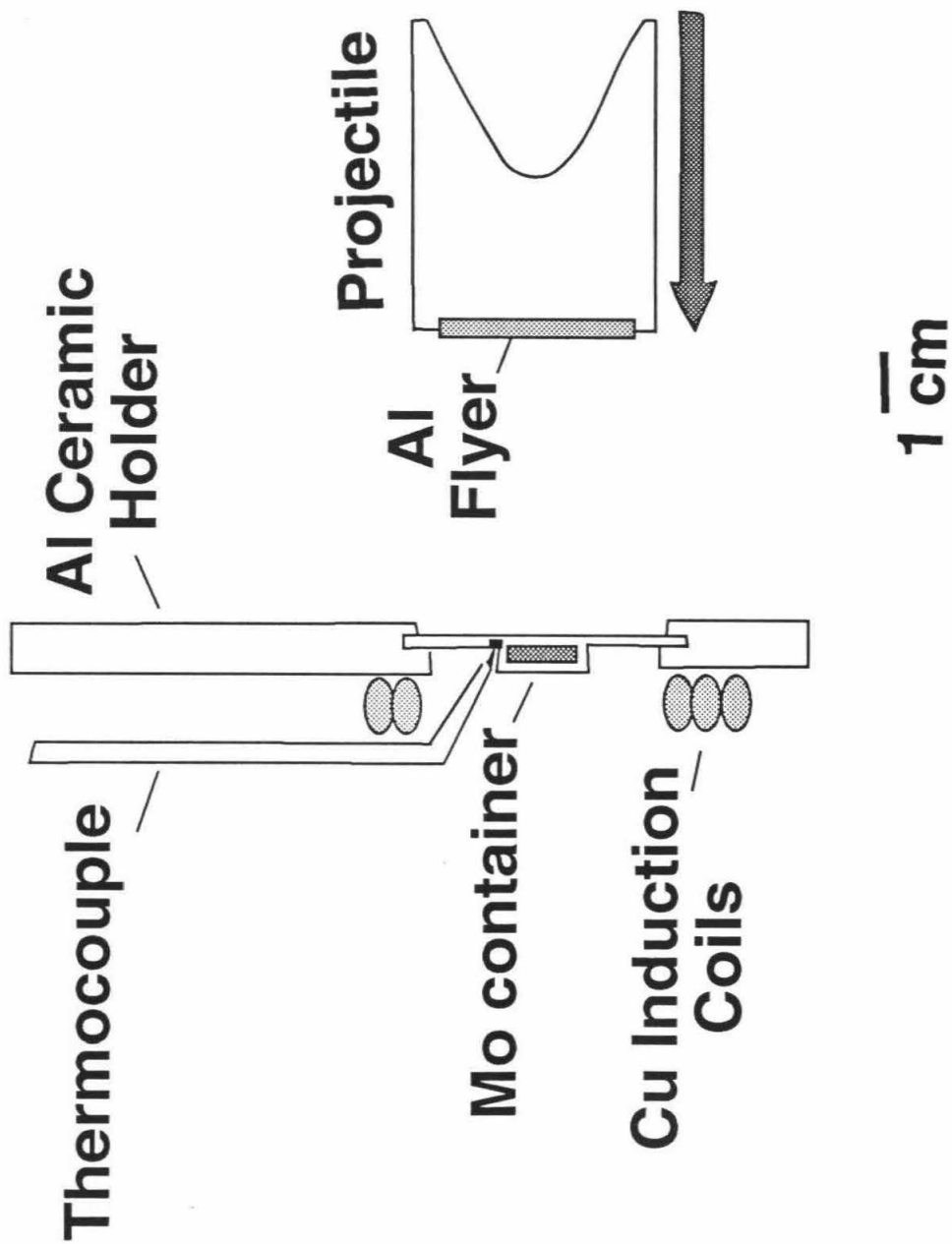
where d is the distance measured on the streak record between the driver and cap cut-off, M is the print magnification, Cr is the the circumference of the camera film track ($\sim$27.94 cm) and R is the rate at which the prism is revolving, typically 2000 rev/s. The writing rate is $\sim$7mm/μs. The measured tt represents the time for the shock wave to travel through the sample and Mo cap, with a correction added for the thickness of the driver beneath the sample. This correction is necessary because the inner well of the driver (upon which the sample is placed) is polished separately to a slightly different thickness than the outer diameter of the driver, the polished side mirrors. The difference in driver thickness (δx_d) is small, typically $\sim \pm 0.02$ mm and this small correction to the tt is made in the impedance match calculations.

1.2.3   Impedance Match Method

Given the initial temperature, the projectile velocity and the shock transit time, the EOS of the basaltic liquid can be determined using the impedance match method. In this method, a material with known Hugoniot EOS parameters, C_o and s, is interfaced with a material whose EOS parameters we are trying to determine. If the development of the shock front (rise time) is time-independent and therefore represents a sharp discontinuity in density between the shocked and unshocked material then the Rankine-Hugoniot conservation equations [*Duvall and Fowles,* 1963] may be used to determine the EOS. The three equations for mass, momentum and energy conservation, respectively, are

$$\rho_o U_s = \rho(U_s - U_p) \tag{1.3}$$

$$P - P_o = \rho_o U_s U_p \tag{1.4}$$
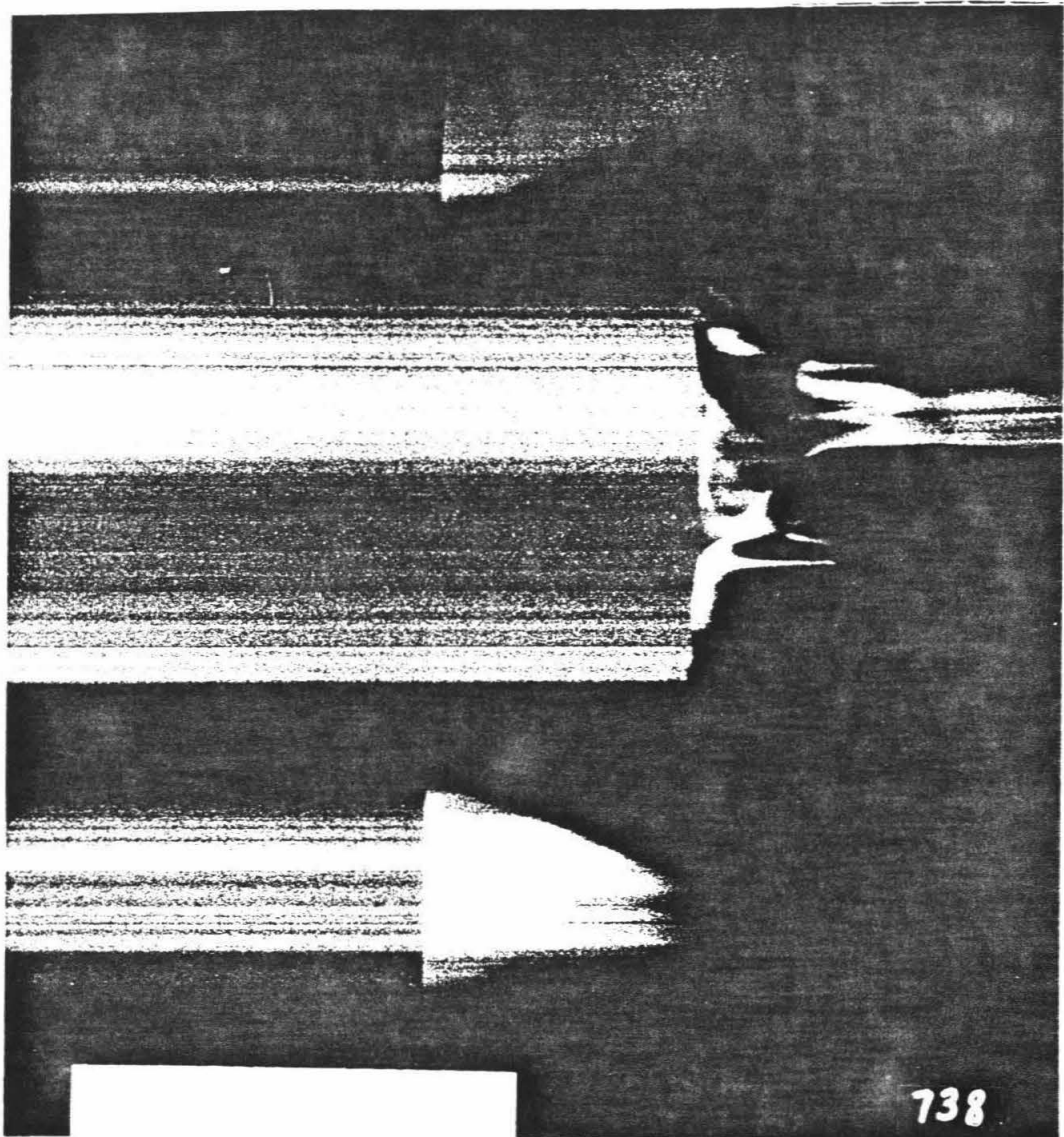
Figure 1.3: Typical streak record for molten MORB shock wave experiments. This record is from shot# 738. The center mirror cut-off (cap) shows a slight convex curvature, which is discussed in section 1.3.2.

$$E - E_o = 1/2(P + P_o)(V_o - V) \tag{1.5}$$

where U_s is the shock velocity, U_p is the particle velocity, P is the pressure, ρ is the density, E is the internal energy and V is the specific volume (i.e., $V = 1/\rho$). The subscript ^{o} refers to the values at the initial, unshocked state.

The impedance match method is applied three times (flyer-driver, driver-sample and sample-cap interfaces) for liquid silicate EOS experiments, following the technique of [*Miller et al.*, 1991a]. Two different materials were used for the flyers in these experiments (Cu or 2024 Al) and their EOS parameters, along with the EOS parameters for hot (1400^oC) Mo metal, are given in Table 1.3.

Once the high pressure properties of the liquid for each shot have been determined, the zero pressure bulk sound speed, C_o and s, can be determined by fitting the $U_s - U_p$ data. The majority of shock wave data, for materials with negligible strength and no phase transitions, can be described by the first order linear relation [e.g., *Ruoff*, 1967]

$$U_s = C_o + sU_p. \tag{1.6}$$

The $U_s - U_p$ relation is fitted using a weighted least squares approach and the intercept, C_o, and slope, s, of this line along with ρ_o, provide a complete description of the EOS of the liquid.

1.3 Results

1.3.1 Linear $U_s - U_p$ fit and Hugoniot curve

Twelve shots were used to determine the EOS of molten basalt. The first two shots (# 677 and 678) were conducted by P. Ihinger. The experimentally measured pa-

	Copper[a]	Aluminum[a]	Molybdenum[b]
T ^{o}**C**	25	25	1400
$\rho_{o\mathbf{T}}$ **[gm/cc]**	8.93 ± 0.0	2.78 ± 0.0	9.961 ± 0.02
Co [km/s]	3.94 ± 0.0	5.33 ± 0.0	4.77 ± 0.06
s []	1.49 ± 0.0	1.34 ± 0.0	1.43 ± 0.05
Kos [GPa]	22.5 ± 0.8	27.0 ± 0.6	232 ± 6
K′ []	4.16 ± 0.24	4.9 ± 0.1	4.7 ± 0.2
$\alpha \times 10^{-5}$ **[K^{-1}]**	—	—	2.373 ± 0.1[c]
Cp [J/gmK]	—	—	0.345 ± 0.02[c]
$\gamma_{\mathbf{o}}$ **[]**	—	—	1.56 ± 0.7

[a] Hugoniot EOS: *Marsh*, 1980

[b] Hugoniot EOS: *Miller*, 1990

[c] Calculated from *Touloukian et al.*, 1970

Table 1.3: EOS parameters for flyer and driver materials

rameters, V_{imp} and tt, along with the important dimensions of each target are given in Table 1.4. For the two shots conducted by Ihinger, V_{imp} and tt were recalculated from the x-ray shadowgraphs and streak records to assure consistency. Given this data set and the Mo and flyer EOS parameters (Table 1.3) the shots were fit using the empirical $U_s - U_p$ fit and impedance match as described in section 1.2.3. The shocked, high pressure properties of the molten MORB for each shot are given in Table 1.5.

The twelve shots fit the linear $U_s - U_p$ relation with a χ^2 of 7.2. Figure 1.4 shows the best fit line along with the individual experiments. The intercept, C_o, is 2.10 ± 0.15 km/s and the slope, s, is 1.68 ± 0.19. These values along with the initial, pre-heat density of 2.66 ± 0.01 gm/cm^3 can be used to solve for the zero pressure isentropic bulk modulus, K_{os}, and its first pressure derivative, K'_s, from

$$K_{os} = C_o^2 \rho_o \tag{1.7}$$

$$Ks' = 4s - 1 \tag{1.8}$$

to give $K_{os} = 11.7 \pm 1.7$ GPa and $K'_s = 5.7 \pm 0.7$ for the MORB liquid. The Hugoniot curve determined from the Rankine-Hugoniot relations using the C_o and s from the linear $U_s - U_p$ fit is shown in Figure 1.5 along with the individual shots.

1.3.2 Complications of Liquid Silicate Shock Wave Measurements

Shock wave experiments on silicate liquids are more complicated than shock wave techniques used to determine the EOS of solids because of the need to heat the sample to high temperatures prior to impact and the need of a suitable container to

Shot	flyer*	V_{imp} [km/s]	tt [μ s]	x_s [mm]	x_c [mm]	x_d [mm]
760	Al	0.83 ± 0.01	1.29 ± 0.08	3.32 ± 0.03	0.71 ± 0.01	0.0058 ± 0.0069
740	Cu	1.00 ± 0.01	1.16 ± 0.07	3.37 ± 0.04	0.77 ± 0.01	0.0653 ± 0.0151
761	Al	1.03 ± 0.02	1.34 ± 0.09	3.34 ± 0.03	0.72 ± 0.01	0.0205 ± 0.0064
823	Al	1.21 ± 0.02	1.33 ± 0.07	3.33 ± 0.03	0.79 ± 0.01	-0.0106 ± 0.0026
763	Al	1.25 ± 0.02	1.36 ± 0.09	3.36 ± 0.03	0.73 ± 0.01	-0.0211 ± 0.0120
833	Al	1.33 ± 0.02	1.21 ± 0.07	3.45 ± 0.03	0.74 ± 0.01	-0.1238 ± 0.0056
739	Cu	1.41 ± 0.03	1.02 ± 0.06	3.34 ± 0.03	0.68 ± 0.01	0.0224 ± 0.0088
824	Al	1.49 ± 0.03	1.14 ± 0.06	3.38 ± 0.03	0.77 ± 0.01	-0.0451 ± 0.0116
737	Cu	1.76 ± 0.05	0.91 ± 0.05	3.38 ± 0.03	0.85 ± 0.01	0.0038 ± 0.0094
678*	Cu	1.94 ± 0.04	0.90 ± 0.05	3.34 ± 0.03	0.82 ± 0.01	0.0083 ± 0.0035
677*	Cu	1.99 ± 0.03	0.88 ± 0.05	3.34 ± 0.03	0.85 ± 0.01	0.0231 ± 0.0033
738	Cu	2.15 ± 0.05	0.85 ± 0.05	3.36 ± 0.03	0.86 ± 0.01	-0.0352 ± 0.0106

* For Al flyers, 2024 Al was used

* Experiments done by P. Ihinger

Table 1.4: Parameters measured for each shock wave experiment.

P [GPa]	Density [gm/cc]	Us [km/s]	Up [km/s]	Shot
2.77 ± 0.17	3.04 ± 0.04	2.88 ± 0.19	0.36 ± 0.01	760
3.38 ± 0.24	3.19 ± 0.06	2.78 ± 0.21	0.46 ± 0.01	761
4.10 ± 0.23	3.29 ± 0.06	2.85 ± 0.18	0.54 ± 0.01	823
4.16 ± 0.28	3.35 ± 0.07	2.76 ± 0.21	0.57 ± 0.01	763
5.16 ± 0.29	3.23 ± 0.05	3.31 ± 0.21	0.59 ± 0.01	833
6.08 ± 0.34	3.29 ± 0.06	3.46 ± 0.21	0.66 ± 0.02	824
6.59 ± 0.42	3.44 ± 0.09	3.31 ± 0.24	0.75 ± 0.01	740
10.43 ± 0.68	3.70 ± 0.13	3.73 ± 0.27	1.05 ± 0.03	739
15.29 ± 0.97	3.74 ± 0.13	4.46 ± 0.31	1.29 ± 0.04	737
16.76 ± 1.02	3.94 ± 0.16	4.40 ± 0.30	1.43 ± 0.04	678*
17.55 ± 1.06	3.93 ± 0.16	4.52 ± 0.32	1.46 ± 0.03	677*
20.14 ± 1.38	3.94 ± 0.18	4.83 ± 0.37	1.57 ± 0.05	738

* Experiments done by P. Ihinger

Table 1.5: Results for twelve shots on molten MORB.

Figure 1.4: Empirical fit of shock wave data to $U_s - U_p$ for MORB liquid at 1400°C and $\rho_o = 2.66$ gm/cm^3. The solid line indicates the linear fit, $U_s = 2.10 + 1.08 U_p$ and the dashed curve indicates the quadratic fit, $U_s = 2.65 + 0.29 U_p + 0.72 U_p{}^2$, forced to intersect the calculated bulk sound speed (open diamond) from the data of *Kress and Carmichael* [1991]. Open circles denote shots done by Phil Ihinger.
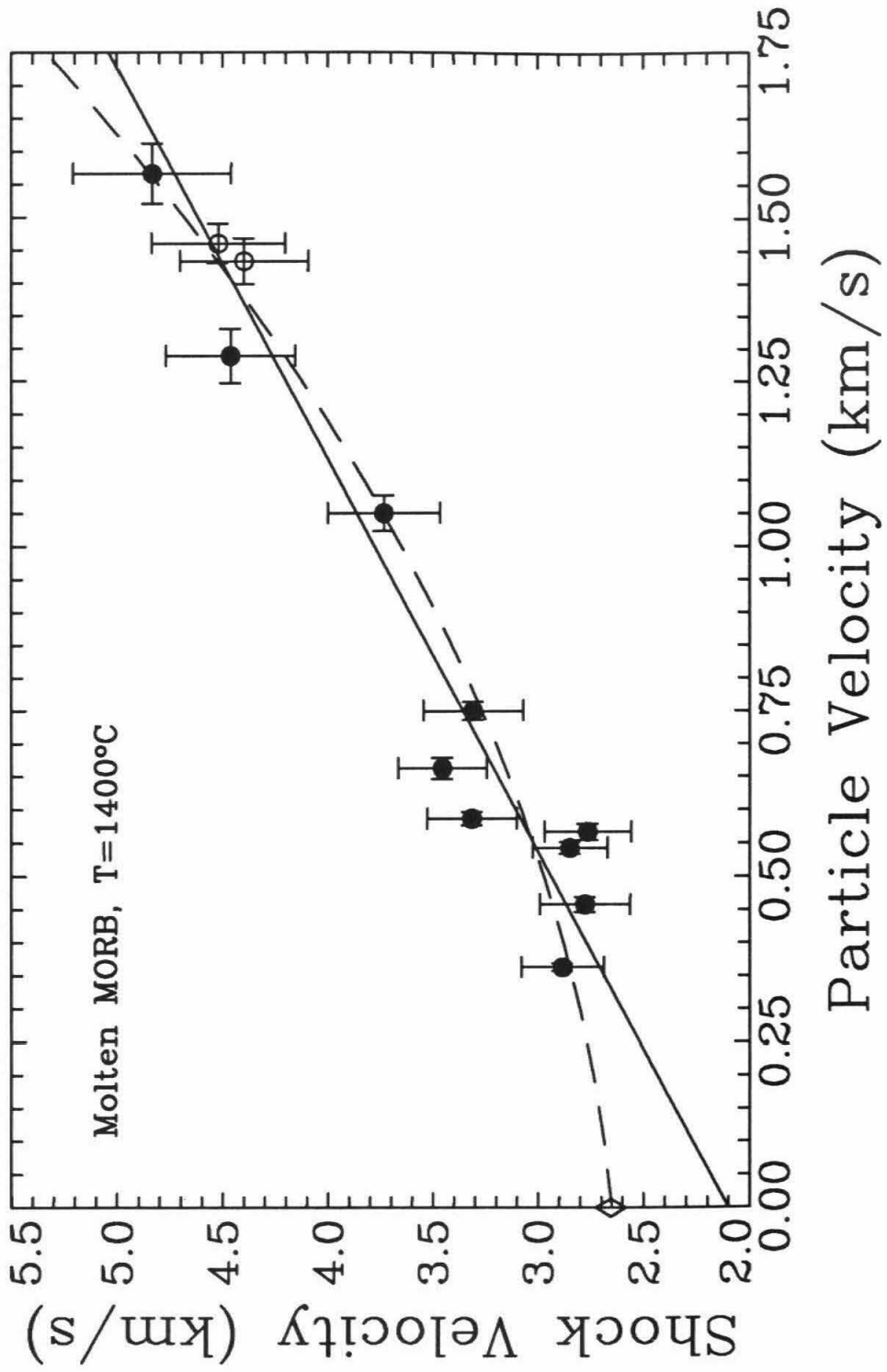
Figure 1.5: Hugoniot curves and experimental datapoints for each shot for MORB liquid at 1400°C and $\rho_o = 2.66$ gm/cm^3. Solid curve was determined using the linear $U_s - U_p$ fit ($C_o = 2.1$ and s=1.68) and the dashed curve was determined using the quadratic $U_s - U_p$ fit forced to have an intercept at the calculated bulk sound speed, $C_o = 2.65$, from *Kress and Carmichael* [1991] with a slope, s=0.29 and s'=0.72. Open circles indicate shots done by Phil Ihinger. The dotted curve is the high pressure dense oxide Hugoniot for the MORB composition determined by volume additivity.
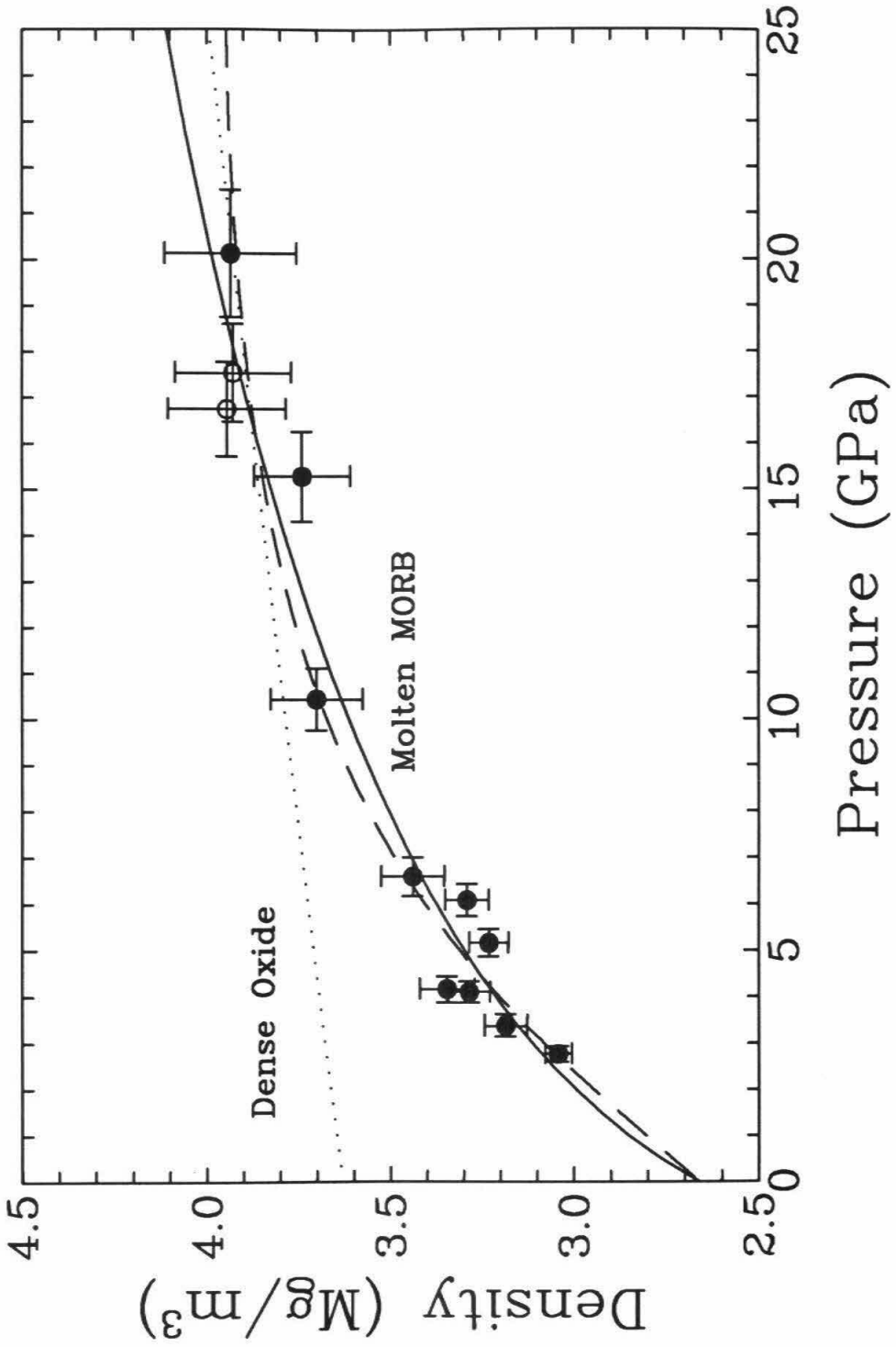
hold the liquid. It is important to estimate how the shock wave is effected by the geometry of the container and the higher temperatures.

Elastic precursor

The Hugoniot elastic limit (σ^{HEL}) is defined as the maximum stress that a solid can maintain in a planar shock compression without irreversible deformation occurring at the shock front. For the silicate liquid shock wave experiments, the stress must be greater than the Hugoniot elastic limit (yield strength) in the container material (Mo) in order to assure that the shock wave velocity is being measured, rather than an elastic precursor. For Mo, the elastic precursor for a 3 mm thick sample is $\sigma_{HEL} \sim 1.6 \pm 0.2$ GPa at room temperature [*McQueen et al.,* 1970]. *Duffy* [1992] measured the Mo elastic precursor for a 5 mm thick sample, at 1400°C, and found $\sigma_{HEL} \sim 1.64$ GPa. Thus temperature and small changes in the sample thickness do not seem to have a significant effect on the amplitude of the stress (σ_{HEL}). Given the limited data available and the difficulties of measuring the elastic precursor, we have assumed that the Mo driver (~ 2 mm thick) and Mo cap (~ 0.8 mm thick) have a $\sigma_{HEL} \sim 1.6 \pm 0.4$ GPa at 1400°C. For our experiments, only the lowest pressure shot (# 826, P$\sim$0.8 GPa, $V_{imp} = 1.02$ km/s with a lexan flyer) had a low enough pressure (Mo cap shock pressure of ~ 1.7 GPa) to suggest possible complications from the elastic precursor. This shot also had a very ambiguous streak record (i.e., the cut-off is poorly defined on the cap) and it has been excluded from the Hugoniot fit for these reasons. The other shots were done at higher pressures with metal flyers that preclude any significant effects from the elastic precursor and none of the streak records showed as poor a cut-off as shot # 826.

Lateral wave effects

If the shock wave is planar when it intersects the reflected light free surface measured by the streak camera, then the cut-off on the streak record should be flat. This is true for the side mirror cut-offs in all the experiments, but is not true for the cap cut-offs. In most cases, the very edges of the cap cut-off were sharply curved outward (i.e., concave curvature), due to complications from the outer radius of the cap.

The sharp concave curvature along the cap edges on the streak records may be due to release waves propagating inwards, from the outer diameter of the liquid sample space, that interfere with the shock front. The amount of interference may be estimated using the method of *Al'tshuler* [1965] to define the angle of the encroaching rarefaction waves within the liquid. If the angle is large ($\sim 60^o$, for a sample thickness of $\sim$3.4 mm and diameter of 10.8 mm) then the release waves from the outer edge will converge within the liquid and the shock wave transit time is not being measured on the streak records. If the angle is smaller, then the shock wave should be the first arriving wave on the base of the central part of the cap. It is assumed that this wave will propagate through the cap without much further interference, because the cap is thin, so that the first arrival on the center of the cap free surface is the shock front through the sample plus cap. The angle, α, can be estimated from

$$tan^2\alpha = \frac{C^2}{U_s^2} - \left(\frac{U_s - U_p}{U_s}\right)^2 \tag{1.9}$$

where C is the high pressure bulk sound speed in the liquid. The angle, α, will increase with increasing shock pressure because the sound speed increases more than the shock velocity as a function of increasing pressure. For the highest pressure shot (# 738), using $C = 5.8$ km/s, we get $\alpha = 45^o$ and the rarefaction waves will

not converge within the MORB liquid. Therefore the center of the cut-off on the cap for all the shots are not effected by the lateral release waves from within the liquid. However, the actual wave interactions are much more complicated than this simple calculation suggests because the propagation of the elastic release wave, the interaction of the shock wave in the liquid with the shock and/or release wave from the Mo sidewalls and the effect of the cap are ignored.

On six of the streak records (shots # 677, 678, 738, 739, 761, 824), the cap shows a broad convex curvature across the entire cut-off. The curvature on the streak record for shot # 738 (Figure 1.3), is representative of the other streak records except for shot # 824 which showed a more pronounced curvature that became very flat near the center of the cap and also showed significant concave curvature along both edges. One possible explanation for the slight convexity on the streak record is that the cap was slightly bowed due to expansion of the liquid during the pre-heating stage of the experiment. This possibility suggests limited effects from lateral release waves because it requires the shock front impinging upon the cap to be planar or have less convex curvature than the distended cap. If this were the case, then the calculated sample thickness would be underestimating the actual sample thickness by an amount proportional to the curvature on the streak record. The effect of possible bowing of the cap can be tested by comparing the distance measured from the edge of the cap cut-off with the distance measured from the center of the cap cut-off. The streak record for shot # 738 was used for this test. The calculated tt_{edge} is 0.8304 s which is 0.019 s shorter than the tt_{center} determined using the cut-off from the center of the cap. This small change in the tt produces a small increase in the Hugoniot

pressure ($\sim$ 0.45 GPa) and shock velocity ($\sim$ 0.133 km/s) and a slight decrease in the Hugoniot density ($\sim$ 0.059 gm/cm^3) and particle velocity ($\sim$ 0.007 km/s).

Another possible explanation for the broad convex curvature is that the propagation of lateral release waves from the sample-Mo sidewall interface increases the velocity of the shock front along the outer radius of the container and arrives earlier than the actual shock wave in the liquid. Due to the small diameter of the silicate sample and the large difference in the impedance of Mo versus silicate liquid, release waves from the Mo sidewalls may reach the cap surface before the shock wave that travels through the sample. Early arriving release waves which propagate in from the outer radius of the container will produce an earlier arrival on the cap free surface along its edges and this may account for the convexity of the cap cut-off.

Given our limited understanding of the complex wave interactions within the sample container, four measurements (two near the center and two near the edges of the cap cut-off) of the distance between the driver and cap cut-offs were made. The average distance, d, and its standard deviation were used to determine tt and in this manner the error in the tt is maximized. These errors will propagate through the impedance match calculations and produce relatively large errors in the shock velocity in the sample, U_{ss}, and therefore P and ρ which depend on U_{ss}. Therefore, although the edge effects have not been completely explained, our approximate analysis suggests that within the conservatively large errors placed on d, we have measured the true shock wave transit time through the sample and cap. Detailed modeling of the wave propagations and interactions in the sample assembly may refine the tt and reduce the errors, thereby refining, but not changing the EOS.

Porosity

The basaltic glass cores synthesized for these experiments contained some bubbles. No amount of annealing could completely remove all the bubbles. Along the interface with the Mo crucible, tiny bubbles were particularly prevalent. The formation of the bubbles is attributed to diffusion and oxidation/reduction of Mo and Fe by the reaction

$$3FeO + Mo \rightarrow 3Fe + MoO_3(g). \tag{1.10}$$
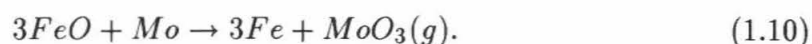
There is concern that such reactions are taking place in the sample container during the pre-heat stage before each shot. The concern is that large bubbles may be forming in the liquid and that the composition of the liquid, particularly its FeO content, may change prior to flyer impact. These effects were checked by heating a sample in the gun tank under the exact same conditions of an experiment and then removing the target for analysis. The target was sliced in half and the composition of the glass determined on the electron microprobe was not significantly different from the original glass (see Table 2.1). Although the composition did not change, there were three large bubbles with diameters ranging from 1 - 2 mm and many minute bubbles along the interface with the Mo driver and cap.

The effect of large bubbles on the experimental measurements may be checked in two ways. First, estimate how quickly it would take a large bubble to rise to the top of the sample space and form a miniscus that would not interfere with the tt measurements. Second, assume there is a bubble along the interface between the liquid and Mo cap and calculate the Hugoniot with an extra gap.

When the sample is completely molten, any large bubble should rise to the top

of the container and form part of the miniscus that is not within the measured shock wave path (Figure 1.1b). The time it takes a bubble to rise from the bottom to the top of the container, approximately 10 mm, can be estimated using Stokes flow as is done for float/sink experiments. The velocity of a bubble of radius, r, in a Newtonian melt of viscosity η is given by

$$V = \frac{2r^2 \Delta \rho g}{9\eta} \tag{1.11}$$

where g is the gravity constant and $\Delta \rho$ is the difference in density between the liquid and bubble. Using a viscosity of 8 Pa s [*Bottinga and Weill,* 1972] for molten MORB at 1400°C, bubbles of diameters, 2 to 0.05 mm, will take 3 to 100 s, respectively, to reach the top of the container. Therefore any large bubbles in the container should rise to the top since the target is heated for $\sim 2 - 5$ minutes before impact.

The calculation of the bubble velocity ignores edge effects of the container and the possibility exists that surface tension along the Mo-sample interface may keep a bubble from rising above the measured shock wave path. Intuitively, a large bubble along the measured shock wave traverse should show a significant increase in d (i.e., an elongated cap cut-off) on the streak record as shown in *Miller et al.* [figure2, 1991a] has shown for a vertical slit streak record that traverses the miniscus in the komatiitic liquid shock wave experiments. To check our intuition, we have recalculated the U_{ss} for each shot, assuming a gap, of thickness $x_{gap} = 0.1x_s$, exists between each sample and cap. The wave velocity in the gap is equal to the free surface velocity of the sample, which is defined as twice the particle velocity, U_{p_s}, of the sample. The new values of U_{ss} are unreasonably high at low pressure and give a linear fit to $U_s - U_p$ with $C_o \sim 3.3$ km/s. The high values of U_{ss} are due to the *tt* (i.e., the

measured distance between the cut-offs on the cap and driver). The tt in the molten MORB, including a gap, is

$$tt = \frac{x_s}{U_{ss}} - \frac{x_{gap}}{2U_{p_s}} - \frac{x_c}{U_{sc}}. \tag{1.12}$$

In the impedance match, tt is rearranged to solve for U_{ss} such that

$$U_{ss} = \frac{x_s}{tt - \frac{x_{gap}}{2U_{p_s}} - \frac{x_c}{U_{sc}}}. \tag{1.13}$$

At low pressure, U_{p_s}, which is determined from the driver-sample impedance match and therefore does not change due to a gap between the sample and cap is low. The lower values of U_{p_s} in Eqn. 1.13 for lower pressure shots, causes more time to be subtracted from tt and therefore U_{ss} gets larger. This indicates that the tt's measured on the streak records are too short to account for a significant gap between the sample and cap and therefore such a large gap does not exist along the measured shock wave path.

The tiny bubbles along the interface with the Mo, however, may still be there during impact. The effect of these bubbles can be estimated in two ways, by doing a more rigorous impedance match and by calculating the porous Hugoniot. The impedance match described in section 1.2.3 is an approximate method for the driver-sample and sample-cap solutions because the zero pressure EOS parameters, Co and s, are used to describe the first material used in each match, even though the first material is in a shocked state. It is assumed that there is a small gap between the shocked and unshocked materials being matched. This small gap allows the shocked material to reduce to its zero pressure state so that the pressure in, the as yet unshocked material, may be derived using the zero pressure EOS parameters of the

shocked material. The rigorous impedance match assumes no such gap exists between the two materials and the shocked material is not reduced to its zero pressure state before the shock front reaches the interface with the unshocked material. In this case the shocked material's high pressure EOS parameters, C^{HP} and s^{HP}, should be used. The high pressure EOS parameters are not known but have been estimated by *Miller* [Appendix 2, 1990]. The Hugoniot curve calculated from a rigorous impedance match is nearly identical to the Hugoniot curve calculated using the approximate impedance match method for our experimental data. Therefore the gap approximation appears to be valid for the MORB liquid. Physically, a small gap may actually exist because of the presence of minute bubbles along the interface with the Mo container, but the calculations suggest that these bubbles have no significant effect on the EOS fit to the data. Therefore whether the interface between the Mo container and the liquid is completely wetted with no gap or has small bubbles along the interface does not effect our fit within the errors of the experiments.

McQueen et al. [1970] studied porous metal EOS deviations from the principal Hugoniot and noted that porous materials produced more scatter in the data ($U_s - U_p$ fit) because of the slightly different initial densities of each sample. The MORB data show a small amount of scatter that may be attributed to slight variations in the initial density of the liquid due to bubbles (Figure 1.4). Using the principal Hugoniot *McQueen et al.* [1970] derived a relation to describe the porous Hugoniot by:

$$P_p = \frac{P_H[1 - \frac{\gamma}{2}(\frac{V_o - V}{V})]}{1 - \frac{\gamma}{2}\left(\frac{V_{oo} - V}{V}\right)} \tag{1.14}$$

where P_p is the porous Hugoniot pressure calculated at a range of compressed volumes, V, V_o is the initial volume of the MORB liquid and V_{oo} is the initial porous

volume of the liquid. The shock and particle velocity for the porous Hugoniot can then be estimated from

$$U_{sp} = V_{oo}[P_p/(V_{oo} - V)]^{1/2} \tag{1.15}$$

$$U_{p_p} = [P_p(V_{oo} - V)]^{1/2}. \tag{1.16}$$

Approximately 2-5% of the volume of the glass contained bubbles from observations of the glass cores and the one sample container that was cross-sectioned (excluding the three large bubbles which were assumed to represent the miniscus or extra free space in the container). Assuming a 5% increase in the volume of the liquid, does not produce a significant change in the Hugoniot curve. In fact, a 50% volume increase would be necessary to cause the porous Hugoniot to be offset to a higher pressure ($\sim$ 1 GPa) from the principal Hugoniot at a density of ~ 3.5 gm/cm^3. Thus if bubbles are present in the liquid, they are not significant enough to effect the pressure-density calculations. The one effect small bubbles may have is on the shock temperature. The bubbles should collapse quickly upon shock compression and this collapse is likely to increase the temperature, thereby increasing the volume slightly so that the porous Hugoniot is always below the principal Hugoniot in P-ρ space [*Melosh*, 1986].

Shock wave rise time and relaxation in the liquid

The rise time of the shock front is assumed to be short and abrupt. This is required to achieve a steady-state profile of the wave on the timescale of the experiment (i.e., the rise time is shorter than the shock travel time). *Duffy* [1992] estimated the rise time of the plastic shock front in his Mo sound wave measurements at 1400°C was on the order of nanoseconds. The rise time is slightly longer at lower pressure ($\sim$ 50 ns at 12 GPa). *Duffy* also simulated the four layer impedance match for the EOS

experiments on molten komatiite and found that at impact velocities < 1 km/s using an Al flyer, the shock front broadened significantly. If the shock wave does not reach a steady state on the timescale of the experiment then the measurements are being done on an unrelaxed liquid. In this case, the EOS cannot be determined using the Rankine-Hugoniot relations because these equations refer to a structurally relaxed state. The Bland number, B, [*Swegle and Grady*, 1985] may be used to estimate the structural state of the liquid, in shock wave experiments. It is defined as

$$B = \frac{3s^2 U_{p_s}^2 U_{ss} x_s}{16 V_o C_o^2 \eta_{eff}} \tag{1.17}$$

where η_{eff} is the effective viscosity of the liquid. The Bland number is basically a ratio of the sample thickness to the distance the wave must travel to reach steady state, so if $B > 1$ then the shock is steady. This relation shows that the rise time is proportional to the viscosity [*Bland*, 1965; *Jeanloz and Ahrens*, 1979] and it has also been shown that the relaxation time is proportional to the viscosity [*Rivers and Carmichael*, 1987; *Kress et al.*, 1989]. Therefore the rise time is proportional to the relaxation time in the liquid and the liquid will be in a structurally relaxed state behind a steady shock front. Using 8 Pa s [*Bottinga and Weill*, 1972] for the viscosity of the MORB, the data from the lowest pressure shot #760 (2.8 GPa) and the highest pressure shot # 738 (20 GPa) and $C_o = 2.10$ and $s = 1.68$, the Bland number ranges from 51 to 2111, much greater than 1, indicating that the shocked liquid is structurally relaxed during the experiment.

1.3.3 Shock Temperatures

In each shock wave experiment, the MORB liquid is superheated upon compression to a shock temperature. Shock temperatures of the molten MORB are needed to correct the Hugoniot to the liquidus of basalt and to define the thermal state of the liquid. Shock temperatures in the molten MORB are not measured in the experiments, but have been calculated using the method of *Miller et al.* [1991a]. The temperature calculations are dependent on the Grüneisen parameter estimated for the liquid. The Grüneisen parameter or thermal pressure, γ_o, is a fundamental thermodynamic variable used to relate temperature and volume as a function of pressure by

$$\gamma_o \equiv -\left.\frac{\partial \ln T}{\partial \ln V}\right|_S = \frac{\alpha_o V_o K_{os}}{C_{p_o}} = \frac{\alpha_o V_o K_{oT}}{C_{v_o}}. \tag{1.18}$$

Using the coefficient of thermal expansion derived earlier, $\alpha_o = 6.3 \times 10^{-5}$, the zero-pressure isentropic bulk modulus, $K_{os} = 11.7 GPa$, derived from Eqn. 1.7 for the linear fit to $U_s - U_p$ and the specific heat at ambient pressure, $C_{po} = 1.50 J/kgK$, determined from the partial molar quantities of *Stebbins et al.* [1984], we calculate a $\gamma_o = 0.18$ for MORB liquid. Given these thermodynamic parameters, the shock temperature is derived from the numerical integration of the following differential

$$\left.\frac{\partial T}{\partial V}\right|_{Hugoniot} = \frac{2\gamma C_p T - V(P - P_o)(1 + \alpha\gamma T) + K_s(V_o - V)}{C_p[\gamma(V_o - V) - 2V]}. \tag{1.19}$$

The high pressure isentropic bulk modulus, K_s, is given by:

$$K_s = \frac{U_s^2}{V_o(1 - s\lambda)}[(1 - \lambda)(1 + s\lambda) - \gamma s\lambda^2] \tag{1.20}$$

where $\lambda = U_p/U_s$. The volume-dependent functional form of the Grüneisen parameter, γ, is given by:

$$\gamma = \gamma_o(\frac{V}{V_o})^q. \tag{1.21}$$

Walsh and Christian [1955] assumed a constant C_v and $q = 1$ to solve Eqn. 1.19 and we have followed this approach. The shock temperature is calculated by incrementing the volume, V, in small steps in the differential. For each step, γ is calculated from Eqn 1.21, K_s from Eqn. 1.20, α from Eqn. 1.18 and C_p from $C_p = C_v(1 + \alpha\gamma T)$.

The calculated shock temperature for the MORB liquid and its isentrope are given in Figure 1.6. The isentrope was calculated using the same thermal parameterization as defined above for the shock temperature calculations. The pressure of the isentrope is determined incrementally from [*McQueen et al.,* 1970]

$$P_S^i = \frac{E_H - E_S^{i-1} - P_H \frac{V}{\gamma} - P_S^{i-1} \frac{\Delta V}{2}}{\frac{\Delta V}{2} - \frac{V}{\gamma}} \tag{1.22}$$

where

$$E_S^i = E_S^{i-1} + (P_S^i + P_S^{i-1})\Delta V/2. \tag{1.23}$$

The temperature of the isentrope, T_S, is given by:

$$T_S = T_o \exp\left(\frac{\gamma_o}{V_o}[V_o - V]\right). \tag{1.24}$$

Figure 1.6 compares the temperature of the shocked MORB liquid with an extrapolated liquidus curve for an olivine tholeiite of similar composition. The tholeiite liquidus is only experimentally determined to $\sim$4 GPa [*Stern et al.,* 1975]. If the slope of the liquidus remains constant above 4 GPa, then it appears that the shocked MORB liquid is metastable (i.e., below the tholeiite liquidus) between 3.5 and 13.5 GPa. In order to compare the molten MORB Hugoniot at conditions relevant to the earth's upper mantle, we must correct the shock temperature of the liquid to the extrapolated temperature of the basalt liquidus. This is done using a Mie-Grüneisen

thermal pressure correction of the form:

$$\frac{\Delta T}{\Delta P} = \frac{1}{\gamma \rho C_v} \tag{1.25}$$

where ΔT is the temperature difference between the Hugoniot and basalt liquidus and ΔP is the pressure difference between the Hugoniot and liquidus. Such a thermal correction adjusts the MORB Hugoniot in $P - \rho$ space slightly and all the comparisons that follow will use this temperature corrected Hugoniot, that for lack of a better name, we will call the Liquidus MORB.

1.4 Discussion

1.4.1 Comparison with Low Pressure, Static Compression Experiments

The density of various mafic to ultramafic natural melts have been measured directly using the float/sink technique for different marker spheres in the liquid under static compression at relatively low pressure [*Agee*, 1992; *Agee and Walker*, 1988; *Kushiro*, 1986; *Sharpe et al.*, 1982; *Kushiro*, 1981; *Murase*, 1981; *Fujii and Kushiro*, 1977; *Kushiro et al.*, 1976]. A comparison of these static compression measurements with the MORB liquid indicates that basaltic liquids are very compressible. Figure 1.7 shows MORB compared to float/sink density measurements for an aluminous tholeiite from the chilled margin of the Bushveld [*Sharpe et al.*, 1983]. The composition of the aluminous tholeiite is similar to the MORB (Table 1.6) and the MORB Hugoniot has been corrected for the temperature at which the static compression experiments were done ($1450^\circ C$). Both experimental data sets are corrected for their different initial densities by normalizing the measured density to the calculated starting den-

Figure 1.6: Shock temperature (determined by numerical integration of Eqn. 1.19) and isentrope of MORB liquid initially at 1400°C, with $\rho_o = 2.66$ gm/cm^3. $\gamma_o = 0.18$, derived from the linear $U_s - U_p$ fit, was used for the initial value of the Grüneisen parameter and γ/V was held constant for these calculations. The liquidus curve is for a tholeiite of similar composition as our MORB [Stern et al., 1975]. The portion of the liquidus that is dotted is an extrapolated extension of the liquidus slope beyond the experimental data.
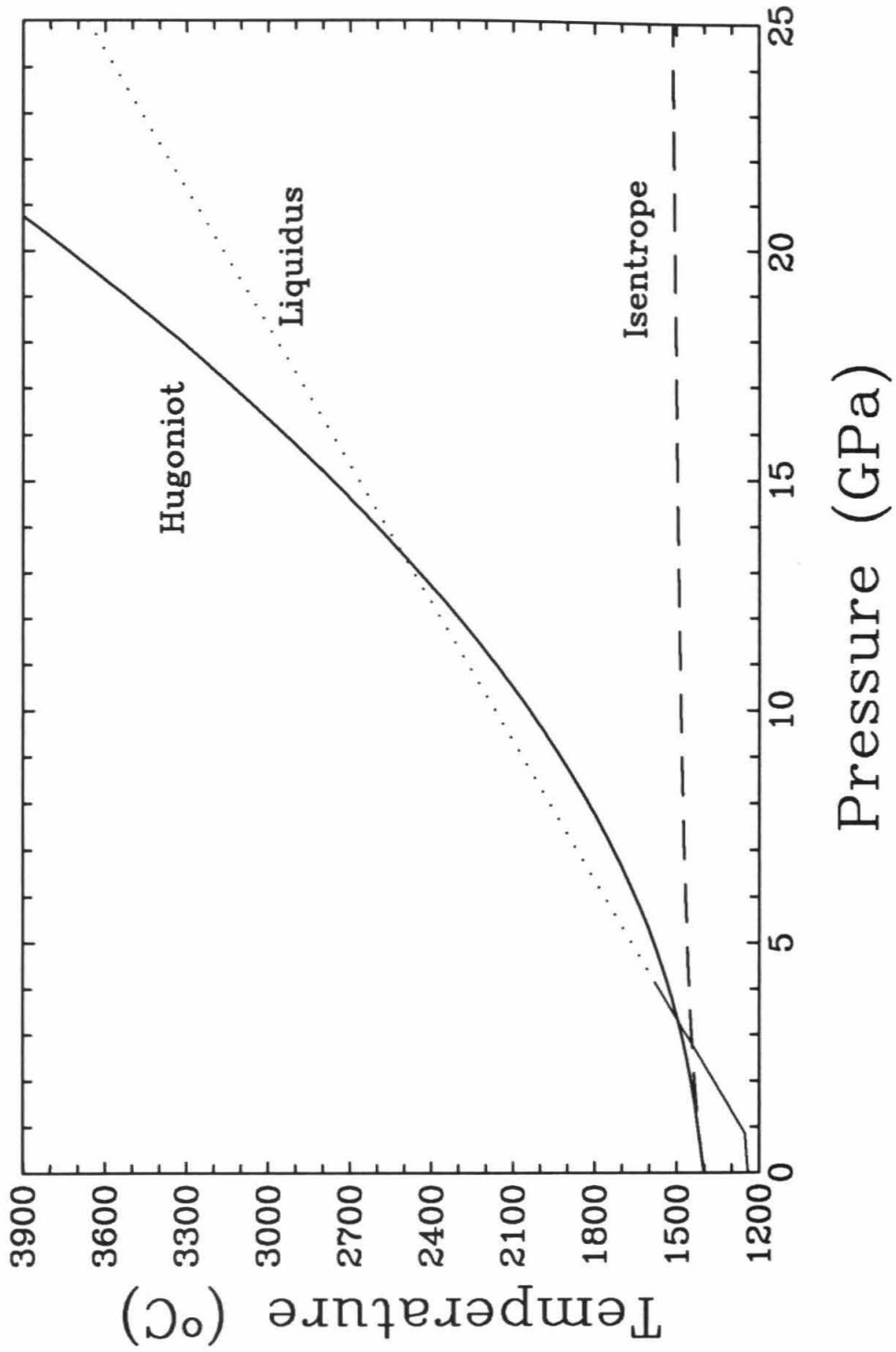
sity. This allows a direct comparison of the results and shows that both liquids are very compressible and reach a similar density at $\sim$2 GPa. Figure 1.8 shows a similar comparison between the MORB liquid and the float/sink measurements of *Fujii and Kushiro* [1977] for an olivine tholeiite from Kilauea (KOT). The static compression experiments were done at 1400°C and the MORB liquid density has been corrected to this isothermal condition. The densities have also been normalized to the initial density calculated for each composition to allow a direct comparison of the results which show that the shock wave experiments done at higher pressures are consistent with the static compression experiments done at lower pressures on similar basaltic compositions.

1.4.2 Comparison with Ultrasonic Measurements

The extrapolated bulk sound speed from the linear fit to $U_s - U_p$ may be compared with the measured bulk sound speed of basaltic liquids determined ultrasonically. Table 1.7 shows the measured sound speeds of some basaltic melts with similar compositions to our MORB. These bulk sound speeds are considerably faster than the sound speed, 2.10 km/s, extrapolated from the shock wave experiments, except for an earlier determination of C_o in a Kilauea olivine tholeiite (KOT) measured at a lower frequency (0.1 MHz) and lower temperature (1250°C) than later measurements (> 1 MHz and $> 1300^{o}$C). Temperature and compositional differences of our MORB can be accounted for by using a linear ideal mixing model to estimate C_o [*Rivers and Carmichael*, 1987]

$$C_o = \sum_{i=1}^{n} x_i C_i \tag{1.26}$$

Wt%	KOT[a]	AT[b]
SiO_2	50.1	52.42
TiO_2	2.60	0.79
Al_2O_3	12.56	15.56
FeO*	10.79	10.64
MgO	9.39	6.67
CaO	10.88	10.20
K_2O	0.48	0.32
Na_2O	2.33	2.97
TOTAL	99.5	99.57

* Total Fe as FeO

[a] Kilauea Olivine Tholeiite: *Kushiro et al.*, 1976

[b] Aluminous Tholeiite: *Sharpe et al.*, 1983

Table 1.6: Major oxide composition of basalts used for float/sink measurements of density.
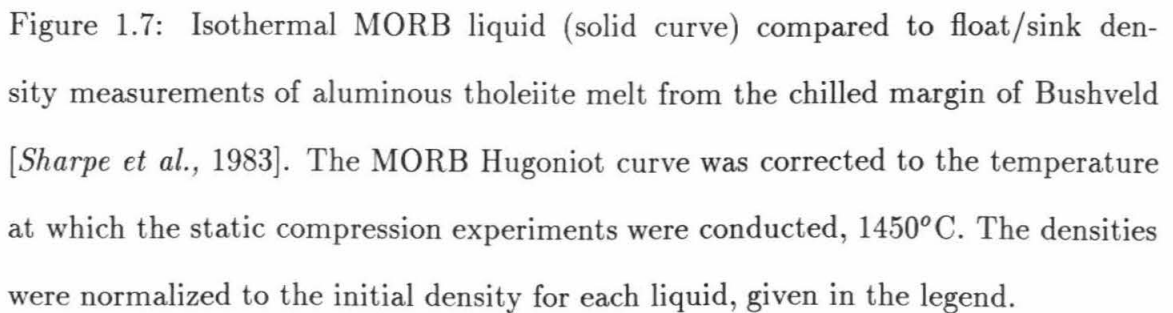
Figure 1.7: Isothermal MORB liquid (solid curve) compared to float/sink density measurements of aluminous tholeiite melt from the chilled margin of Bushveld [*Sharpe et al.*, 1983]. The MORB Hugoniot curve was corrected to the temperature at which the static compression experiments were conducted, 1450°C. The densities were normalized to the initial density for each liquid, given in the legend.
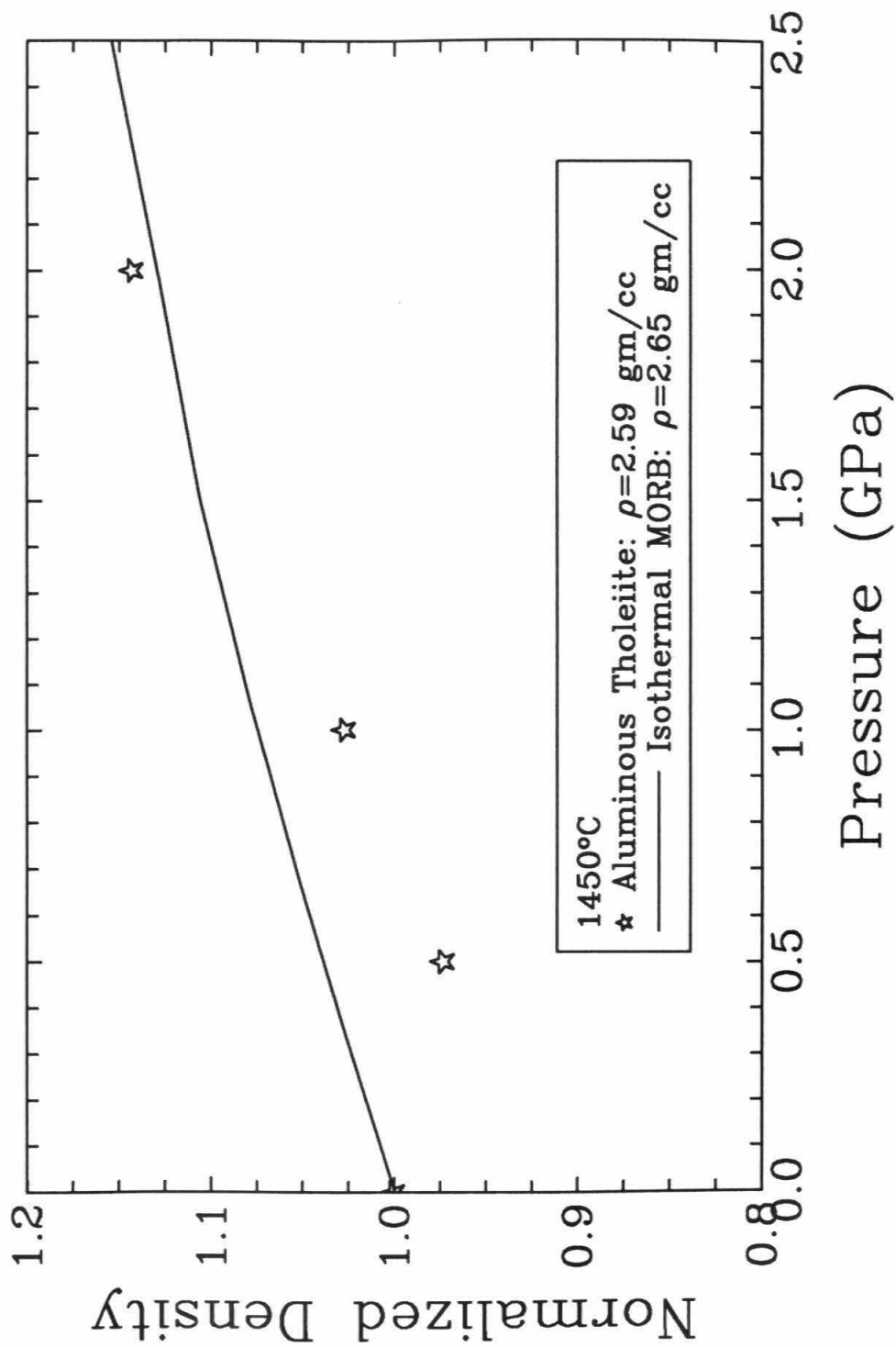
Figure 1.8: Isothermal MORB liquid (solid curve) compared to float/sink measure-ments of liquid Kilauea olivine tholeiite (KOT, open diamonds) [*Fujii and Kushiro,* 1977]. The MORB Hugoniot curve was corrected to the temperature at which the static compression experiments were conducted, 1400° C. The densities were normal-ized to the initial density for each liquid, given in the legend.
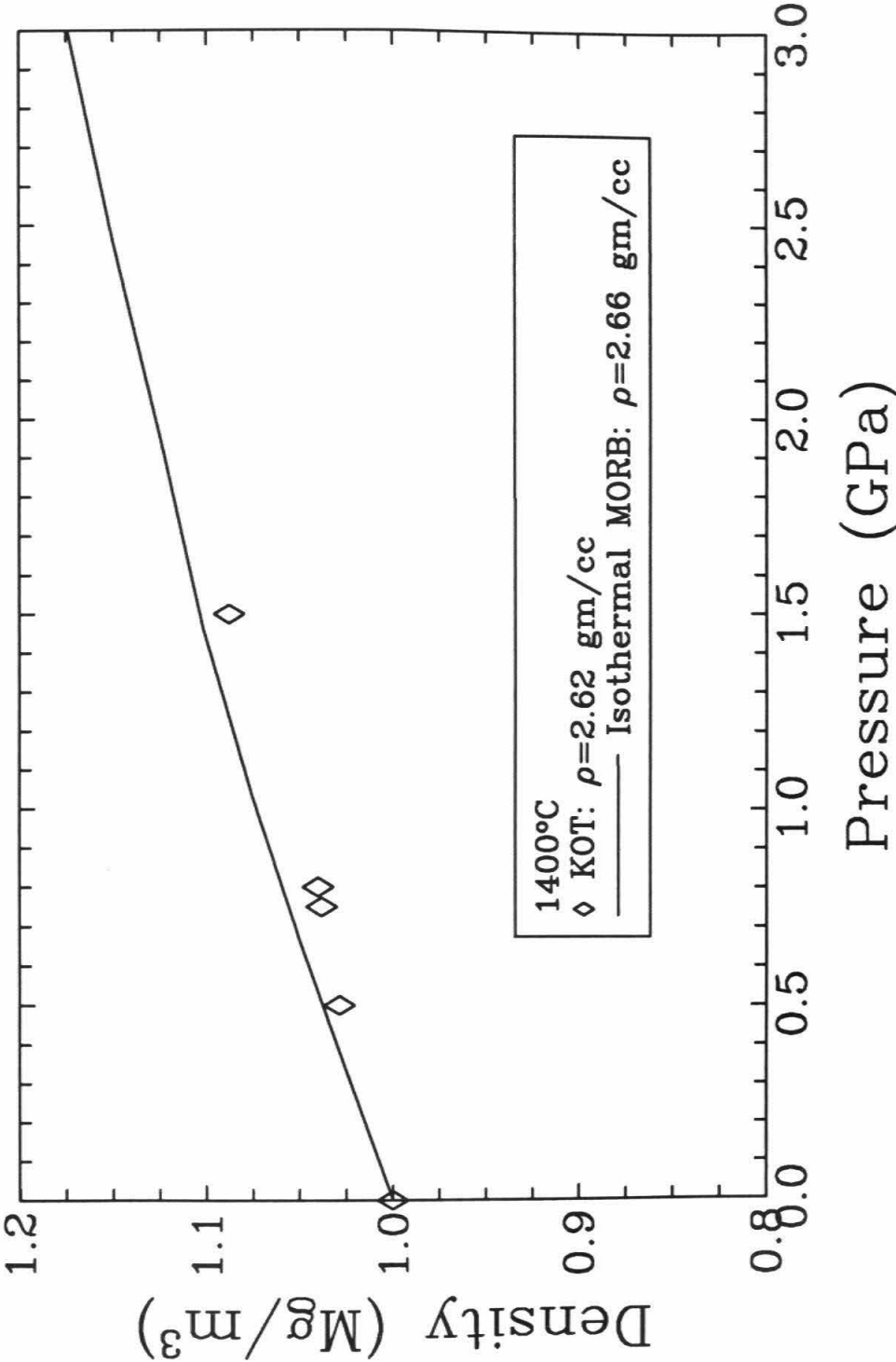
where x_i is the mole fraction of the oxide and C_i is the coefficient of the sound speed for each oxide. *Rivers and Carmichael* [1987] determined the values of C_i for all the major oxides in silicate liquids by doing a least squares fit to the available ultrasonic data. *Kress and Carmichael* [1991] adjusted these coefficients slightly to account for the effects of oxygen fugacity and these coefficients were used to calculate the bulk sound speed for the MORB liquid at 1400°C. The calculated bulk sound speed for the MORB composition is 2.65 ± 0.02 km/s. This value is still higher than our extrapolated result.

There are several possible reasons why the extrapolated shock wave C_o does not agree with the ultrasonic results, including experimental difficulties, model parameters and compositional effects. The bulk sound speeds of the liquids were determined at different frequencies for the two methods, so it is important to establish that both methods were measuring the velocity in a relaxed liquid where the velocity does not depend on the frequency. *Rivers and Carmichael* [1987] and *Kress et al.* [1989] have shown that the frequencies at which their ultrasonic measurements were made ($1 - 3$ MHz) are within the range where silicate liquids are relaxed. We have already shown that the shock wave experiments were done on relaxed liquids, given that the shock wave rise times are within 10^{-8} to 10^{-9} s.

Besides the frequency differences, ultrasonic measurements actually have similar experimental difficulties as our shock wave experiments because ultrasonic interferometry requires high temperatures and a suitable container for the liquid. Most ultrasonic set-ups use Mo crucibles and Mo buffer rods and therefore the liquid-container interactions will be similar to the pre-heat stage in our shock wave exper-

C_o [km/s]	T [^{o}C]	Composition
2.4	1400	Columbia River Basalt (CRB)[a]
2.35	1400	Galápagos Olivine Basalt (GOB)[a]
2.2	1250	Kilauea Olivine Tholeiite (KOT)[b]
2.60	1400	Kilauea Olivine Tholeiite (KOT)[c]
2.53	1300	Alkali Olivine Basalt, Hawaii (OW76)[d]
2.588	1349	Olivine Basalt, East Uganda (CMS5)[e]
2.55	1400	Oceanic Island Tholeiite, Hawaii (CMS4)[f]
2.60	1400	Hawaiian Olivine Tholeiite (Kil-2)[g]
2.60	1432	Hawaiian Olivine Tholeiite + Fe[h]
2.535	1432	Fe-rich Labrador Basalt[h]

[a] *Murase and McBirney, 1973;* [b] *Murase et al., 1977;* [c] *Murase, 1981*

[d] *Rai et al., 1981;* [e] *Manghnani et al., 1986;* [f] *Rai et al., 1981*

[g] *Rivers and Carmichael, 1987;* [h] *Kress and Carmichael, 1991*

Table 1.7: Measurements of bulk sound speed at the given temperature for basaltic melts determine by three different laboratory groups. The groups are separated by the horizontal lines.

iments. *Rivers and Carmichael* [1987] noted significant Fe loss and Fe-plating on the buffer rod in some experiments involving Fe-rich liquids. These problems could effect the velocity measurements because the path length must be precisely known and the composition of the liquid needs to be known in order to calculate its initial density at temperature. Also bubbles may occur along the interface with the Mo and liquid as have been noted in our experiments, but we could not find a discussion of this potential problem in any of the ultrasonic literature. We note that while our concerns about liquid container interactions are important, these same concerns for the ultrasonic measurements may be more significant since the liquid is kept at high temperature for a longer period of time. *Rivers and Carmichael* [1987] attempted to correct for melt-container interactions and we can only assume that these corrections are appropriate.

The concerns about experimental conditions will not explain all the differences between the bulk sound velocities, but some of the discrepancy may be explained by the model assumptions used to determine C_o. *Rivers and Carmichael* [1987] assumed that the oxides in the melts mix ideally in order to use their linear model (Eqn. 1.26). *Bottinga et al.* [1982; 1983] suggested that Al_2O_3 shows an excess volume of mixing and cannot be described by simple ideal mixing in natural melts. Also the data used to determine the sound speed coefficients only included 3 natural melts (out of 65) and the majority of the other melts were binary, oxide-SiO_2 or ternary 2 oxides-SiO_2 . Many of the oxides used in the fit are also not found in basalts, such as Li_2O. Thus it seems that the only way to resolve the compositional differences of the MORB is to measure its bulk sound speed directly using ultrasonics.

In terms of the shock wave model assumptions, the empirical, linear $U_s - U_p$ fit, which is appropriate for the bulk of shock wave measurements on solids may not be the most appropriate EOS for molten MORB. Using a quadratic fit and the ultrasonically modeled, C_o, as a datapoint, we get a decent fit to the data (Figure 1.4) with $s = 0.29 \pm 0.24$ and $s' = 0.72 \pm 0.21$. These parameters and $\rho_{os} = 2.66$ give $K_{os} = 18.68 \pm 0.35$ $K'_{os} = 0.16 \pm 0.96$ and $K'_{os} = 1.16 \pm 0.36$. The χ^2 for the quadratic fit is 7.7, but the statistical goodness of fit is less than the linear (i.e., <50% confidence for the quadratic, versus 50-75% confidence for the linear). Using the EOS parameters from the quadratic fit, we can determine the Hugoniot curve (Figure 1.5). This curve is not much different than the original, linear fit Hugoniot except at high pressures where the quadratic fit Hugoniot shows a significant stiffening (flattening of the curve). Although we are able to get the ultrasonic C_o by including the modeled bulk sound speed as a datapoint, it is not the best fit to the experimental data and it assumes a priori knowledge of the zero pressure point. For these reasons, we have chosen to use our linear fit to describe the EOS parameters.

1.4.3   Compositional Effects

The low bulk sound velocity and very compressible nature of our MORB liquid versus other basic silicate liquids may be due to compositional differences. Using previous shock wave experiments on a FeO-free basaltic analog melt, $An_{36}Di_{64}$ [*Rigden et al.*, 1988] and a MgO-rich, ultramafic melt, komatiite [*Miller et al.*, 1991a] and the ultrasonic data on komatiitic, basaltic and andesitic melts we can determine which of the major oxides might contribute to the differences in the EOS properties of these liquids. Tables 1.8 and 1.9 summarize the major element composition and

EOS parameters, respectively from the shock wave experiments and for a Hawaiian olivine tholeiite (Kil-2) whose properties have been measured ultrasonically [*Rivers and Carmichael*, 1987].

SiO_2 and Al_2O_3

SiO_2 , the most abundant oxide in silicate liquids and Al_2O_3 , a more varaible oxide component undergo coordination changes that would have a significant effect on the density of the melt. These effects may be seen in the shock wave measurements of $An_{36}Di_{64}$ and MORB. The Hugoniot for $An_{36}Di_{64}$ using a linear $U_s - U_p$ fit and a quadratic $U_s - U_p$ fit is shown in Figure 1.9.

The stiffening of the Hugoniot at high pressure is similar to our results for molten MORB. As *Rigden et al.* [1988] proposed, this stiffening may be due to coordination changes in SiO_2 and Al_2O_3 . With increasing pressure the Si^{+4} and Al^{+3} present in four-fold coordination gradually are transformed to six-fold coordination. The coordination changes are suggested to be gradual because there is no significant change in the slope of the Hugoniot or the fitted $U_s - U_p$ relation for $An_{36}Di_{64}$ or MORB. The quadratic fits to $U_s - U_p$ for $An_{36}Di_{64}$ and MORB liquids have very low K''s and there is a significant contribution from K'' These results are atypical of EOS measurements for most silicate solids, but are not inconsistent with the nature of a silicate liquid. A low K' indicates a very soft material that is easily compressed until it has reached a structural state similar to its higher pressure analog solid state. One important and unusual example of a soft (i.e., low K and K') solid is fused quartz. *Peselnick et al.* [1967] measured the bulk modulus and its pressure derivative for fused quartz and found that K_o was very small and K' was negative

Wt%	$An_{36}Di_{64}{}^{a}$	Komatiite[b]	MORB[c]	Kil-2[d]
SiO_2	50.5	45.4	48.3	51.62
TiO_2	—-	0.4	1.05	3.34
Al_2O_3	15.4	8.2	17.8	13.90
FeO^*	—-	8.6	9.0	10.98
MgO	10.5	26.6	7.3	6.39
CaO	23.9	7.8	12.5	10.31
K_2O	—	0.3	0.1	0.72
Na_2O	—	1.1	2.52	2.74
MnO	—	0.1	0.16	—-
Cr_2O_3	—	0.4	—	—
TOTAL	100.3	98.8	98.9	100.0

Table 1.8: Major element composition of three silicate liquids used for the shock wave experiments. The $An_{36}Di_{64}$ [*Rigden et al.*, 1988] and the komatiite [*Miller et al.*, 1991a] were prepared from pure oxide mixtures in the appropriate proportions. The MORB is a natural melt and was prepared for each shot as described in section 1.2.1. The Hawaiian olivine tholeiite composition [*Rivers and Carmichael*, 1987] was determined after the ultrasonic experiment and may be effected by reactions with the Mo crucible (the initial composition was not given).

EOS	An$_{36}$Di$_{64}$[a]	Komatiite[b]	MORB[c]	Kil-2[d]
T [K]	1673	1823	1673	1708
ρ_{oT} [gm/cc]	2.61 ± 0.03	2.74 ± 0.01	2.66 ± 0.01	2.65
C_o [km/s]	2.94 ± 0.05	3.13 ± 0.03	2.10 ± 0.15	2.605 ± 0.005
s []	1.29 ± 0.06	1.47 ± 0.03	1.68 ± 0.19	—
Kos [GPa]	22.5 ± 0.8	27.0 ± 0.6	11.7 ± 1.7	17.9
K' []	4.16 ± 0.24	4.9 ± 0.1	5.7 ± 0.7	—
$\alpha \times 10^{-5}$ [K^{-1}] [e]	6.10 ± 1.34	8.0 ± 1.7	6.34 ± 1.30	6.7
Cp [J/gmK]	1.59 ± 0.03	1.67 ± 0.05	1.50 ± 0.03	1.46
γ_o []	0.33 ± 0.07	0.47 ± 0.10	0.18 ± 0.04	0.31

[a] Hugoniot EOS: *Rigden et al.*, 1988

[b] Hugoniot EOS: *Miller et al.*, 1991a

[c] Hugoniot EOS: This study

[d] Hawaiian Olivine Tholeiite: *Rivers & Carmichael*, 1987

Table 1.9: The EOS parameters were determined by shock wave measurements or ultrasonics with the initial density and specific heat for each liquid estimated from the partial molar quantities of *Lange and Carmichael* [1987] and *Stebbins et al.* [1984].

Figure 1.9: Comparison of Hugoniot determined from the linear relation $U_s = 2.94 + 1.50U_p$ with the Hugoniot determined from the quadratic relation $U_s = 3.34 + 0.67U_p + 0.34U_p^2$ for $An_{36}Di_{64}$ liquid.
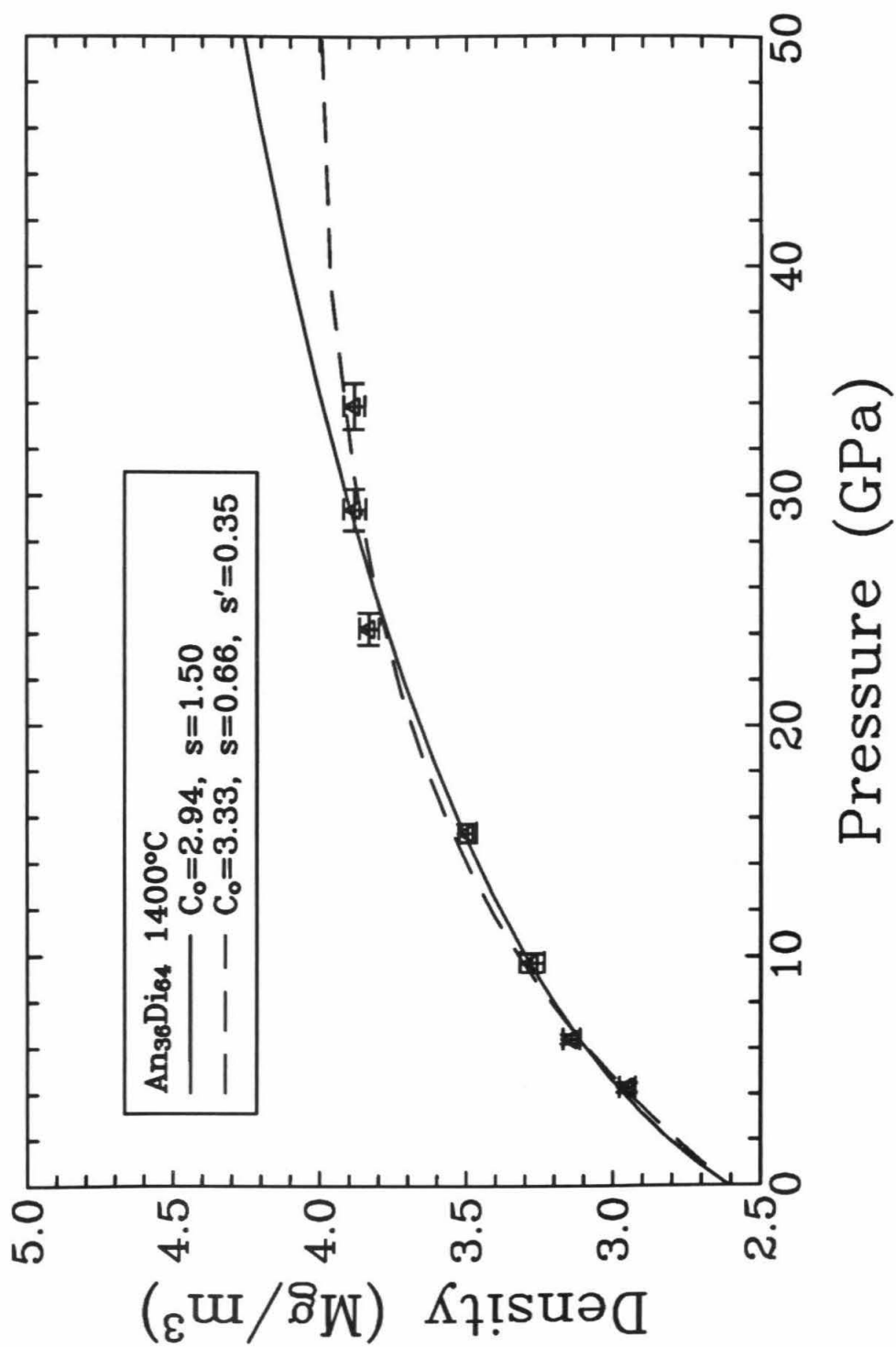
(-6.15) at low pressures. The nature of the fused quartz is relevant and comparable to the structural nature of the $An_{36}Di_{64}$ and MORB liquids. The low K and K' indicate the significant compressibility allowed due to the presence of the readily deformable SiO_2 bond.

At approximately 28 GPa, these transformations in $An_{36}Di_{64}$ liquid appear to be essentially complete and the melt has reached its high pressure structural state as shown by the coincidence of the liquid Hugoniot with the mixed dense oxide Hugoniot at this pressure [*Rigden et al.* 1988]. For the MORB liquid, if the stiffening is related to the same effect then it appears that the MORB liquid reaches it's high pressure structural state more rapidly (i.e., at lower pressures, $\sim$17 GPa). We calculated the high pressure dense oxide Hugoniot for the MORB liquid using the additive volume approach of *Rigden et al.* [1988]. Only five high pressure oxide phases, stishovite, corundum, wüstite, lime and periclase, that account for 94 wt% of the MORB, were used and their parameters are given in Table 1.10. The dense oxide Hugoniot crosses the MORB liquid Hugoniot where the MORB liquid begins to stiffen at 17 GPa (Figure 1.5). This is consistent with the conclusions of *Rigden et al.* [1988].

Besides the pressure-induced coordination changes in SiO_2 and Al_2O_3, Al_2O_3 also seems to correlate with C_o for the An-$An_{36}Di_{64}$ and basalt liquids examined ultrasonically by *Secco et al.* [1991] and *Manghnani et al.* [1986], respectively. They noted that C_o and therefore K_{os} decrease with increasing Al_2O_3. We have plotted this relation in Figure 1.10 for these compositions and komatiite melts using ultrasonic and shock wave results. Given that our MORB is quite Al_2O_3 enriched (Table 1.8) it is not surprising that we get such a low C_o.

	SiO$_2^a$	Al$_2$O$_3^b$	FeO^{c,d}	MgO^b	CaO^d
ρ_o [gm/cc]	4.29	3.988	5.864	3.584	2.245
Kos [GPa]	316.0	252.7	158.0	162.7	112.0
K$'$ []	4	4.3	4	4.27	4.8
$\alpha \times 10^{-5}$ [K^{-1}]^e	3.66	1.64	3.3	3.15	2.9
γ_o []	1.25	1.32	1.63	1.32	1.51

[a] *Weidner et al.*, 1982; *Lyzenga et al.*, 1982

[b] *Anderson et al.*, 1968

[c] *Jeanloz & Sato-Sorenson*, 1986

[d] *Jeanloz & Ahrens*, 1980

[e] *Rivers & Carmichael*, 1987

Table 1.10: EOS parameters of dense oxides used to calculate the dense oxide Hugoniot for the MORB composition.

Figure 1.10: Bulk sound speed versus Al_2O_3 for ultrasonic measurements of komatiitic (open diamonds), basaltic (open triangles) and andesitic (open squares) melts. Three different laboratories determined these velocities, Manghnani's group in Hawaii [*Rai et al.*, 1981; *Rai et al.*, 1982; *Manghnani et al.*, 1986] Carmichael's group at Berkeley [*Rivers and Carmichael*, 1987; *Kress and Carmichael*, 1991] and McBirney's group at Oregon [*Murase and McBirney*, 1973; *Murase et al.*, 1977; *Murase*, 1981]. Also plotted are the extrapolated sound speeds from shock wave measurements of komatiite [*Miller et al.*, 1991a], $An_{36}Di_{64}$ and anorthite [*Rigden et al.*, 1988] and my basalt (open stars).
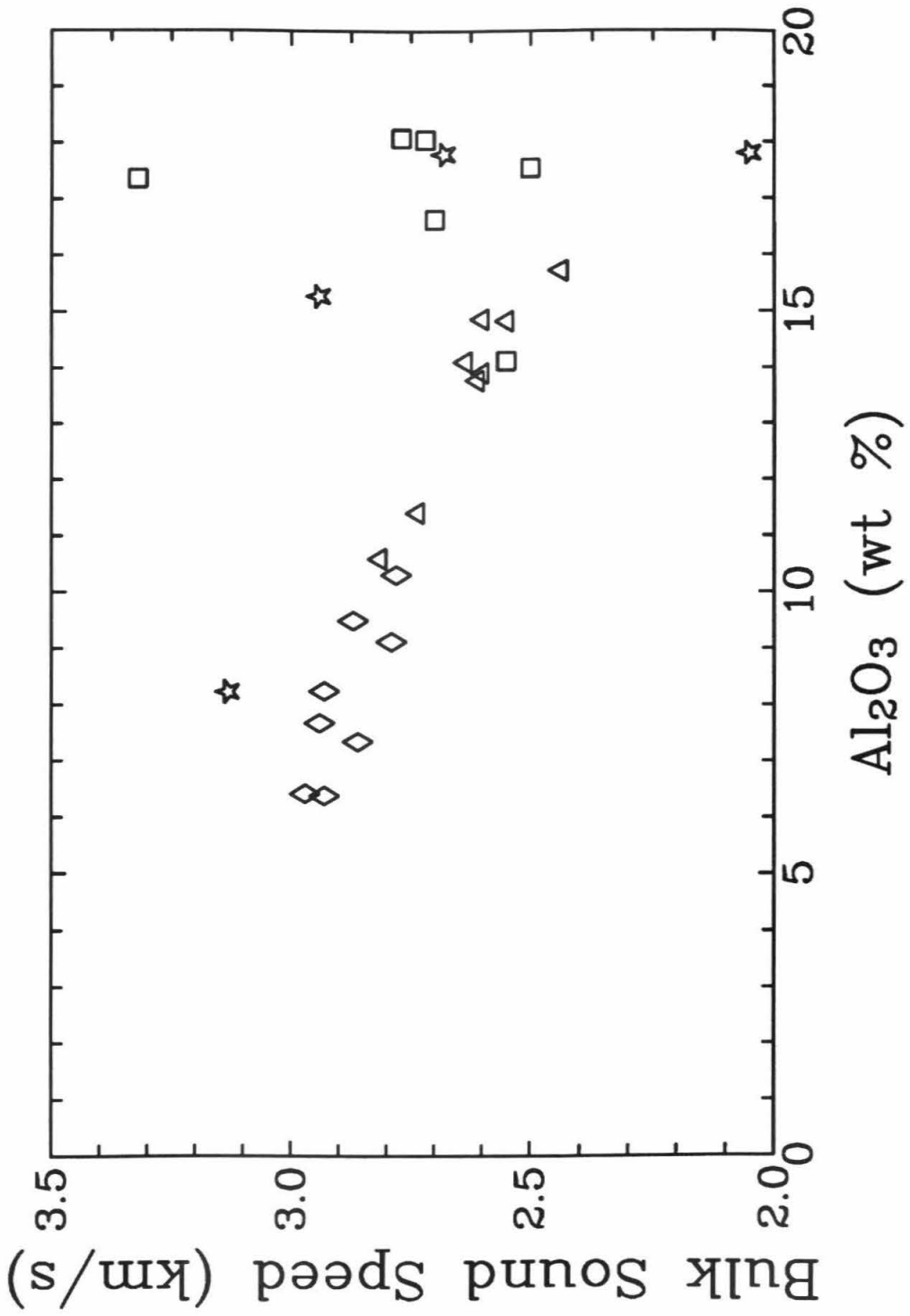
MgO and CaO

SiO_2 and Al_2O_3 are probably two of the major oxides influencing the compressibility of our MORB liquid, but some other oxides also play a role in this natural melt's structural state. *Rivers and Carmichael* [1987] noted that C_o varies as a function of alkali (e.g., Na and K) and alkaline earth (e.g., Ca and Mg) concentrations for a wide range of melt compositions. They noted that C_o decreases as the cation radius increases. Also by comparing their calculated sound speed coefficients for each oxide it can be seen that TiO_2 and FeO have much lower C_i's than CaO and MgO. *Rivers and Carmichael* [1987] noted that the calculated $(\partial V_i/\partial P)_T$ for FeO is much greater than MgO (in fact for MgO the derivative is negative) even though their volumes are comparable. The ultrasonic data show a consistent trend of increasing C_o with increasing MgO content (Figure 1.11).

The influence of MgO with increasing pressure can clearly be seen by comparing the molten MORB Hugoniot with the molten komatiite Hugoniot (Figure 1.12). Although the MORB is initially at a lower density and temperature, the liquid compresses more rapidly than the komatiite and overtakes the komatiite at a low pressure of $\sim$2.5 GPa. The komatiite has greater than three times more MgO and only half as much Al_2O_3 by weight as the MORB. A similar situation, a low pressure crossover for a denser, hotter liquid, occurs for the An ($CaAl_2Si_2O_8$) and Di ($CaMgSi_2O_6$) Hugoniots determined by *Rigden et al.* [1987] (Figure 1.13) due to the differences in MgO and Al_2O_3 content.

The influence of CaO can be seen by comparing the $An_{36}Di_{64}$ with the two basalts. The large amount of CaO in the $An_{36}Di_{64}$ compared with the basalts,

Figure 1.11: Bulk sound speed versus MgO for ultrasonic measurements of komatiitic, basaltic and andesitic melts. See Figure 1.10 for references.
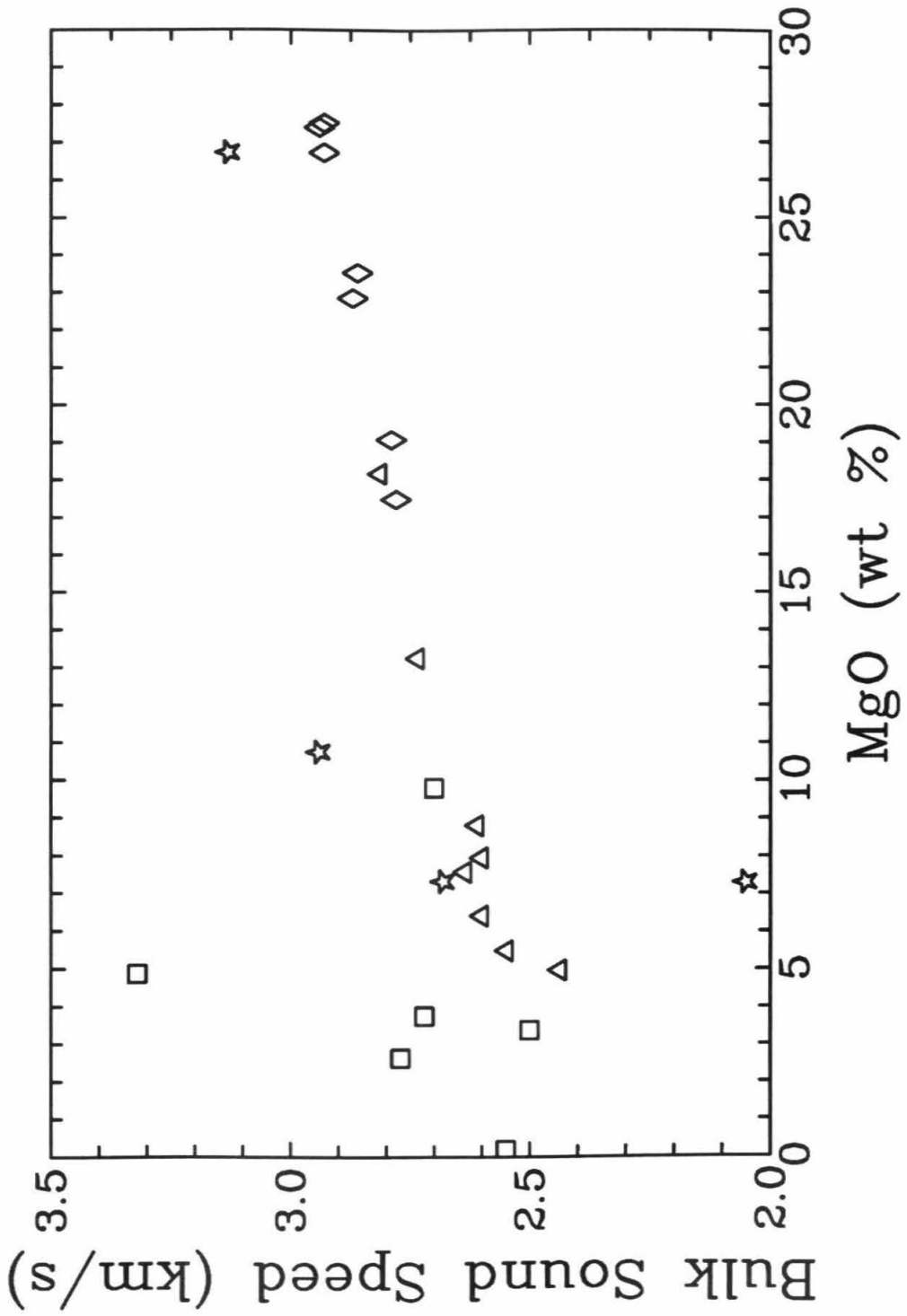
Figure 1.12: Hugoniot curves of MORB liquid compared to komatiite liquid deter-

mined by *Miller et al.,* [1991a].
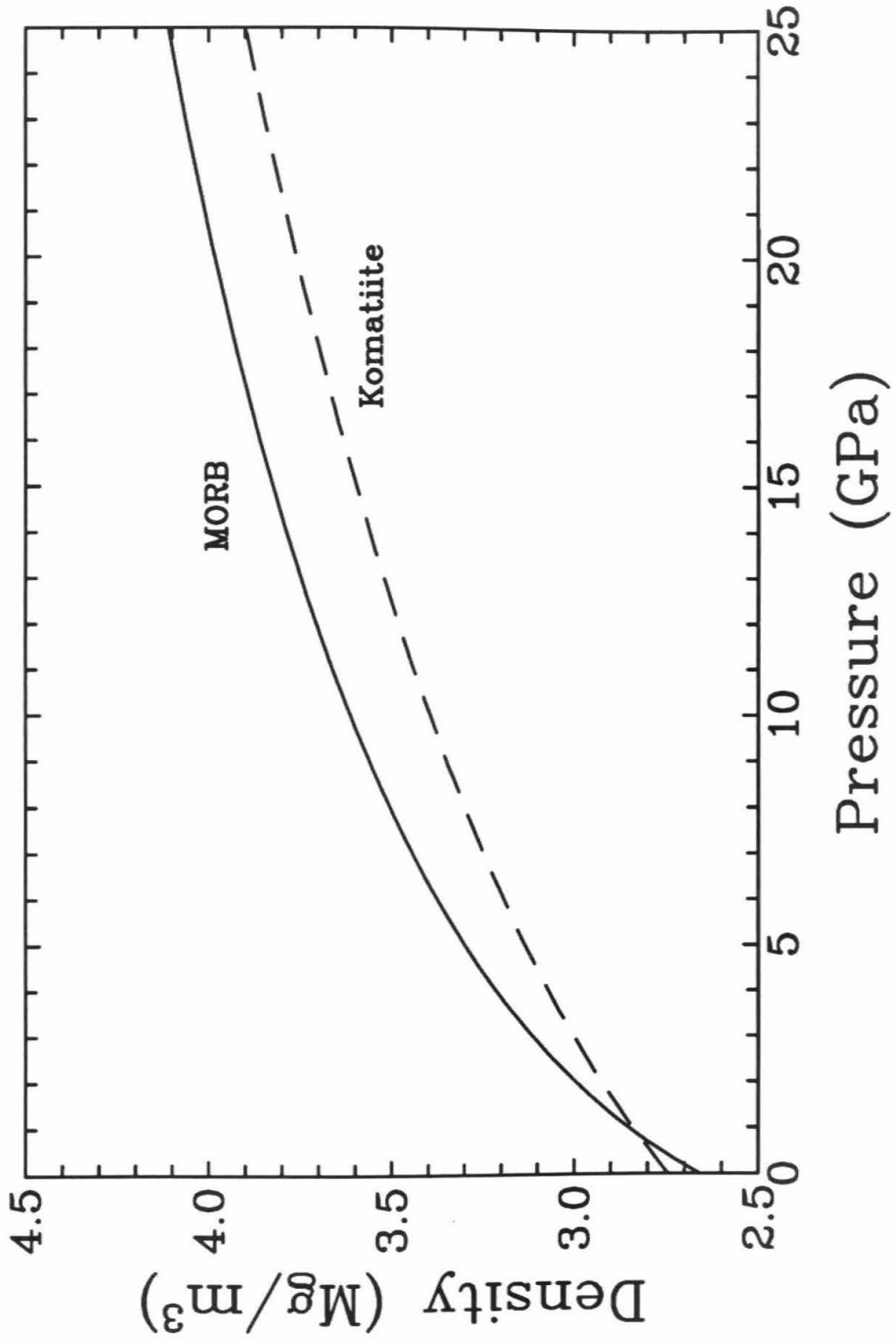
Figure 1.13: Hugoniot curve of MORB liquid from linear $U_s - U_p$ fit compared to Hugoniot curves from linear $U_s - U_p$ fits for $An_{36}Di_{64}$, diopside and anorthite determined by *Rigden* [1986].
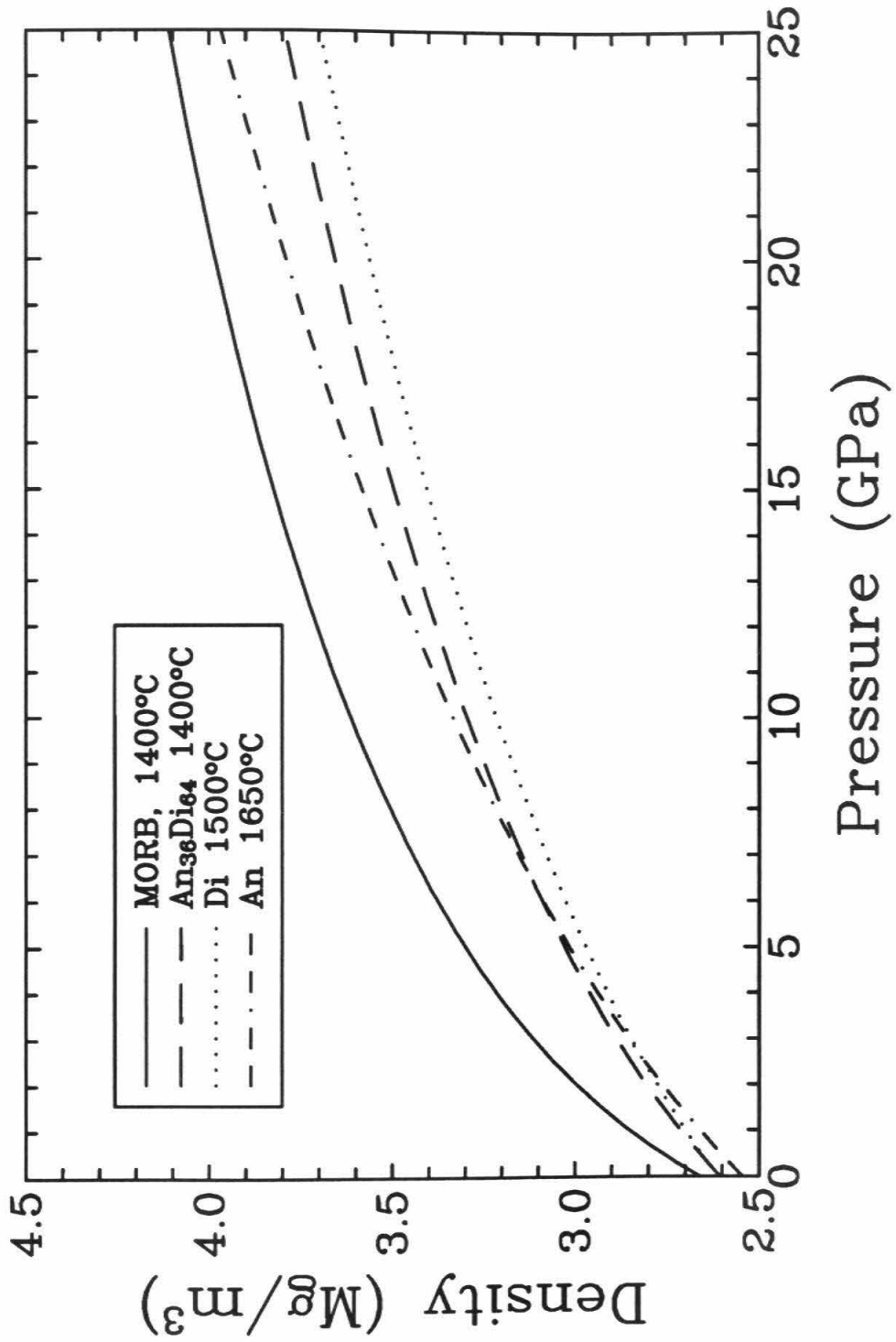
keeps the C_o for $An_{36}Di_{64}$ higher than the C_o for the basalts. CaO behaves like MgO and represents a tightly packed bond with limited compressibility. *Secco et al.* [1991] noted that small cations like Mg^{+2} and Ca^{+2} result in smaller cation-oxygen-cation bond angles and more polymerized units. These tightly packed units limit the amount of continued structural rearrangement available within the melt as pressure is increased. Therefore, the MORB liquid is very compressible because it is enriched in SiO_2 and Al_2O_3 and depleted in MgO compared to more ultramafic melts, like komatiites, and these compositional effects have important implications for basalt genesis.

1.5 Implications

1.5.1 Comparison with PREM

In order to give an overall perspective of the relation of the Liquidus MORB to the bulk earth we may qualitatively compare it to the Preliminary Reference Earth Model (PREM) [*Dziewonski and Anderson,* 1981] (Figure 1.14). This is done with the understanding that the composition of the bulk earth (i.e., the density of the bulk earth) is not the same as the composition of the solid phase that would be in equilibrium with a MORB liquid at a particular depth. At ~0.5 GPa (15 km) the MORB liquid crosses the solid earth and until 6 GPa (180 km) the molten MORB is less dense than the solid mantle. Within this region any parcel of molten MORB should buoyantly rise to the near surface of the earth and this pressure range is consistent with the suggested range for MORB genesis in the mantle. The density crossover at 6 GPa is consistent with the predictions of *Rigden et al.* [1984]

estimated using the EOS of a basaltic analog. From 6-7 GPa, the MORB liquid is slightly denser than the mantle near the base of the low velocity zone ($\sim$180-200 km). These relations suggest that the low velocity zone (LVZ) may be a region of magma concentration, although the composition of the partial melt will not be basaltic. Below the low velocity zone, the MORB liquid is denser than the surrounding mantle until it intersects the 670 km discontinuity. This result is quite unlike komatiite liquid which is lighter and therefore buoyant throughout the entire mantle [*Miller et al.*, 1991b]. If there was any MORB-like melt present in the mantle region between the LVZ and the 670 km discontinuity it may stagnate at this depth, whereas a diapir of komatiite liquid would segregate and buoyantly rise up through the mantle. The decreasing buoyancy (i.e., increasing density) with depth of a partial melt as a function of decreasing MgO will have important implications for models of basalt genesis that require a deep and/or an enriched source. If a mafic magma is inhibited from rising from below the LVZ in the upper mantle then any primary magmas suggested to arise from deeper levels must be ultramafic. If mafic magma is dragged down below the LVZ by subduction, convective circulation or some other process, then it would provide a source of enrichment between the LVZ and the 670 km discontinuity because any mafic magma would be forced to re-equilibrate given the small density contrast between the melt and solid.

1.5.2   MORB Genesis

Mid-ocean ridge basalts represent the shallow, fractionated end-member lavas derived from the adiabatic upwelling and focussing of primary partial melts at oceanic spreading ridges. The physical process is a passive one, driven strictly by exten-

Figure 1.14: Liquidus MORB compared to PREM. The mineral phases that are in equilibrium with a MORB liquid were estimated from the phase relations of *Takahashi and Kushiro,* [1983], *Takahashi* [1986] and *Stern et al.* [1975]. The curves were generated using the EOS data for each mineral given in Table 1.11. The dashed part of the curve indicates the pressure range where the mineral is stable and in equilibrium with a MORB liquid.
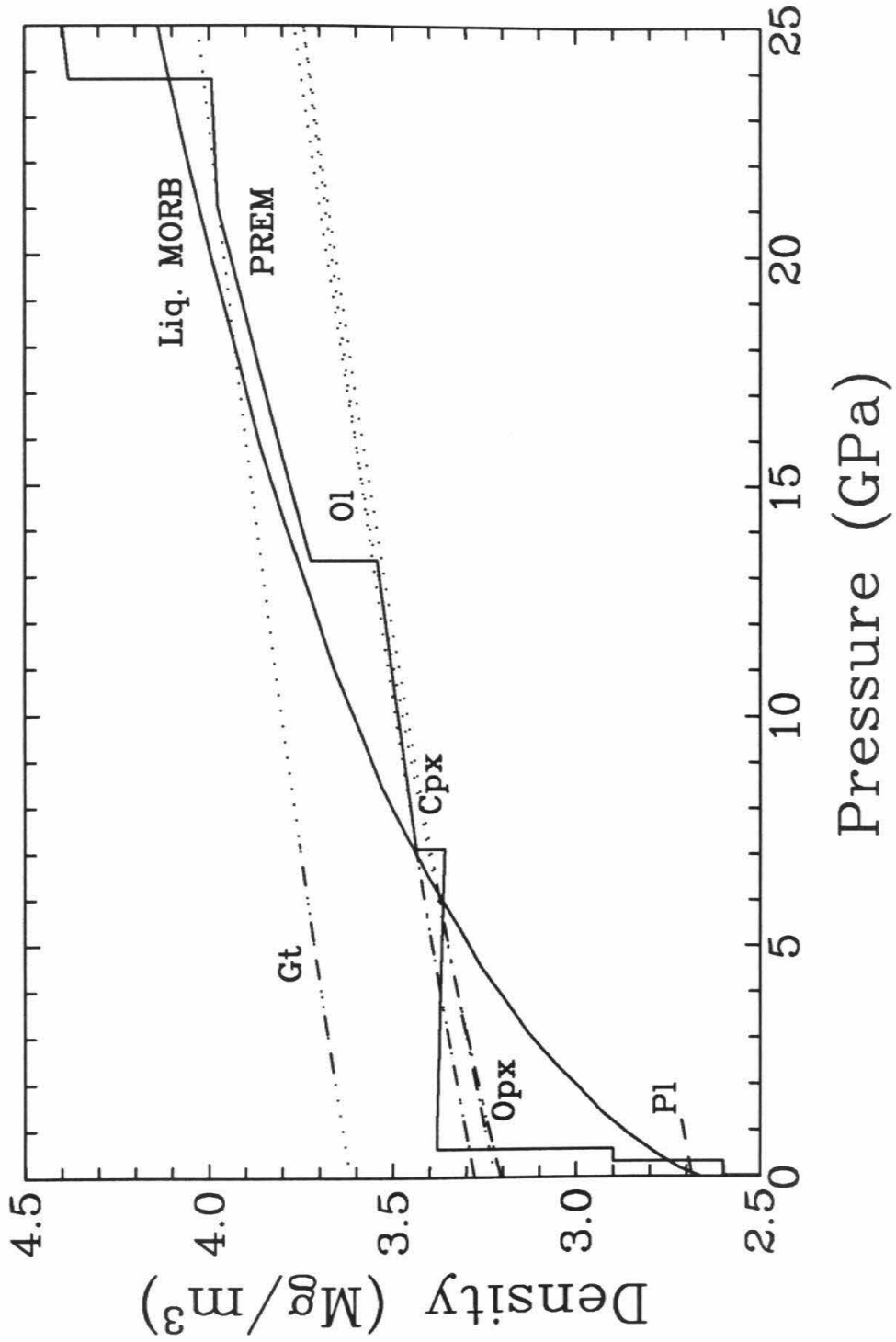
sion at plate boundaries and the density contrast between the partial melt and solid mantle. In general terms, the primary partial melt is produced when a diapir rising adiabatically from the mantle impinges on the more gently sloping solidus of the solid mantle (peridotite) and begins to melt (Figure 1.15). The melting may occur all at once (batch melting) or the diapir may melt as it rises (polybaric melting). In either case, the final composition of the basalt produced at the ridge by shallow fractional crystallization will depend on the depth of the source, the extent of partial melting of the source and the rate of segregation of the melt from its source. These aspects are ultimately dependent on the density differences between the melt and solid residue. The melt fraction required to segregate the melt from its solid residue at the same rate at which it is produced by melting at any given instant in time is inversely proportional to $\Delta\rho$ [*Riley and Kolhstedt,* 1992]. Therefore a larger melt fraction is necessary to segregate the melt from its solid residue when the density contrast is small. *Stolper et al.,* [1981] also showed that segregation rate and melt velocity are directly related to the density contrasts between the liquid and solid. In particular, the melt velocity is proportional to $\Delta\rho$ so for small density contrasts primary melts should rise slower (and therefore might react with the surrounding mantle). Also the time needed to segregate the liquid by percolation is inversely proportional to $\Delta\rho$ so for small density contrasts it takes longer to segregate a primary liquid from its solid residue.

The density contrasts needed for magma flow are ultimately determined by the chemistry of the system. Lherzolite, is the typical source composition used to produce primary MORB magmas. The lherzolites may be divided into three groups

based on the transition of the aluminous phase found in some basalts as a function
of increasing pressure from plagioclase to spinel to garnet. Plagioclase lherzolites to
spinel lherzolites, can produce MORB liquids plus olivine, augite (Cpx), orthopyrox-
ene (Opx) and an aluminous phase (plagioclase or spinel) at shallow depths, 0 to 4
GPa, at 1250 to 1400°C [See table 5 of *Kinzler and Grove,* 1992a for references]. A
garnet lherzolite source for MORB primary magmas require the melts to be derived
from greater depth ($>$ 2.5 GPa) and has been invoked by various workers to get a
garnet phase in equilibrium with the melt [*Bender et al.,* 1984; *Klein and Langmuir,*
1987; *McKenzie and Bickle,* 1988; *Salters and Hart,* 1989].

The composition of the melt and its equilibrium phases will vary as a function of
pressure and temperature so that deeper in the upper mantle the partial melts be-
come richer in MgO, such that the melts range from basalts to picrites to komatiites.
The crystal composition will also become more MgO-rich, such that olivine, in equi-
librium with the melt, ranges from Fo_{84} in MORB to Fo_{94} in komatiites. *Takahashi
and Kushiro* [1983] found that to 4 GPa the olivine changes slightly as a function of
pressure by $K_D = (FeO/MgO)^{ol}/(FeO/MgO)^{liq} = 0.3 + 0.02P$ (GPa). The $K_D^{\frac{xtl.}{liq.}}$
for the other phases will have similar increases as pressure increases from their initial
values.

With these compositional variations in mind, we have chosen a specific set of
equilibrium crystal compositions to compare with our Liquidus MORB from the
experimental data. We have mainly used the results of *Takahashi and Kushiro* [1983]
for the melting of a spinel lherzolite (Salt Lake Crater, Hawaii). At 0.8 GPa, 1200°C
their experiments show that the residual liquid from the lherzolite is basaltic and the

equilibrium crystal phases are olivine (Fo_{84}), orthopyroxene (En_{84}) and clinopyroxene (Di_{82}). The subscript on each of these minerals refers to the mole fraction of MgO in each phase. *Stern et al.* [1975] found garnet to be a liquidus phase for the olivine tholeiite starting at 2 GPa. They did not provide the exact composition of this phase so we have used the experimental study of *Johnston* [1986] on the melting of a high alumina basalt that is very similar in composition to our MORB and also has a similar liquidus. Garnet (Py_{75}) was the liquidus phase for this melt starting at 2.7 GPa and $1450^{o}C$. The initial density of each phase was corrected for its MgO-FeO concentration and initial temperature, using the data in Table 1.11. In addition, the plagioclase (An_{90}) EOS was taken from the float/sink experiments of *Fujii and Kushiro* [1977].

The adjusted EOS for each mineral phase is shown in Figure 1.14. The dashed part of each curve represents the approximate stability region (on the liquidus or near the liquidus) of the phase in equilibrium with the basaltic melt. The density crossover for Fo_{84} with the Liquidus MORB is at the base of the low velocity zone, ~ 7 GPa, which is consistent with the crossover predicted by *Rigden et al.* [1984]. Both pyroxenes, Opx (En_{84}) and Cpx (Di_{82}) cross the Liquidus MORB at lower pressures, ~ 5 GPa. Garnet (Py_{75}) will always sink in a MORB liquid, while it appears that plagioclase (An_{90}) will always float. As a function of increasing pressure, the density contrast decreases to almost 0 for the two pyroxenes and olivine, while the density difference between liquid and garnet is reduced near the LVZ. The density contrast for plagioclase has the opposite effect and increases as pressure increases. Comparing the slope of the Liquidus MORB with the slopes of the crystal phases indicates how

Mineral	ρ_o [gm/cc]	Kos [GPa]	K' []	$\alpha \times 10^{-5}$ [K^{-1}]	$\gamma_o^\star$ []	$x_{Fe}^\star$
Fo	$3.222 + 1.182 x_{Fe}$	129	5.1	2.68	1.15	.10
En	$3.204 + 0.799 x_{Fe}$	104	5.0	2.6	1.1	.30
Di	$3.277 + 0.38 x_{Fe}$	$113 + 7 x_{Fe}$	4.5	2.55	1.1	.20
Py	$3.562 + 0.758 x_{Fe}$	$175 + 1 x_{Fe}$	4.9	2.38	1.1	.25

Data from table 5 of *Duffy & Anderson, 1989*

$^\star\gamma_o$ assumed, except for Fo *Kumazawa & Anderson, 1969*; Opx, Cpx *Watanabe, 1982*

$^\star x_{Fe}$, mole fraction of Fe-phase in each mineral from

Takahashi, 1986; Takahashi & Kushiro, 1983

Johnston, 1986

Table 1.11: EOS parameters and mole fraction of FeO for mineral phases in equilibrium with basaltic liquid at $\sim 1250^o$C and 0.8 GPa.

rapidly the density contrast between solid and liquid changes at a pressure < 4 GPa.

This critical region is the depth range for primary melts and their equilibrium crystal phases as derived from experimental studies of the fusion products of peridotites and chemical analyses of basalts and xenoliths. *Klein and Langmuir* [1987] collected an extensive chemical data set for MORB, which they systematically corrected for shallow fractionation, and then correlated the resulting chemical signature with axial depth and crustal thickness. They concluded that most MORB could be accounted for by 8-20% melting from 0.5-1.6 GPa (15-50 km) and that the extent of partial melting was the only significant parameter consistent with the chemical variation of primary MORB melts. In this manner, the authors eliminated higher pressure Cpx fractionation and source heterogeneity as significant factors controlling chemical variation. This generalized model is consistent with previous models for source magmas that have a shallow source (0.9 - 1.1 GPa, $\sim$27 km) derived from batch melting of a primary composition very close to the most primitive MORB [e.g., *Presnall et al.*, 1979; *Fujii and Scarfe*, 1985; *Fujii*, 1989]. and for primary magmas derived from a polybaric source (0-3 GPa) by the aggregation of small melt fractions (0.1 - 5%) as the parcel rises along an adiabat [e.g., *Kinzler and Grove*, 1992a,b]. These studies are all consistent with our results that indicate the largest density contrast between the MORB liquid and its equilibrium crystal phases between 0.5 - 2.0 GPa, allowing the most efficient segregation and buoyancy for the range of melt fractions proffered by the various petrologic models.

Of course these shallow source models with small to medium extents of partial melting are not the only models used to derive basalts. Picritic primary magmas from

deeper in the mantle have been suggested as the source for basalts [e.g., *O'Hara*, 1968; *Green et al.*, 1979; *Elthon and Scarfe*, 1984; *Stolper*, 1980]. Picrites are intermediate in composition between MORB and komatiite ($\sim$ 20 wt% MgO) and they represent a more controversial source composition because of the large amount of melting and fractionation required to transform them to MORB and the range of pressures over which they have been suggested to be derived from. The pressure range extends from $\sim$ 1 GPa [*Elthon and Scarfe*, 1984] to $\sim$ 3.5 GPa [*O'Hara*, 1968]. The composition of the crystal phases in equilibrium with picrite would be more magnesian than those for basalts. With these small changes in composition it is still true that the smallest density contrast will be near the source depth of the melts (3 - 5 GPa). *Klein and Langmuir*, 1987] noted that magmas derived by larger fractions of melting indicated a deeper segregation depth. The results of our EOS study of MORB are consistent with this observation and indicate that the derivation of basaltic melts from pressures greater than 2 GPa will require greater melt fractions because the density contrast between the melt and solid residue is decreasing dramatically as the base of the LVZ is approached. This is consistent with the dependence of the melt velocity and segregation efficiency on the density contrast and suggests that mafic melts cannot separate for small melt fractions (i.e., polybaric melting) at high pressures ($>$ 2 GPa). Thus if MORB is derived from a picritic source at high pressures there must be extensive partial melting in order to allow the melt to buoyantly rise to the near surface.

These considerations are consistent with the petrological observations that primary MORB magmas come from a pressure range of 0.9 to 3 GPa because this is

where the density contrast of the MORB versus a solid residue would be the greatest and thus segregation would be most efficient in this depth range, does not require a large amount of partial melt and does not allow significant compositional changes. Although the large density contrast allows for the possibility of small melt fraction segregation it does not preclude the occurrence of large melt fractions. The size of the melt fraction becomes more critically dependent on $\Delta\rho$ at high pressure where the small density difference will not allow efficient segregation without a large melt fraction.

Figure 1.15: Phase relations basalt and peridotite versus possible adiabats (thin lines) and the high and low temperature oceanic geotherms (dash-dot curves) [*Mercier and Carter,* 1975]. The peridotite phase relations are taken from *Takahashi* [1986] for the melting of a dry, fertile spinel lherzolite. The lherzolite solidus is the heavy solid curve, while the light, dotted curves indicate the boundary where the crystal phase (label on each line) is completely melted. The basaltic liquidus (heavy dashed line labeled BL) is from *Stern et al.* [1975] for an olivine tholeiite.
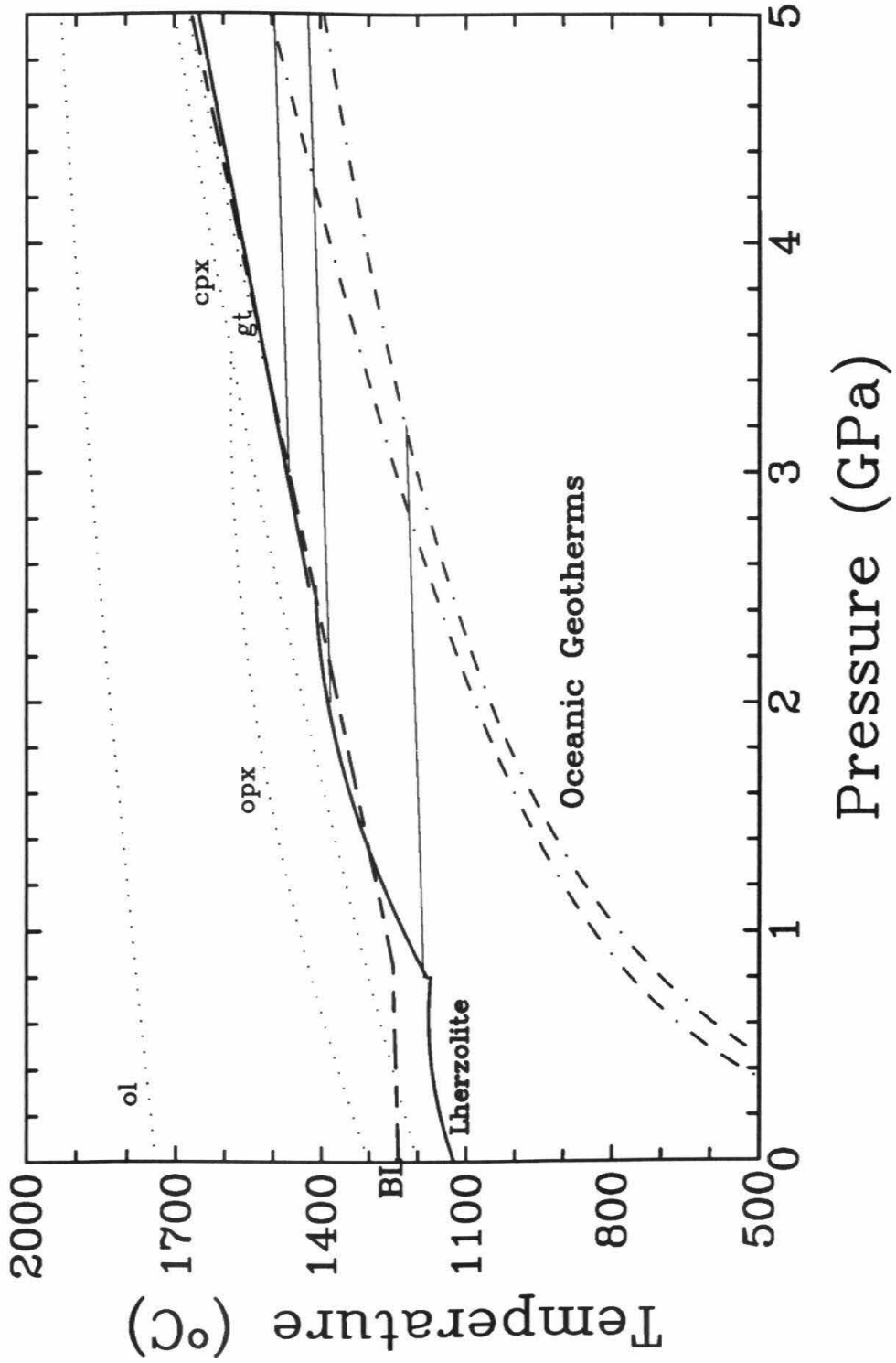
Bibliography

Agee, C. B., Isothermal compression of molten Fe2SiO4, *Geophys. Res. Let.,19*, 1169-1172, 1992.

Agee, C. B., and D. Walker, Mass balance and phase density constraints on early differentiation of chondritic mantle, *Earth Planet. Sci. Lett.*, *90*, 144 - 156, 1988.

Ahrens, T. J., J. H. Lower, and P. L. Lagus, Equation of state of forsterite, *J. Geophys. Res.*, *76*, 514-528, 1971.

Altshuler, L. V., Use of shock waves in high-pressure physics, *Soviet Physics US-PEKHI*, *8*, 52-91, 1965.

Anderson, O. L., R. C. Schreiber, R. C. Leibermann, and N. Soga, Some elastic constant data on minerals relevant to geophysics, *Rev. Geophys.*, *6*, 491-524, 1968.

Bender, J. F., C. H. Langmuir, and G. N. Hanson, Petrogenesis of basalt glasses from the Tamayo region, East Pacific Rise, *J. Petrol.*, *25*, 213-254, 1984.

Birch, F., Finite strain isotherm and velocities for single-crystal and polycrystalline NaCl at high pressures and 300 K, *J. Geophys. Res.*, *83*, 1257-1268, 1978.

Bland, D. R., On shock structure in a solid, *J. Inst. Math Appl.*, *1*,56-75, 1965.

Bottinga, Y., and D. F. Weill, Densities of liquid silicate systems calculated from partial molar volumes of oxide components, *Amer. J. Sci.*, *269*, 169 - 182, 1970.

Bottinga, Y., and D. F. Weill, The viscosity of magmatic silicate liquids: A model for calculation, *Am. J. Sci.*, *272*, 438-475, 1972.

Bottinga, Y., D. F. Weill, and P. Richet, Density calculations for silicate liquids, I, Revised method for aluminosilicate compositions, *Geochim. Cosmochim. Acta*, *46*, 909-919, 1982.

Bottinga, Y., P. Richet, and D. F. Weill, Calculation of the density and thermal expansion coefficient of silicate liquids, *Bull. Mineral.*, *106*, 129-138, 1983.

Delaney, J. R., H. P. Johnson, and J. L. Karsten, The Juan de Fuca Ridge - Hot-Spot - propagating rift system: New tectonic, geochemical, and magnetic data, *J. Geophys. Res.*, *86*, 11,747 - 11750, 1981.

Dingwell, D. B., and S. L. Webb, Structural relaxation in silicate melts and non-Newtonian melt rheology in geologic processes, *Phys. Chem. Minerals*, *16*, 508-516, 1989.

Duffy, T. S., Elastic properties of metals and minerals under shock compression,Ph. D. thesis, 298pp. California Institute of Technology, 1992.

Duffy, T. S., and D. L. Anderson, Seismic velocities in mantle minerals and the mineralogy of the upper mantle, *J. Geophys. Res.*, *94*, 1895-1912, 1989.

Duvall, G. F., and G. R. Fowles, Shock waves, in *High Pressure Physics and Chemistry*, edited by R. S. Bradley, pp. 209-291, Academic Press, N.Y., 1963.

Dziewonski, A. M., and D. L. Anderson, Preliminary reference Earth model, *Phys. Earth Planet. Int.*, *25*, 297-356, 1981.

Elthon, D., and C. M. Scarfe, High-pressure phase equilibria of a high-magnesia basalt and the genesis of primary oceanic basalts, *Am. Mineral.*, *69*, 1-15, 1984.

Fujii, T., Genesis of mid-ocean ridge basalts, in *Magmatism in the Ocean Basins*, vol. 42, edited by A. D. Sounders and M. J. Norry, pp. 71-105, Geol. Soc. Spec. Publ., London, 1989.

Fujii, T., and I. Kushiro, Density, viscosity, and compression of basaltic liquid at high pressures, *Year Book Carnegie Inst., Washington*, *76*, 419-4 24, 1977.

Fujii, T., I. Kushiro, and K. Hamuro, Melting relations and viscosity of an abyssal olivine tholeiite, *Initial Reports of the Deep Sea Drilling Project*, *45*, 513-517, 1978.

Fujii, T., and C. M. Scarfe, Composition of liquids coexisting with spinel lherzolite at 10 kbar and the genesis of MORBs, *Contrib. Mineral. Petrol.*, *90*, 18-28, 1985.

Green, D. H., and A. E. Ringwood, The genesis of basaltic magmas, *Contrib. Mineral. Petrol.*, *15*, 103-190, 1967.

Green, D. H., W. O. Hibberson, and A. L. Jacques, Petrogenesis of mid-ocean basalts, in *The Earth: Its Origin, Structure, and Evolution*, edited by M. W. McElhinney, pp. 265-299, Academic Press, London, 1979.

Jeanloz, R., Finite-strain equation of state for high-pressure phases, *Geophys. Res. Lett.*, *8*, [12], 1219 - 1222, 1981.

Jeanloz, R., Effects of phase transitions and possible compositional changes on the seismological structure near 650 km depth, *Geophys. Res. Lett.*, *18*, 1743 - 1746, 1991.

Jeanloz, R., and T. J. Ahrens, Release adiabat measurements on minerals: The effect of viscosity, *J. Geophys. Res.*, *84*, 7545-7548, 1979.

Jeanloz, R., and T. J. Ahrens, Equations of state of FeO and CaO, *Geophys. J. Roy. Astr. Soc.*, *62*, 505-528, 1980.

Jeanloz, R., and R. Grover, Birch-murnaghan and Us - up equations of state, in *APS 1987 Topical Conference of Shock Waves in Condensed Matter*, edited by S. C. Schmidt and N. C. Holmes, Monterey, CA, 1987.

Jeanloz, R., and Y. Sato-Sorenson, Hydrostatic compression of $Fe_{1-x}O$ wustite, *J. Geophys. Res.*, *91*, 4665-4672, 1986.

Jeanloz, R., and A. B. Thompson, Phase transitions and mantle discontinuities, *Rev. Geophys. Space Phys.*, *21*, [No. 1], 51 - 74, 1983.

Johnston, A. D., Anhydrous P-T phase relations of near-primary high-alumina basalt from the South Sandwich Islands, *Contrib. Mineral. Petrol.*, *92*, 368-382, 1986.

Kinzler, R. J., and T. L. Grove, Primary magmas of mid-ocean ridge basalts 1. Experiments and methods, *J. Geophys. Res.*, *97*, 6885-6906, 1992a.

Kinzler, R. J., and T. L. Grove, Primary magmas of mid-ocean ridge basalts 2. Applications, *J. Geophys. Res.*, *97*, 6907-6926, 1992b.

Klein, E. M., and C. H. Langmuir, Global correlations of ocean ridge basalt chemistry with axial depth and crustal thickness, *J. Geophys. Res.*, *92*, 8089-8115, 1987.

Kress, V. C., and I. S. E. Carmichael, The compressibility of silicate liquids containing Fe_2O_3 and the effect of composition, temperature, oxygen fugacity and pressure on their redox states, *Contrib. Mineral. Petrol.*, *108*, 82-92, 1991.

Kress, V. C., Q. Williams, and I. S. E. Carmichael, When is a silicate melt not a liquid?, *Geochim. Cosmochim. Acta*, *53*, 1687-1692, 1989.

Kumazawa, M., and O. L. Anderson, Elastic moduli, pressure derivatives, and temperature derivatives of single-crystal olivine and single-crystal forsterite, *J. Geophys. Res.*, *74*, 5961-5972, 1969.

Kuno, H., Geology and petrology of Omuro-yama volcano group, north Izu, *J. Fac. Sci. Univ. Tokyo, Sec. II*, *9*, 241-265, 1954.

Kushiro, I., Density of tholeiite and alkali basalt magmas at high pressures, *Year Book Carnegie Inst., Washington*, *80*, 305-309, 1981.

Kushiro, I., J. H. S. Yoder, and B. O. Mysen, Viscosities of basalt and andesite melts at high pressure, *J. Geophys. Res.*, *81*, 6351-6356, 1976.

Lange, R. A., and I. S. E. Carmichael, Denisities of Na2O-K2O-CaO-MgO-FeO-Fe2O3-Al2O3-TiO2-SiO2 liquids: New measurements and derived partial molar properties, *Geochim. Cosmochim. Acta*, *51*, 2931 - 2946, 1987.

Lange, R. A., and I. S. E. Carmichael, Ferric-ferrous equilibria in Na2O-FeO-Fe2O3-SiO2 melts: Effects of analytical techniques on derived partial molar volumes, *Geochim. Cosmochim. Acta*, *53*, 2195 - 2204, 1989.

Lange, R. A., and I. S. E. Carmichael, Thermodynamic properties of silicate liquids with emphasis on density, thermal expansion and compressibility, in *Modern Methods of Igneous Petrology, Reviews in Mineralogy*, vol. 24, edited by J. Nicholls, pp. 25 - 106, Mineralogical Society of America, 1990.

Lyzenga, G. A., T. J. Ahrens, and A. C. Mitchell, Shock temperatures of SiO2 and their geophysical implications, *J. Geophys. Res.*, *88*, 2431-2444, 1982.

Manghnani, M. H., H. Sato, and C. S. Rai, Ultrasonic velocity and attenuation measurements on basalt melts to 1500C: Role of composition and structure in the viscoelastic properties, *J. Geophys. Res.*, *91*, 9333-9342, 1986.

Marsh, S. P., *LASL Shock Hugoniot Data*, University of California Press, Berkeley, 1-658, 1980.

McKenzie, D., and M. J. Bickle, The volume and composition of melt generated by extension of the lithosphere, *J. Petrol.*, *29*, 625-679, 1988.

McQueen, R. G., S. P. Marsh, J. W. Taylor, J. N. Fritz, and W. J. Carter, The equation of state of solids from shock wave studies, in *High-Velocity Impact Phenomena*, edited by R. Kinslow, pp. 294-417, Academic Press, New York, 1970.

Melosh, H. J., *Impact Cratering, A Geologic Process*, Oxford University Press, New York, 1-245, 1989.

Mercier, J., and N. L. Carter, Pyroxene geotherms, *J. Geophys. Res.*, *80*, 3349-3362, 1975.

Miller, G. H., The equation of state and petrogenesis of komatiite, Ph. D. thesis, 300pp. California Institute of Technology, 1990.

Miller, G., E. M. Stolper, and T. J. Ahrens, The equation of state of a molten komatiite I: Shock wave compression to 36 GPa, *J. Geophys. Res.*, *96*, 1831-1848, 1991a.

Miller, G., E. M. Stolper, and T. J. Ahrens, The equation of state of a molten komatiite II: Application to komatiite petrogenesis and the hadean mantle, *J. Geophys. Res.*, *96*, 1849-1864, 1991b.

Murase, T., Density and compressional wave velocity of basaltic and andesitic liquids, *Year Book Carnegie Inst. Washnigton, 80*, 303-306, 1981.

Murase, T., I. Kushiro, and T. Fujii, Compressional wave velocity of partially molten peridotite, *Year Book Carnegie Inst. Washnigton*, *76*, 414-416, 1977.

Murase, T., and A. E. McBirney, Properties of some common igneous rocks and their melts at high temperatures, *Geol. Soc. Am. Bull.*, *84*, 3563-3592, 1973.

O'Hara, M. J., Are any ocean basalts primary magma?, *Nature*, *220*, 68 3-686, 1968.

Peselnick, L., R. Meister, and W. H. Wilson, Pressure derivatives of elastic moduli of fused quartz to 10 kb, *J. Phys. Chem. Solids*, *28*, 635-639, 1967.

Presnall, D. C., J. R. Dixon, T. H. O'Donnell, and S. A. Dixon, Generation of mid-ocean ridge tholeiites, *J. Petrol.*, *20*, 3-35, 1979.

Press, W. H., B. P. Flannery, S. A. Teukolsky, and W. T. Vetterling, *Numerical Recipes in C The Art of Scientific Computing*, Cambridge University Press, Cambridge, 1-735, 1988.

Rai, C. S., K. W. Katahara, and M. H. Manghnani, Viscoelastic behavior of two ba salt melts (abs.), *EOS Trans. AGU*, *63*, 469, 1982.

Rai, C. S., M. H. Manghnani, and K. W. Katahara, Ultrasonic studies on a basalt melt, *Geophys. Res. Let.*, *8*, 1215-1218, 1981.

Rhodes, J. M., C. Morgan, and R. A. Liias, Geochemistry of axial seamount lavas: Magmatic relationship between the Cobb Hotspot and the Juan de Fuca Ridge, *J. Geophys. Res.*, *95*, [B8], 12,713 - 12,733, 1990.

Rigden, S. M., The determination of the equation of state of molten silicates at high pressures using shock-wave techniques, Ph. D. thesis, 137pp. California Institute of Technology, 1986.

Rigden, S. M., T. J. Ahrens, and E. M. Stolper, Densities of liquid silicates at high pressures, *Science*, *226*, 1071-1074, 1984.

Rigden, S. M., T. J. Ahrens, and E. M. Stolper, Shock Compression of Molten Silicate: Results for a Model Basaltic Composition, *J. Geophys. Res.*, *93*, [B1], 367-382, 1988.

Rigden, S. M., T. J. Ahrens, and E. M. Stolper, High-pressure equation of state of molten anorthite and diopside, *J. Geophys. Res.*, *94*, 9508-9522, 1989.

Riley, G. N., and D. L. Kohlstedt, Melt migration in silicate melt-olivine systems, *Earth Planet. Sci. Let.*, *17*, 2101-2104, 1992.

Rivers, M. L., and I. S. E. Carmichael, Ultrasonic Studies of Silicate Melts, *J. Geophys. Res.*, *92*, [B9], 9247 - 9270, 1987.

Robie, R. A., B. S. Hemingway, and J. S. Fisher, Thermodynamic Properties of Minerals and Related Substances at 298.15 K and 1 Bar (105 Pascals) Pressure and at Higher Temperatures, *U. S. Geol. Surv. Bull.*, *1452*, 163,201,217, 1978.

Ruoff, A. L., Linear shock-velocity–particle-velocity relationship, *J. Appl. Phys.*, *38*, [13], 4976 - 4980, 1967.

Ryan, M. P., Elasticity and contractancy of Hawaiian olivine tholeiite and its role in the stability and structural evolution of subcaldera magma reservoirs and rift systems, *U. S. Geol. Surv. Prof. Pap. 1350*, 1395-1447, 1987.

Salters, V. J. M., and S. R. Hart, The Hf-paradox and the role of garnet in the source of mid-ocean ridge basalts, *Nature*, *342*, 420-422, 1989.

Scott, D. R., and D. J. Stevenson, The competition between percolation and circulation in a deformable porous medium, *J. Geophys. Res.*, *93*, 6451-6462, 1988.

Secco, R. A., M. H. Manghnani, and T. C. Liu, The bulk modulus - attenuation - viscosity systematics of diopside-anorthite melts, *Geophys. Res. Let.*, *18*, [1], 93-96, 1991.

Secco, R. A., M. H. Manghnani, and T. C. Liu, Velocities and compressibilities of komatiitic melts, *Geophys. Res. Let.*, *19*, 93-96, 1991.

Sharpe, M. R., T. N. Irvine, B. O. Mysen, and R. M. Hazen, Density and viscosity of melts of Bushveld chilled margin rocks, *Carneigie Inst. Yearbook*, *82*, 300-304, 1983.

Stebbins, J. F., I. S. E. Carmichael, and L. K. Moret, Heat capacities and entropies of silicate liquids and glasses, *Contrib. Mineral. Petrol.*, *86*, 131 - 148, 1984.

Stern, C. R., W. Huang, and P. J. Wyllie, Basalt-Andesite-Rhyolite-H2O: Crystallization intervals with excess H2O and H2O-undersaturated liquidus surfaces to 35kilobars, with implications for magma genesis, *Earth Planet. Sci. Let.*, *28*, 189-196, 1975.

Stolper, E. M., and D. Walker, Melt density and the average composition of basalt, *Contrib. Mineral. Petrol.*, *74*, 7-12, 1980.

Stolper, E. M., D. Walker, B. H. Hager, and J. F. Hayes, Melt segregation from partially molten source regions: The importance of melt density and source region size, *J. Geophys. Res.*, *86*, 6261-6271, 1981.

Swegle, J. W., and D. E. Grady, Shock viscosity and the prediction of shock rise times, *J. Appl. Phys.*, *58*, 692-701, 1985.

Takahashi, E., Melting of a dry peridotite KLB-1 up to 14 GPa: Implications of the origin of peridotitic upper mantle, *J. Geophys. Res.*, *91*, 9367-9382, 1986.

Takahashi, E., Speculations on the Archean mantle: Missing link between komatiite and depleted garnet peridotite, *J. Geophys. Res.*, *95*, 15,941-15,954, 1990.

Takahashi, E., and I. Kushiro, Melting of a dry peridotite at high pressures and basalt magma genesis, *Am. Mineral.*, *68*, 859-879, 1983.

Touloukian, Y. S., R. K. Kirby, R. E. Taylor, and P. D. Desai, *Thermal expansion of metallic elements and alloys*, Plenum, New York, 1-208-218, 1970.

Walker, D., and C. Agee, Partitioning "equilibrium", temperature gradients, and constraints on Earth differentiation, *Earth Planet. Sci. Lett.*, *96*, 49 - 60, 1989.

Walker, D., C. B. Agee, and Y. X. Zhang, Fusion Curve Slope and Crystal Liquid Buoyancy, *J. Geophys. Res.*, *93*, [B1], 313-323, 1988.

Walsh, J. M., and R. H. Christian, Equation of State of Metals from Shock Wave Measurements, *Phys. Rev.*, *97*, [6], 1544 - 1556, 1955.

Watanabe, H., Thermochemical properties of synthetic high-pressure compounds relevant to the Earth's mantle, in *High-Pressure Research in Geophysics*, edited by S. Akimoto and M. H. Manghnani, p. 441, Center for Academic Publishing, Tokyo, 1982.

Weidner, D. J., J. D. Bass, A. E. Ringwood, and W. Sinclair, The single-crystal elastic moduli of stishovite, *J. Geophys. Res.*, *87*, 4740-4746, 1982.

Weidner, D. J., H. Wang, and J. Ito, Elasticity of ortho-enstatite, *Phys. Earth Planet. Inter.*, *17*, P7-P13, 1978.

Chapter 2

Impact-Induced Metal-Silicate Interactions

Observations of molten mid-ocean ridge basalt (MORB) – molybdenum (Mo) interactions produced by shock experiments provide insight into planetary impact and differentiation processes involving metal-silicate partitioning. Scanning electron microscope (SEM) imaging and chemical analysis of fragments recovered from experiments (achieving MORB liquid shock pressures in the range of 0.8 to 6 GPa) showed significant changes in the composition of the MORB and Mo due to reaction of the silicate and metal liquids on a short time scale (< 13 s). The FeO concentration of the shocked basaltic liquid decreases with increasing shock pressure, from an initial concentration of 9 wt% to 0.1 wt% in the highly shocked (6 GPa) MORB liquid.

Fragments recovered from the intermediate pressure shot (2.8 GPa) contain metallic spheres composed of Fe, Mo and Si, within the shocked glass. The spheres, which have a maximum diameter of ~ 20 μm, range from homogeneous to two texturally

distinct alloys (one enriched in Fe and the other enriched in Mo) with cellular to globular textures. These metallic spheres were derived from the shock-induced dissemination, mixing and reduction of the target in the following manner. Hot ($\sim$1400 - 1700°C) micron-size particles of Mo from the sample holder were injected into the liquid MORB upon fragmentation of the target after impact. The FeO and SiO_2 in the MORB was reduced in an estimated oxygen fugacity of 10^{-17} bars and mixed with the Mo particles. Addition of Fe and Si to the Mo particles decreased the melting point from $\sim$2630°C (pure Mo) to $<$ 1400°C giving rise to the ubiquitous occurrence of metallic spheres in the shocked glass. The cooling rate for the spheres was limited by the cooling rate for the entire fragment since the spheres were insulated by the silicate liquid. The calculated radiative cooling rate for the fragment is $\leq$ 140°C/s, which is slow enough to allow the metal phases within the spheres to coalesce and form the observed globular textures, but fast enough to quench phases before equilibrium could be achieved. The disequilibrium textures, which show the efficient separation of immiscible molten metals from silicate liquids, are similar to those observed in naturally-shocked metallic particles found in meteorites and lunar rocks. Our textures and estimated cooling rates are consistent with the interpretation that globular textures seen in metallic spheroids from lunar samples are due to slow cooling where the spheres are surrounded by the melted target.

The substantial drop in oxygen fugacity ($\sim$8 log units at 1400°C) estimated from the occurrence of iron silicides within the SiO_2 -rich shocked glass is very rare in natural samples and is most analogous to fulgurites (fused products of lightning strikes). The in-situ reduction of FeO in the shocked molten basalt implies that

shock-induced reduction of the impact melt should be considered a viable mechanism for the formation of metallic phases. In particular, the minute, separate Fe particles found in lunar soils may have formed by such a process. Furthermore the partitioning of Fe suggests the increased siderophile character of Fe with increasing temperature and pressure and decreasing oxygen fugacity. If the earth's core formed in a magma ocean produced from a giant impact then impact-induced dissemination, melting and disequilibrium mixing of metal and silicate as observed in this study should be considered when deriving siderophile partitioning characteristics (i.e., partition coefficients).

2.1 Introduction

Observations of the physics and chemistry of impact-induced liquid metal-liquid silicate interactions provide insight into models of the evolution of terrestrial planets via accretional impacts. By studying the physical and chemical processes that allow rapid segregation of metal and silicate in experimental impacts we may gain insight into these same processes in natural impacts. On a small scale, this may allow us to understand the origin of metallic particles found in lunar rocks and meteorites. On a larger scale, such observations may provide more details on how a giant impact model for the evolution of the earth-moon system, accompanied by the development of a magma ocean and efficient core formation, can explain the excess siderophile abundance anomaly in the earth and moon.

Metallic particles are commonly found in lunar rocks and soils [*Wanke et al.,* 1970; *Goldstein et al.,* 1970; *Scarlett et al.,* 1974], meteoritic material [*Blau et al.,*

1973] and in chondrites [*Bunch and Cassidy*, 1968; *Begemann and Wlotzka*, 1969; *Taylor and Heymann*, 1971; *Scott* 1982]. Metallic particles are particularly interesting because the relatively simple metal phase equilibria provides clues to the thermal history of the host silicate phases [*Mehta and Goldstein*, 1980]. If these particles were derived from an impact, then their observed textures and compositions should provide information about the amount of fractionation, partitioning and/or mixing between the planetary surface and the bolide. A limited number of experimental studies have been conducted to duplicate the textures and chemistry of these metallic particles by simulating impact processes [*Blau and Goldstein*, 1975; *Deamer and Goldstein*, 1980; *Badjukov and Petrova*, 1991] while other shock wave studies have noted that partial fragmentation of the sample holder caused injection of metallic particles into the shock-melted sample [*Deamer and Goldstein*, 1980; *Gibbons et al.*, 1975; *Reimold and Stöffler*, 1968; *Schaal et al.*, 1979; *Schaal and Hörz*, 1980; *Schaal*, 1982].

Impact-induced metal-silicate partitioning provides insight into giant impact models of the evolution of the earth-moon system. *Hartmann and Davis* [1975] and *Cameron and Ward* [1976] first suggested a giant impact origin for the moon and such models have increasingly been applied to other terrestrial planets, particularly the earth. A large impact on the proto-earth [*Melosh*, 1989; *Tonks and Melosh*, 1991] would have dramatic effects, including the production of a magma ocean and the efficient and rapid formation of an Fe-rich metallic core. In principle, siderophile partition coefficients can be used to constrain models for the origin of the earth-moon system due to their sensitivity to metal-silicate fractionations [*Newsom and Simms*,

1991; *O'Neill,* 1991a, 1991b]. There is currently no experimental data at the appropriate physical conditions nor is there enough information about the temperature and pressure-dependence of these partition coefficients to attempt an accurate extrapolation to magma ocean conditions. All the experimental work has been done at lower temperatures and pressures, under static conditions, excluding the initial enhanced kinetics and disequilibrium caused by a large impact. *Ringwood and Hibberson* [1991] noted that compositional and thermal gradients are likely to be produced by a giant impact on the earth and are not immediately dissipated. A subtle point about the equilibrium condition noted by *Stevenson* [1990] and reiterated by *Ringwood and Hibberson* [1991] is that equilibrium does not have to occur between the bulk core and bulk mantle. It is probably more likely that equilibrium occurred in local domains between the local liquid composition and metal particles as the core formed. These effects could have important consequences for the chemical models that assume bulk equilibrium, isothermal conditions and static rates of reactions.

2.2 Method

We used the shock wave techniques of *Rigden et al.* [1988] and *Miller et al.* [1991] for molten silicates, so only a brief description is provided here. The target consisted of a ~3 mm thick by 10 mm diameter disk of basaltic glass encapsulated in a vacuum-welded Mo container. This target was hung in a vacuum tank associated with a 40 mm bore propellant gun. The tank was evacuated to $< 100\mu$m Hg (< 0.1 torr) and the target was heated by induction to ~1400^oC to melt the glass. The target was maintained at 1400 ± 5^oC for between ~2 to 5 minutes before it was impacted by a

flyer (either Al or lexan) that produced a shock wave in the target (Figure 1.2).

The experiments were designed to determine the equation of state (EOS) of molten basalt and three parameters were measured during the experiment, the initial pre-heat temperature, the projectile velocity and the shock transit time (STT). The temperature and projectile velocity were measured before impact while the STT recorded the passage of the first shock wave through the liquid basalt and Mo cap (total thickness ~4 mm). For the experiments discussed here, the STT averaged < 1.3 μs. Recognizable, macroscopic (typically $2 \times 1 \times 0.2$ cm) fragments of the impacted target were found in the gun tank. Initially, the fragments were recovered from the floor of the gun tank. Later, a simple recovery system was devised to catch the ejected fragments. Four plywood boards and a lexan board ($15 \times 20 \times 2$ cm each) were clamped onto the steel skid plate in the main body of the tank. These boards were aligned with the axis of the gun barrel and the skid plate was moved as close as possible to the target area (~60 cm behind the target, see Figure 1.2). This system allowed retrieval of several fragments without the further comminution that might have occurred if they hit the thick steel wall of the gun tank instead of the softer wood. The recovered fragments consisted of twisted Mo metal with a thin veneer or small patches of basaltic glass on the surface and within some of the cracks in the metal.

Preliminary analysis was conducted on unpolished surfaces of these fragments using a CAMSCAN Series 2 scanning electron microscope (SEM) at a filament current of ~2 A and an operating voltage of 15 KeV. The fragments were gently cleaned with alcohol, carbon coated and mounted on Al stubs with carbon glue. Images

were taken mostly in the back-scattered electron mode because this provided the best contrast in composition while still depicting the topography on the surface. An energy dispersive spectrometer (EDS), held at a working distance of 35 mm was used for the SEM spot analyses which were collected for 10 – 30 s. Measured peaks were converted to oxide concentrations using the Bence-Albee correction procedure [*Bence and Albee*, 1968].

Quantitative analysis was conducted on a JXA 733 Superprobe. Fragments were mounted in epoxy, cut into several cross sections and polished with alumina grit (to 0.3 μm). Back-scattered electron images (BEI) of polished cross sections of the fragments were taken on the SEM prior to analysis on the electron microprobe in order to locate analysis points. The operating conditions of the probe varied depending on whether the analysis was for metal or glass. For the glass, we used a beam current of 20 nA, a collection interval of $<$60 s per oxide, and a relatively defocussed beam diameter of 20 μm to avoid significant alkali loss or migration during analysis. Mineral standards were used for the major oxides and Mo metal for MoO_3 . For the metal phases, we used a beam current of 5 nA, a collection interval of $<$60 s and a focussed beam diameter of $\sim$2 μm. Analyses of the metal phases were conducted after the completion of all the glass analyses to avoid inadvertently damaging the glass. We used Si, Mo, Fe, Pt and Cu metal standards for these elements and mineral standards for the other major elements that are typically found in the basalt and might be present in the metal phases.

2.3 Results

2.3.1 Shock Conditions

Table 1.3 and 1.9 summarize the initial parameters used for the determination of the shock conditions and Table 1.5 summarizes the shock conditions for the three shots described in this study. The range of MORB shock pressures (0.8 to 6 GPa) are only indicative of the peak values experienced by the silicate liquid. Shock temperature determined by the method of *Miller et al.* [1991] for MORB liquid si given in Figure 1.6. The slope of the pressure-temperature curve for MORB liquid is greater than that for Mo, but Mo is shocked to a higher pressure so the two materials actually experience comparable temperatures (Table 1.5). It is important to note that the temperature calculations have large uncertainties. Factors such as reverberations of secondary shock waves in the target before dissemination, the heat of fusion (which is only significant for the solidification of the metal alloys), the collapse of pore spaces and mechanical heating, none of which are considered in the calculation, may increase the temperature of the shocked material. Also, there were undoubtedly significant temperature gradients in the samples which have not been included in our estimate of the temperature. As a first approximation we assume the fragments have an average temperature equal to the peak shock temperatures calculated for the metal ($\sim$1500$\pm$200^{o}C) and liquid silicate ($\sim$1400$\pm$200°C). Assuming that the post-shock temperature is greater than the pre-shock temperature, the temperature range for the sample is 1400 $-$ 1700°C.

Compositional and textural changes as a function of impact conditions were determined from analyses of each of two fragments from three shots (826, with a lexan

flyer, and 760 and 824, both with Al flyers). The fragments recovered from shot# 760 did not employ a wood recovery system. The fragments from the other two shots (826 and 824) were rescued from the plywood boards. Two sections of a fragment from each shot were analyzed. Each segment was numbered in the following way: shot#, fragment# – board#, cross section letter. The fragment# refers to which fragment was recovered. The board# indicates which plywood board the fragment was embedded in. The fragments tended to penetrate further (e.g., into the third or fourth board) as the impact velocity was increased. The cross section letter refers to whether it was the first (a), second (b) etc... segment cut from that fragment. For example, fragment 8261-3a is from shot# 826, the first fragment removed from the third board and the first cross-sectional segment cut from the epoxied fragment.

2.3.2   Textures

Textural features of the recovered fragments provide information about the mechanical and chemical evolution of the different components of the impactor and target after impact. Before discussing the textures observed along the Mo–shocked glass interface as a function of increasing pressure for the three shots (826, 760 and 824) we would like to describe some important textures seen in a fragment recovered from the gun tank floor that was not cut, polished or analyzed in detail. Fragment # 834 has an irregular surface that shows a possible mechanism for Mo comminution and various target materials that may contaminate the Mo-MORB system after impact (Figure 2.1). Instead of the typical smooth texture of an unshocked metal surface the Mo is broken up into polygons along grain boundaries in the metal. The Mo is deformed as a result of shock stress and the subsequent heating resulting from

irreversible deformation. Similar textures have been observed in metallurgy [*Gray et al.*, 1988; *Unal et al.*, 1990], where the polygonization indicates a coalescence of dislocations into low-angle boundaries upon annealing after plastic deformation. The deepening of the intergranular cracks, the increase in their separation and the rounding of the polygon edges may be due to thermally induced self-diffusion, local grain-boundary vaporization or oxidation of the metal surface. The smooth, non-vesicular glass on fragment # 834 (Figure 2.1) forms irregular patches on the surface and oozes through the cracks in the polygonized metal. This textural feature has been described in high pressure and temperature experiments involving Fe-silicate interactions by *Ringwood and Hibberson*, [figure 5, 1991] and *Goarant et al.*, [figure 13, 1992]. They attributed the textures to penetrative flow and grain boundary wetting at low-dihedral angles of the silicate by the molten metal liquid. In our case we have grain boundary wetting of the metal by the silicate liquid, which can occur because of the weakened and separated grain boundaries in the metal due to shock deformation.

There is obvious evidence of other components of the target assembly on the surface of this fragment. The fiber ($\sim$55 μm) is part of the alumina ceramic sheath for the thermocouple. On the large patch of glass on the left side of the photo, the gray bits on the surface are alumina fibers and the bright white spheres are metal alloys, which contain Mo, Si, and Fe; some also contain Pt, Rh and Cu. Pt and Rh are from the thermocouple wire, Cu from the coil used for induction heating and Fe from the host melt. The extra components may mix with the MORB liquid and contaminate the melt composition.
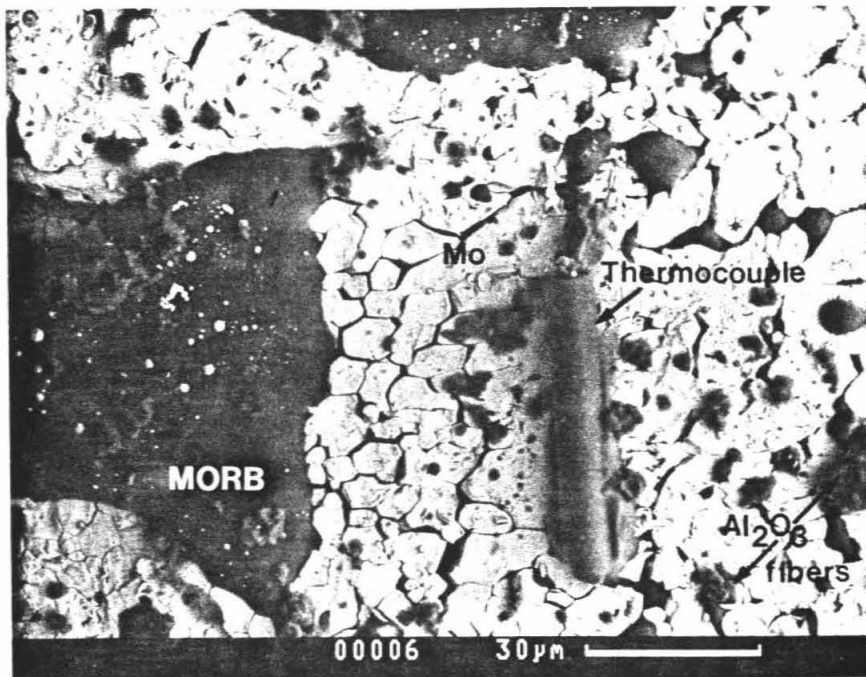
Figure 2.1: Image of the unpolished surface of fragment 834 recovered from a low pressure shot ($P_{MORB} \sim$ 1 GPa). Note the polygons of metal representing grain separations resulting from the stresses induced by impact-produced shock waves. The brightness of the images is proportional to the atomic number of the material. The Mo metal is the brightest feature because it has the highest atomic number (42) of the major elements of interest.

Shot # 826

The shocked glass in the fragments recovered from the lowest pressure shot# 826 (P_{MORB} ~0.8 GPa) had a pahoehoe-like microtexture. The glass is very vesicular with an estimated measurable range of bubble diameters from 10 – 550 μm. Polished cross sections of 8261-3a and b, reveal a vesicular glass with a range of vesicle sizes from 10 – 170 μm diameter. Neither the size nor the amount of vesicularity varied in any systematic way as the interface between glass and Mo is approached. Besides the vesicularity, the glass is relatively smooth and homogeneous in texture and there is a sharply defined interface between it and the Mo, indicating little mixing between the two components.

Shot # 760

Fragments, from shot# 760, recovered in the gun tank, with a peak pressure in the MORB of 2.8 GPa, show substantial metal-silicate interactions. Figure 2.2 shows part of fragment# 7601, which has the largest observed surface area covered by a texturally homogeneous swath of black shocked glass. There are many bright, white spheres on the surface and Figure 2.3 shows a magnified view of the grainy texture of the largest sphere in the center of Figure 2.2. The roughly stippled surface may indicate oxidation or evaporation of the surface of this sphere similar to the results seen by *King* [1983].

Polished cross sections (7601a and 7601c) of this fragment showed mixing along the metal-silicate interface and more details of the textures of the spheres. In Figure 2.4 of 7601a, the interface is irregular and micron-size, rounded polygons of Mo are partially separated from the Mo metal and partially surrounded by an Al-rich
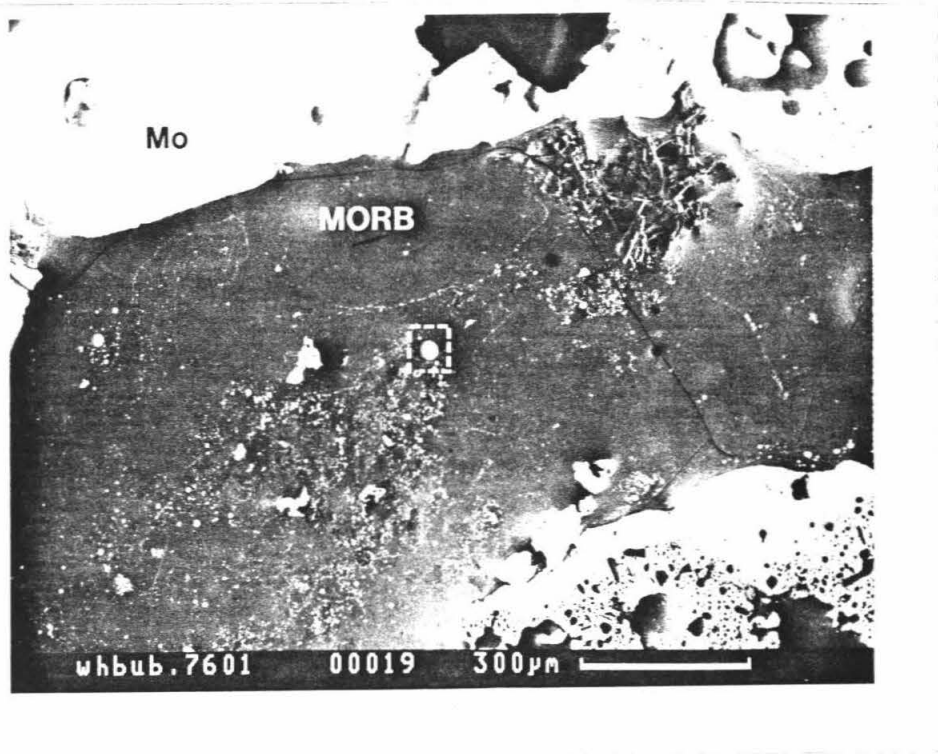
Figure 2.2: Image (BEI) of recovered fragment 7601. Shot #760 reached a P~2.8 GPa and a shock T~1477°C in the MORB. The white spheres on the surface are metal alloys enriched in Fe, Si and Mo. The area enclosed in the box is enlarged in Figure 2.3
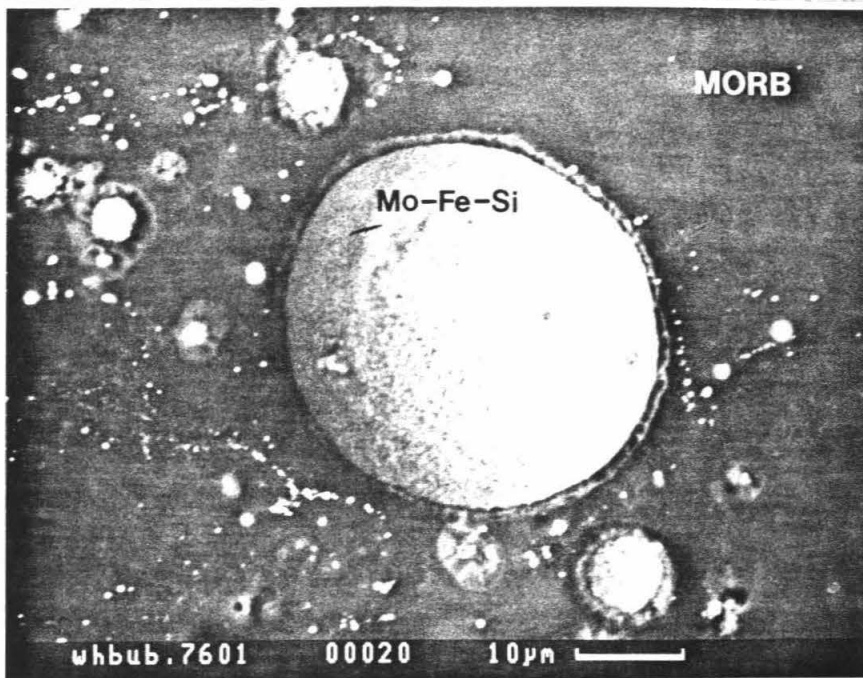
Figure 2.3: Magnified image (BEI) of large sphere in Figure 2.2. The white spheres on the surface are metal alloys enriched in Fe, Si and Mo.

metallic phase and shocked glass. The impact-induced polygonization of the Mo al-
lows a smaller, probably partially melted (as evidenced by the rounded corners) piece
of Mo to react more easily with the surrounding liquid. Further away from the in-
terface (Figure 2.5) the spherical shape of the Mo-rich alloys are textural evidence of
complete melting. The white angular fragment in the large sphere in Figure 2.5 with
the irregular, dendritic interior probably represents a crystal grown during quench.
Many of the larger spheres studied in the shocked liquid are heterogeneous. Magni-
fied images of the three large spheres in Figure 2.6 are shown in Figures 2.7a, b and
c as examples of the cellular to globular textures found within these spheres.

Evidence for turbulent motion of the molten or partially molten spheres in the
shocked liquid is shown in Figure 2.6 and 2.8. Figure 2.6 shows several strings or
streams of variably sized spheres outlining the paths taken by the spheres through
the melt. Many of the paths are relatively straight and the streams of spheres
line up in the same direction. This is seen more clearly in the magnified image in
Figure 2.8, where the streams of metallic spheres traverse the shocked liquid in the
same direction. The motion of the spheres in one direction along parallel lines would
favor an origin related to injection of metallic particles by jetting from the target after
impact. However there is also evidence for some of these streams flowing in semi-
circular paths through the shocked liquid. For example, sphere b in Figure 2.6 is part
of a large, looped string of spheres. Thus, initially the spheres may have been injected
by jetting into the superheated liquid and then some secondary turbulent motion
was initiated in the liquid. Similar textures have been seen in some experiments
and these features have been related to convective processes. *King* [1983] conducted
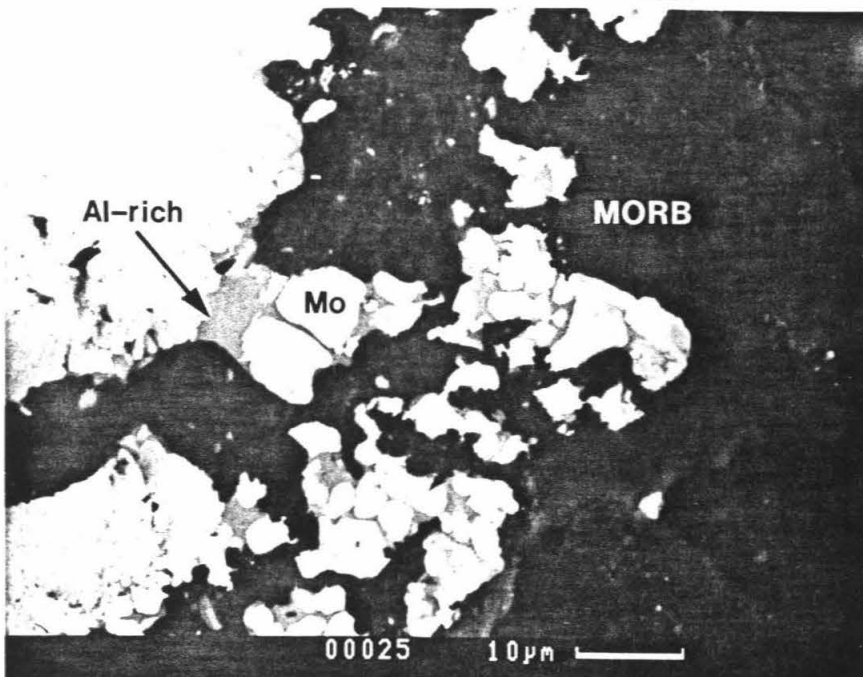
Figure 2.4: Image of cross-sectioned piece (a) of fragment 7601 (see Figure 2.2). The interface is irregular and shows mixing between the Mo and the MORB. The light gray regions surrounding the polygons along the interface are Mo and Al rich (see Table 2.3).
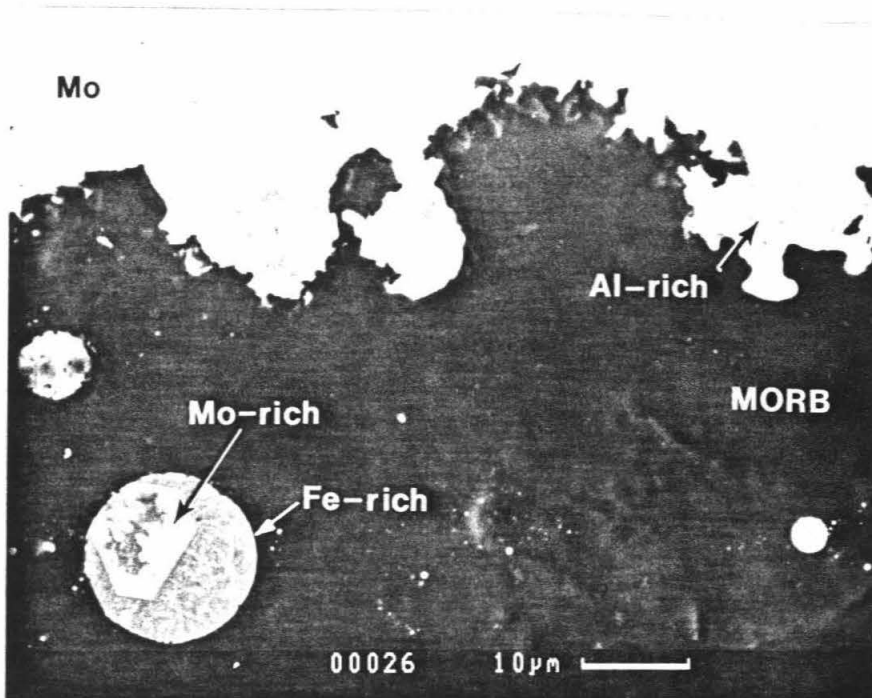
Figure 2.5: Image of cross-sectioned piece (a) of fragment 7601 showing the heterogeneity of the large sphere with the skeletal Mo-rich crystal.

Figure 2.6: Image (BEI) of cross-sectioned piece (c) of fragment 7601 (cut from the fragment shown in Figure 2.2). The spheres labeled a, b and c are shown in magnified images in Figure 2.7. Note the stream of smaller spheres behind the larger spheres, indicating the turbulent movement of the spheres.
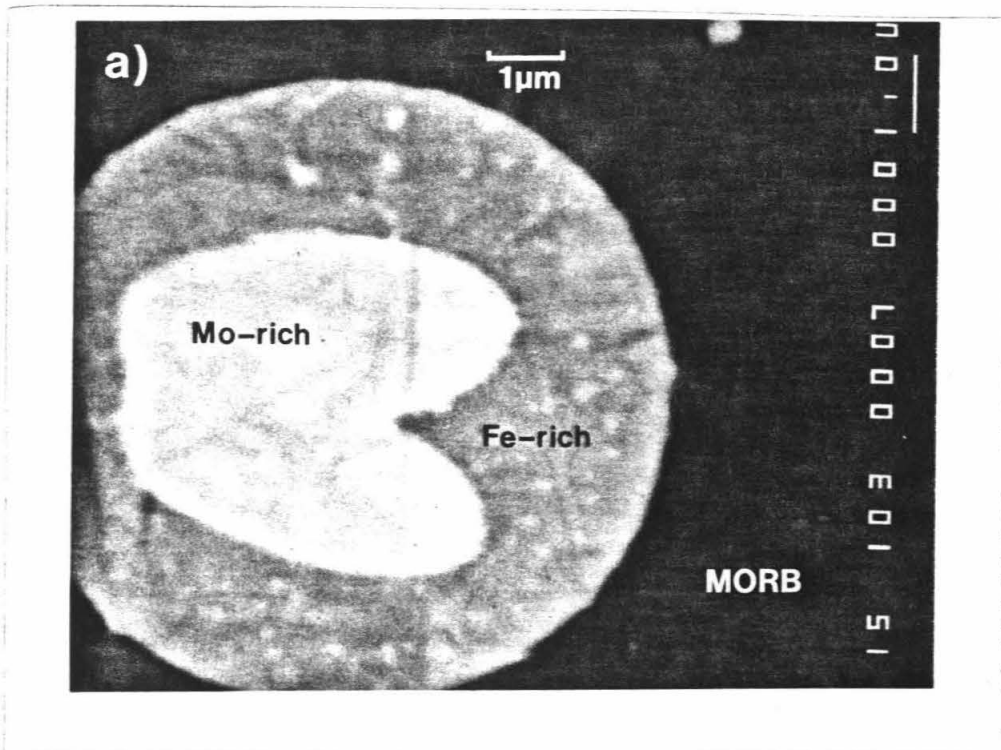
Figure 2.7: a,b and c Magnified image taken on the electron microprobe of the large spheres labeled in Figure 2.6. Separate analyses were done on the white and gray regions (see Table 2.4) of a and b.

b) Mo-rich, Fe-rich, MORB, 1µm

c) Fe-rich, Mo-rich, MORB, 1µm

superheating experiments of basalt standard BCR-1 under vacuum at temperatures between 2400 - 3000°C in which Fe metallic spheres were formed by reduction of FeO. In figure 1a of *King* [1983], the streams of spheres are lined-up along one direction although this directionality is not as distinctive as in the present sample. The author was able to observe the development and movement of these spheres in-situ over a period of several to tens of minutes. He noted convective circulation of the Fe-rich spheres from within the liquid to the surface of the liquid. Once the spheres reached the surface they began to decrease in size due to evaporation. Stringers of metallic spheres are also found in experimentally-shocked lunar regolith analogs contaminated by their stainless steel containers [*Gibbons et al.,* 1975, see figure 8c]. *Gibbons et al.* [1975] indicated that the spheres aligned and concentrated along the highest temperature flow schlieren in the shocked glass. Stringers of metallic spheres occur naturally in basaltic glass fragments from Apollo 11 samples [*Carter and MacGregor,* 1970, see figure 26] and the experimental results may be useful for describing the origin of these spherules and others observed in impact melts.

Shot # 824

The glass on the surface of the fragments retrieved from the wood recovery system for the highest pressure shot# 824 (P_{MORB} ~6 GPa) tended to be extremely vesicular and had many delicate transparent hollow spheres on the surface, indicating degassing. The polished, cross section 8241-4c in Figure 2.9 shows the intense mixing between the Mo and the glass. This figure indicates some of the extreme interactions possible between the glass and Mo ejecta.
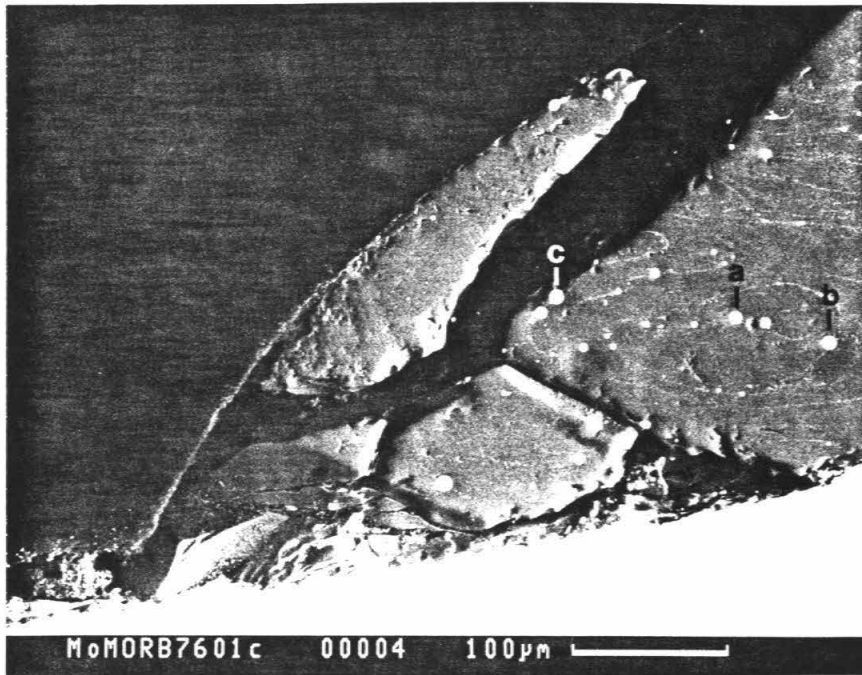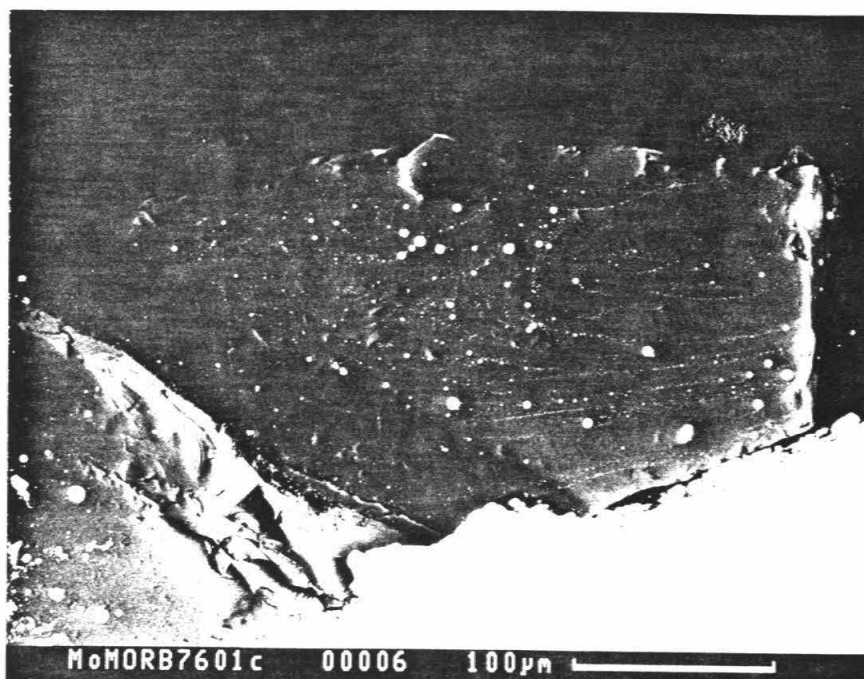
Figure 2.8: Image (BEI) of cross-sectioned piece (c) of fragment 7601 (cut from the fragment shown in Figure 2.2). Note the parallel streams of smaller spheres behind the larger spheres, indicating the movement of the spheres.
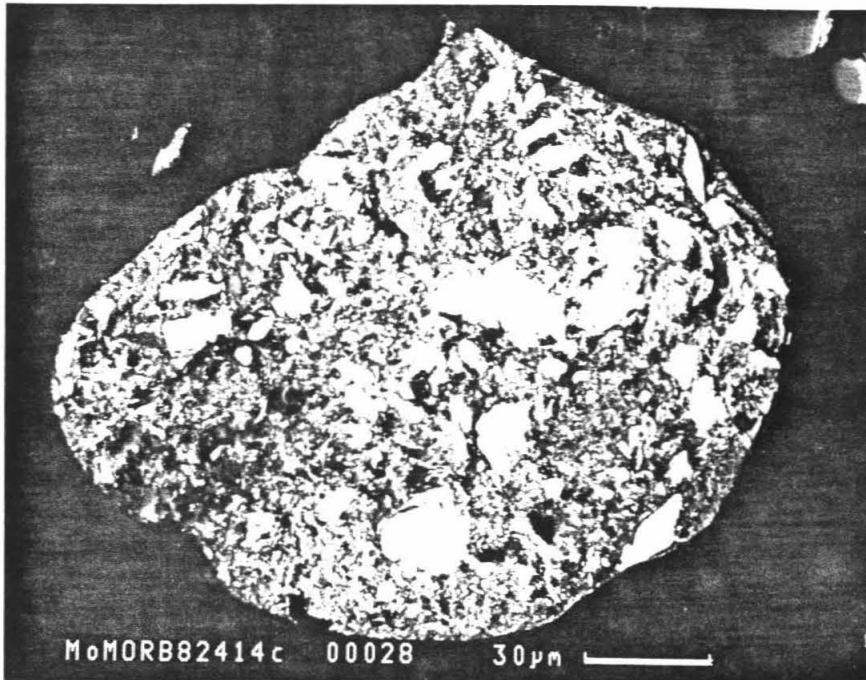
Figure 2.9: High magnification image of an isolated piece of 8241-4c. The gray, slightly vesicular material is shocked glass and the bright white material is Mo. This small region shows the significant deformation and mixing that occurred in the fragments recovered from the highest pressure.

2.3.3   Compositions: Electron Microprobe Results

MORB Glass

The starting material is a mid-ocean ridge basalt (MORB) dredged from the Juan de Fuca Ridge in the Pacific Ocean off the coast of Washington and Oregon (dredge sample # 75-2, see *Delaney et al.,* [1981]). The whole rock sample is crushed to a fine powder and sintered to a homogeneous glass by heating at $\sim1350^{o}C$, well above the MORB liquidus, in a Mo crucible, under reducing conditions ($fO_2 \sim$iron-wüstite) in a gas mixing Deltech furnace for $\sim$12 hours. Microprobe analysis of 73 points on 6 different glass samples yielded small standard deviations ($<$0.2%) indicating that the initial MORB liquid was very homogeneous so shocked liquids from different shots may be compared (Table 2.1). To investigate the possibility that reactions between the MORB and sample holder occurred prior to shock, we duplicated the heating procedure for a shock wave experiment but terminated the run by turning off the power prior to the shot. The resulting MORB glass is essentially identical to the initial composition except for an increase in MoO_3 from 0.1 to 0.3 wt% (Table 2.1). An apparent drop in silica reflects technical difficulties rather than contamination due to the use of one spectrometer for four elements when the pre-heat sample was analyzed. With the exception of some minor MoO_3 contamination, all the chemical changes seen in the fragments occurred during or after impact.

Relative to unshocked MORB, shocked glasses are enriched in SiO_2 and greatly depleted in FeO. The FeO content of recovered glasses decreases systematically with increasing pressure from 9 wt% before shocking to almost none (0.12 wt%) for MORB shocked to $\sim$6 GPa (Figure 2.10). Other changes in the silicate melt chemistry with

| Wt % | Pre-heated | Shocked | | |
		8261-3	7601	8241-4
SiO$_2$	46.82 ± 0.09	61.27 ± 3.27	55.68 ± 1.27	71.18 ± 0.94
TiO$_2$	1.04 ± 0.004	0.45 ± .13	0.60 ± 0.06	0.15 ± 0.04
Al$_2$O$_3$	17.53 ± 0.03	7.92 ± 2.38	19.78 ± 1.16	4.07 ± 1.70
FeO	8.88 ± 0.02	3.86 ± 1.17	1.52 ± 0.19	0.12 ± 0.02
MgO	7.40 ± 0.02	5.54 ± 0.38	5.82 ± 0.21	4.98 ± 0.20
CaO	12.30 ± 0.03	10.77 ± 0.41	10.93 ± 0.41	11.00 ± 0.69
K$_2$O	0.19 ± 0.002	0.05 ± 0.007	0.09 ± 0.003	0.033 ± 0.006
Na$_2$O	2.56 ± 0.01	8.95 ± 1.26	5.28 ± 0.25	7.70 ± 0.74
MnO	0.15 ± 0.003	0.04 ± 0.02	0.12 ± 0.01	0.04 ± 0.02
NiO	—	0.003 ± 0.001	0.01 ± 0.003	0.007 ± 0.003
Cr$_2$O$_3$	—	0.017 ± 0.005	0.02 ± 0.01	0.009 ± 0.004
MoO$_3$	0.28 ± 0.02	0.17 ± 0.06	0.12 ± 0.02	0.26 ± 0.09
TOTAL	97.16 ± 0.14	99.08 ± 0.09	99.95 ± 0.16	99.56 ± 0.27
Points	20	11	35	9

Table 2.1: Results of electron microprobe analysis of glass before and after impact. The first column gives the mean and standard deviation of the initial MORB glass. The second column gives the composition of the pre-heated MORB glass. The last three columns give the analyses of shocked glass recovered from three shock wave experiments.

pressure are not systematic, but are still significantly greater than the standard deviation of the measurements. These include increases in Al_2O_3 and Na_2O and decreases in TiO_2, MgO and CaO in the shocked glass compared to the initial MORB glass (Tbl 2.1).

Analyses of post-shock glasses were obtained on areas devoid of metal spheres, alumina fibers and other obvious heterogeneities. Among the shocked glasses, SiO_2, Al_2O_3 and Na_2O proportions were the most variable with Al_2O_3 ranging from 4 – 20%. The compositional variability within each sample probably reflects variable degrees of contamination by external material (as described earlier for fragment # 834) and local loss of Fe and Si to metallic Mo-rich melts. However, we did not find any systematic chemical variations in the glass as the boundary with Mo or any of the larger metal spheres was approached, ruling out the possibility of a significant diffusion gradient near the Mo-shocked glass interface.

Metallic Phases

Metal is found in three texturally distinct occurrences: essentially pure Mo from the sample holder, rare, Al-rich regions and Fe-Mo-Si-rich spheres. Knowledge of the relatively simple binary and ternary metal phase equilibria compared to silicate liquid equilibria allows us to estimate probable temperatures experienced by these fragments.

The main Mo metal fragments are essentially pure Mo with no chemical variation to suggest reaction with the MORB liquid or other external materials (Table 2.2) as the interface with the silicate melt is approached.

Recovered samples from the two higher pressure shots (760 and 824) contain Al-

Figure 2.10: Plot of the FeO (wt %) in the shocked MORB normalized to the initial concentration in the unshocked MORB versus the MORB Hugoniot pressure. The trend shows a consistent decrease in FeO with increasing pressure. At 6 GPa almost all the FeO is gone from the MORB glass (Table 2.1).

FeO Variation in Shocked Glass
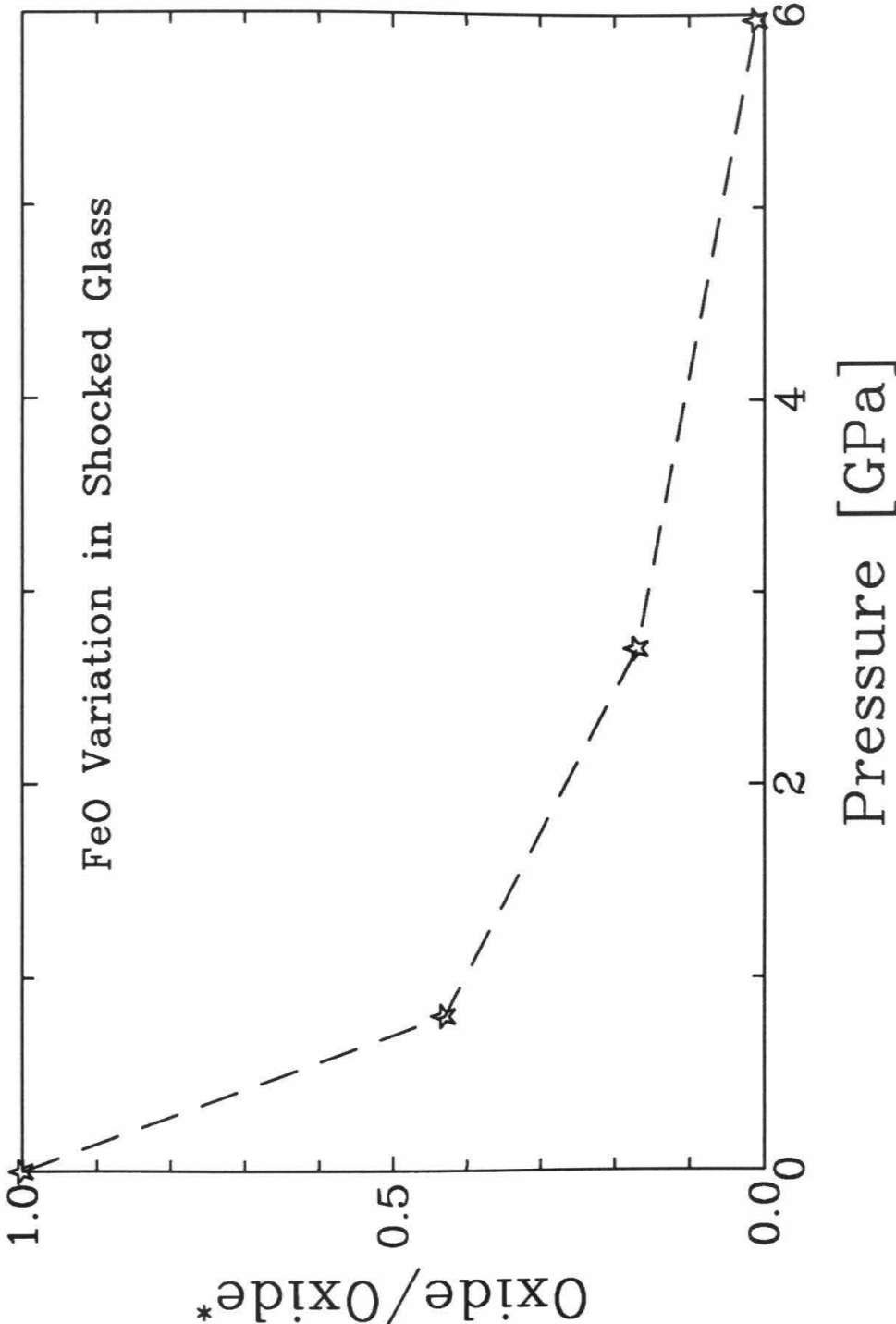
Wt %	Metal
Mo	100.29 ± 0.18
Cu	0.025 ± 0.007
Al	0.015 ± 0.004
Pt	0.014 ± 0.004
Fe	0.013 ± 0.006
Mn	0.013 ± 0.003
Ni	0.013 ± 0.004
Ca	0.007 ± 0.002
Si	0.006 ± 0.001
Na	0.006 ± 0.001
K	0.005 ± 0.001
Cr	0.003 ± 0.002
Ti	0.002 ± 0.001
Mg	0.000 ± 0.000
TOTAL	100.41 ± 0.18
Points	16

Table 2.2: Analysis of shocked molybdenum. Mean and standard deviation of element concentrations determined on the electron microprobe. The analyses were done on six fragments (7601a,c 8241-4a,b and 8261-3a,b).

rich regions primarily found near the interface between the shocked liquid and Mo metal (Figures 2.5 and 2.6). The average composition for the gray regions analyzed in polished cross sections, 7601c and 8241-4c, are given in Table 2.3. The composition of the metal in the more highly shocked fragment, 8241-4c, is approximately Al_3Mo. According to the work of *Schuster and Ipser* [1991] on the Al-rich end of the Al-Mo binary, Al_3Mo melts at $\sim 1530^{\circ}C$ and requires long annealing times to reach equilibrium at temperatures less than $1100^{\circ}C$. They also noted that this composition is slow to decompose at lower temperatures making it likely that the alloy in these fragments was produced at high temperatures and cooled too quickly to allow decomposition. This binary composition also suggests a reduced atmosphere, well below iron-wüstite (IW), because *Gubbels* [1991] has noted an increased solubility of Al in Mo as the oxygen partial pressure is reduced below 10^{-16} bars (at $1400^{\circ}C$). The Al-rich metal in 7601c is more complex compositionally, roughly $FeSi_2Al_4$. Using the Fe-Si-Al phase compilations of *Raynor and Rivlin* [1988] it can be shown that this alloy probably represents a quenched liquid that solidified around $800^{\circ}C$. The Fe-Si-Al ternary is a relatively complex system noted for supercooled liquids, incomplete solid reactions, metastability, the coexistence of many phases in the Al-rich corner and complex crystal structure. Although $FeSi_2Al_4$ has been described by some workers, it is not considered one of the stable solid ternary phases [*Raynor and Rivlin,* 1988]. Therefore the Al-rich regions in our fragments probably represent supercooled liquid phases that did not have enough time to undergo any significant solid-state diffusion because of the sluggishness of such reactions in this ternary system. We may estimate the temperature at which this phase quenched by projecting the normalized Fe-Si-Al

composition onto the ternary liquidus projection of *Raynor and Rivlin* [figure 3.41, 1988]. The liquidus temperature is $\sim 850^\circ$C.

The spheres from fragments 7601a and c are basically ternary Mo-Fe-Si alloys with minor concentrations of Cu and Ti (Table 2.4) and generally consist of at least two phases, one Mo-rich and the other Fe-rich (Figures 2.5 and 2.7a,b and c). Pure Mo melts at 2623°C, far above our calculated temperature range, but the addition of Fe and Si to the Mo particles reduces the melting point of the metal alloys that form. Using an experimentally determined Mo-Fe-Si ternary phase diagram [*Raynor and Rivlin,* 1988] and the chemical analyses given in Table 2.4, we can estimate the composition of the alloys and their melting temperatures. The average composition of all the spheres analyzed in fragment 7601a is $Fe_3Si_6Mo_2$, while all the spheres in fragment 7601c average to Fe_4Si_2Mo. The Mo-rich (White areas in BEI) regions of the spheres are $\sim Fe_6Si_4Mo_3$, while the Fe-rich (Gray areas in BEI) regions of the spheres are $\sim Fe_2Si$. In Figure 2.11, the compositions of all the analyzed spheres are plotted on the ternary Mo-Fe-Si liquidus surfaces. The temperatures estimated from these surfaces indicate the spheres formed within or above ~ 1900 to 1100°C. The higher temperature alloy liquids (Mo-Si-rich spheres) may result from a localized hotter region within the shock-heated fragment. The temperature of the sphere may increase due to the heat of reaction produced during the formation of the alloy. In general, most of the metallic phases fall well within or below our estimated peak temperature range of $1400 - 1700^\circ$C. We note that the ternary liquidus phases only provide a lower limit to the actual temperatures produced by the impact.

Wt %	7601c	8241-4c
Si	23.61 ± 4.33	0.42 ± 0.03
Ti	0.013 ± 0.007	0.008 ± 0.008
Al	48.20 ± 2.86	40.86 ± 1.72
Fe	23.91 ± 1.26	2.05 ± 0.22
Mg	0.014 ± 0.007	0.00 ± 0.00
Ca	0.081 ± 0.008	0.028 ± 0.006
K	0.003 ± 0.002	0.002 ± 0.002
Na	0.023 ± 0.008	0.007 ± 0.007
Mn	2.69 ± 0.26	0.27 ± 0.08
Ni	0.005 ± 0.005	0.00 ± 0.00
Cr	0.05 ± 0.01	0.020 ± 0.002
Mo	0.16 ± 0.09	50.63 ± 0.26
Pt	0.00 ± 0.00	0.004 ± 0.004
Cu	3.16 ± 1.60	7.02 ± 0.80
TOTAL	101.93 ± 0.64	101.34 ± 0.45
Points	4	2

Table 2.3: Analysis of gray regions of fragments.

Wt %	7601	7601c	White	Gray
Si	30.12 ± 3.79	15.78 ± 1.92	14.62 ± 3.37	17.97 ± 2.60
Ti	1.30 ± 0.73	$0.54 \pm .20$	0.58 ± 0.33	0.39 ± 0.24
Al	0.16 ± 0.03	0.13 ± 0.09	0.12 ± 0.09	0.49 ± 0.34
Fe	28.60 ± 8.25	57.61 ± 3.70	45.85 ± 4.07	71.29 ± 4.18
Mg	0.02 ± 0.01	0.07 ± 0.05	0.04 ± 0.04	0.27 ± 0.21
Ca	0.16 ± 0.03	0.25 ± 0.05	0.23 ± 0.02	0.45 ± 0.22
K	0.006 ± 0.002	0.01 ± 0.004	0.01 ± 0.01	0.01 ± 0.01
Na	0.07 ± 0.02	0.10 ± 0.07	0.05 ± 0.05	0.36 ± 0.28
Mn	0.51 ± 0.11	0.39 ± 0.09	0.28 ± 0.14	0.46 ± 0.16
Ni	0.03 ± 0.01	0.04 ± 0.009	0.05 ± 0.03	0.05 ± 0.02
Cr	0.14 ± 0.04	0.21 ± 0.02	0.25 ± 0.03	0.17 ± 0.04
Mo	37.16 ± 6.52	23.23 ± 4.48	37.69 ± 0.24	5.50 ± 1.85
Pt	0.25 ± 0.09	0.02 ± 0.01	0.03 ± 0.01	0.07 ± 0.01
Cu	1.24 ± 0.28	1.44 ± 0.27	0.48 ± 0.20	2.55 ± 0.52
TOTAL	99.78 ± 0.50	99.85 ± 0.20	100.27 ± 0.18	100.04 ± 0.41
Points	9	13	3	3

Table 2.4: Electron microprobe analysis of metal spheres in fragments 7601a and 7601c. The values represent the mean and standard deviation of the mean for many individual analyses. White indicates analyses done on white regions of the sphere and Gray indicates analyses done on gray regions of the sphere. Bulk composition was determined from mass balance.

Figure 2.11: Projection of the primary liquidus surfaces for the Fe-Si-Mo system. The heavy lines with arrows represent the univariant lines of equilibrium between liquid and two crystalline phases. The invariant points (intersections of the lines) are marked by the temperature (^{o}C) at which the reaction has been experimentally determined to occur. The dashed lines show hypothetical relations. The phases labelled with letters are: s - deposited as a liquidus phase of $\sim 34\%$ Fe, 58% Mo, 8% Si, R - taken from the Mo-Fe binary with saturated solid solution of Si to give 42% Fe, 50.5% Mo, 7.5% Si which has been suggested to crystallize congruently at 1610°C and t_1 - formed incongruently at $\sim 1440^o$C from a liquid of $\sim 51\%$ Fe, 25% Mo, 24% Si to form a solid of $\sim Fe_2MoSi_2$. The composition of the metallic spheres analyzed from fragment 7601 are plotted as open circles, the pairs of shaded circles represent individual anaylses of Fe-rich versus Mo-rich regions within one spherule. This figure is modified from *Raynor and Rivlin* [1988].
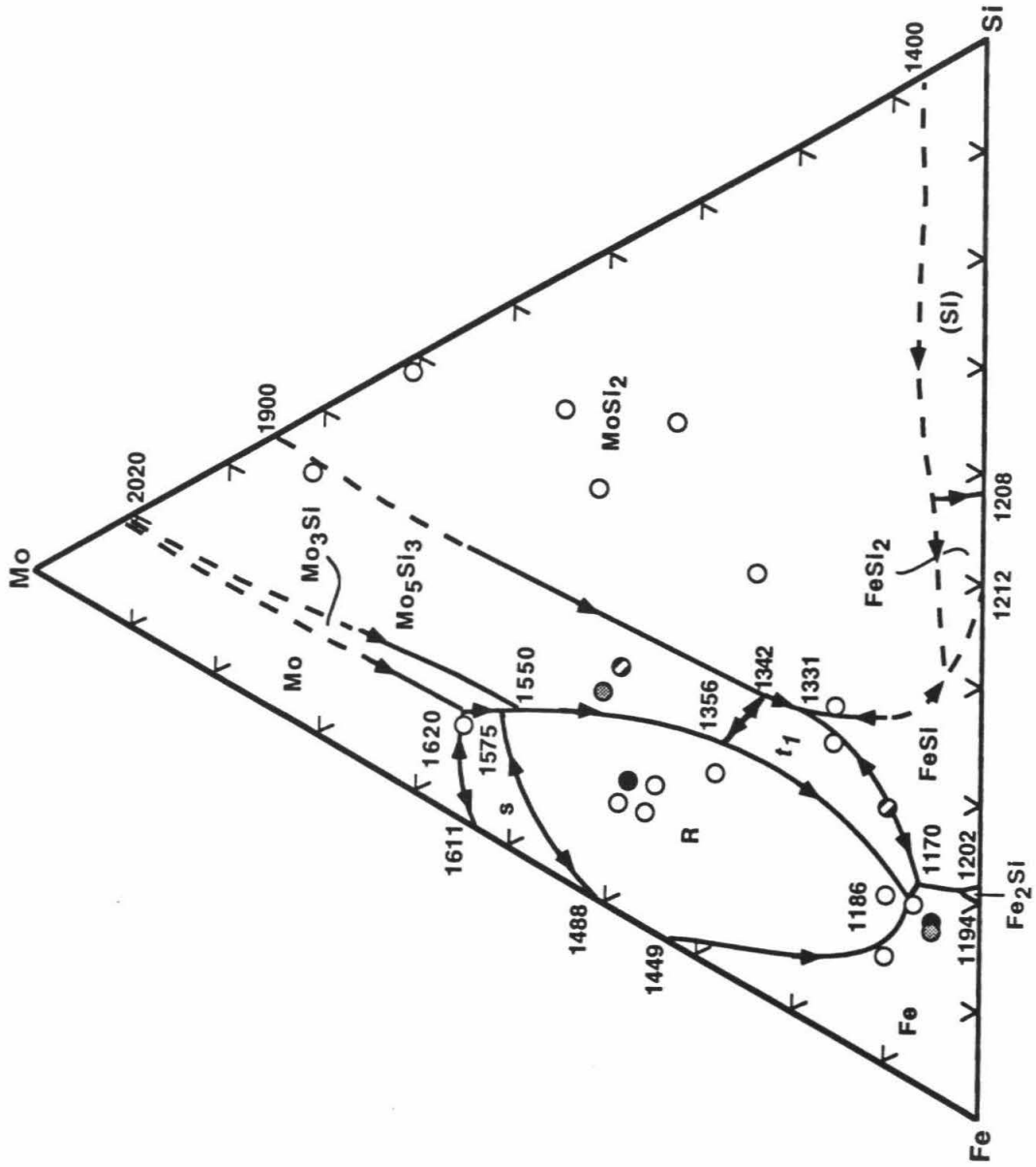
2.4 Post-Shock Conditions

The observed chemical changes are due to post-shock reactions induced by the impact for the following reasons. First, there is little contamination or mixing between the Mo sample holder and the MORB sample prior to impact (Table 2.1). Second, the shock process and the accompanying release to zero-pressure occur on a very short time scale ($\sim$1.3 μs) and there is not enough time for chemical diffusion to produce the observed textures and chemical variations. There is evidence of some diffusion taking place in the fragments, but the overall gross features we observed are derived from another mechanism (primarily the turbulent motion of hot Mo particles in the liquid).

The shock process begins when the flyer impacts the target. Upon impact, very high pressures, temperatures and velocities are produced and a shock wave is propagated forward into the driver and reflected backward into the flyer. When the shock wave reaches a free surface it is converted to a release wave that moves back through the material, decompressing it. When this rarefaction wave reaches a free surface, the material fragments. The complex geometry of our target makes it hard to quantify the velocity of the rarefaction wave but the characteristic fragmentation time for the target, τ, can be approximately estimated by [*Asphaug et al.*, 1991]:

$$\tau \sim \frac{2D}{0.4C_L} \tag{2.1}$$

where D is the diameter of the target and C_L is the longitudinal wave speed or the shock wave velocity. For shot # 760, the Mo driver will fragment in approximately 44 μs, assuming D = 4.4 cm and C_L = 5.07 km/s. If we assume that the rarefaction

wave transit time was the same as the shock wave transit time (~ 2 μs, see Table 1.3),
then the Mo driver fragmented in less than 48 μs, far too short a time to account for
the observed textural and chemical changes. These reactions must have taken place
in the post-shock state.

2.4.1 Pressure and Temperature

Although impacts in the shock wave experiments produced transient high pressures,
the pressure of equilibration was post-shock and hence effectively ambient because
the target has been decompressed and disseminated. The post-shock temperature
will not be reduced as much as the pressure and may only decrease by about 50°C.
Given the many possible mechanisms (heat of reaction, heat of fusion, mechanical
heating, temperature gradients etc...) by which the post-shock fragment may initially
retain or even gain heat, we will use the estimated temperature range ($1400 - 1700^{\circ}$C)
given earlier for shot# 760, for the post-shock state. This temperature range is also
consistent with the phase equilibria for many of the metallic phases observed in
fragments from shot# 760, as discussed above.

2.4.2 Oxygen Fugacity

The oxygen fugacity in our experiments was neither controlled nor measured directly.
A rough approximation can be calculated from the phases identified in the fragments.
The formation of iron silicides, particularly Fe_2Si, and molybdenum aluminates, such
as Al_3Mo, indicate reduction of oxides from the shocked liquid to the metallic phases.
Figure 2.12 shows the relevant oxygen buffers estimated from $-\Delta G_T = RT\ln K$ in the
temperature range of interest (using thermodynamic data from *Robie et al.* [1978]).

There is a large reduction in fO_2 between the Mo – Mo oxide and IW buffers and the Si – SiO_2 buffers. Initially the target is heated and the fO_2 is maintained below the Mo buffers but above the IW buffer in the gun tank by evacuating it to 100 μm Hg to prevent oxidation of the polished Mo surfaces. After impact, significant reduction occurs to form the metallic spheres by heating and unmixing the immiscible silicate and metal liquids. The composition of the spheres (Figure 2.11) is concentrated near the Fe-Si corner and the average composition of the gray regions of the spheres is $\sim Fe_2Si$ (Table 2.4). Using thermodynamic data for $\sim Fe_2Si$ [*Zaitsev et al.*, 1992] we can estimate the oxygen fugacity of the system from the reaction:

$$2FeO + SiO_2 \rightarrow Fe_2Si + 2O_2(g). \tag{2.2}$$
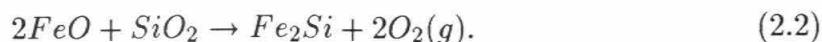
The activities of Fe (0.7), Si (0.3), FeO (0.013) and SiO_2 (0.59) were assumed to be equal to the mole fraction of each component in the metallic spheres and shocked liquid, respectively. This approximate buffer plots close to the SiO_2-Si buffer and is very reducing. At 1400°C, the oxygen fugacity is roughly 10^{-17} bars, about 8 log units below the initial oxygen fugacity.

There are some examples from the geologic literature of extreme reduction of silicate liquid oxides to form metallic compounds. *King* [1983] observed in-situ reduction of FeO to metallic Fe spheres for basalt standard BCR-1 by high temperature heating (2400 - 3000°C) in a solar furnace under vacuum. The author noted that significant Fe reduction and evaporation will occur at temperatures greater than 1800°C in a vacuum, if heating is applied for a few minutes to tens of minutes, depending on the partial vapor pressures of the phases in the system.

Figure 2.12: Plot of temperature versus oxygen fugacity for the system showing the positions of the relevant metal-oxide buffers along with the estimated Fe-Si alloy-FeO-SiO$_2$ buffer. Thermodynamic data was taken from *Robie et al.* [1978] and the Mo-MoO$_3$ buffer is discontinuous because there was no data above 1237°C. After impact, the temperature of the sample is increased and the oxygen fugacity is drastically reduced in the direction of the arrow.
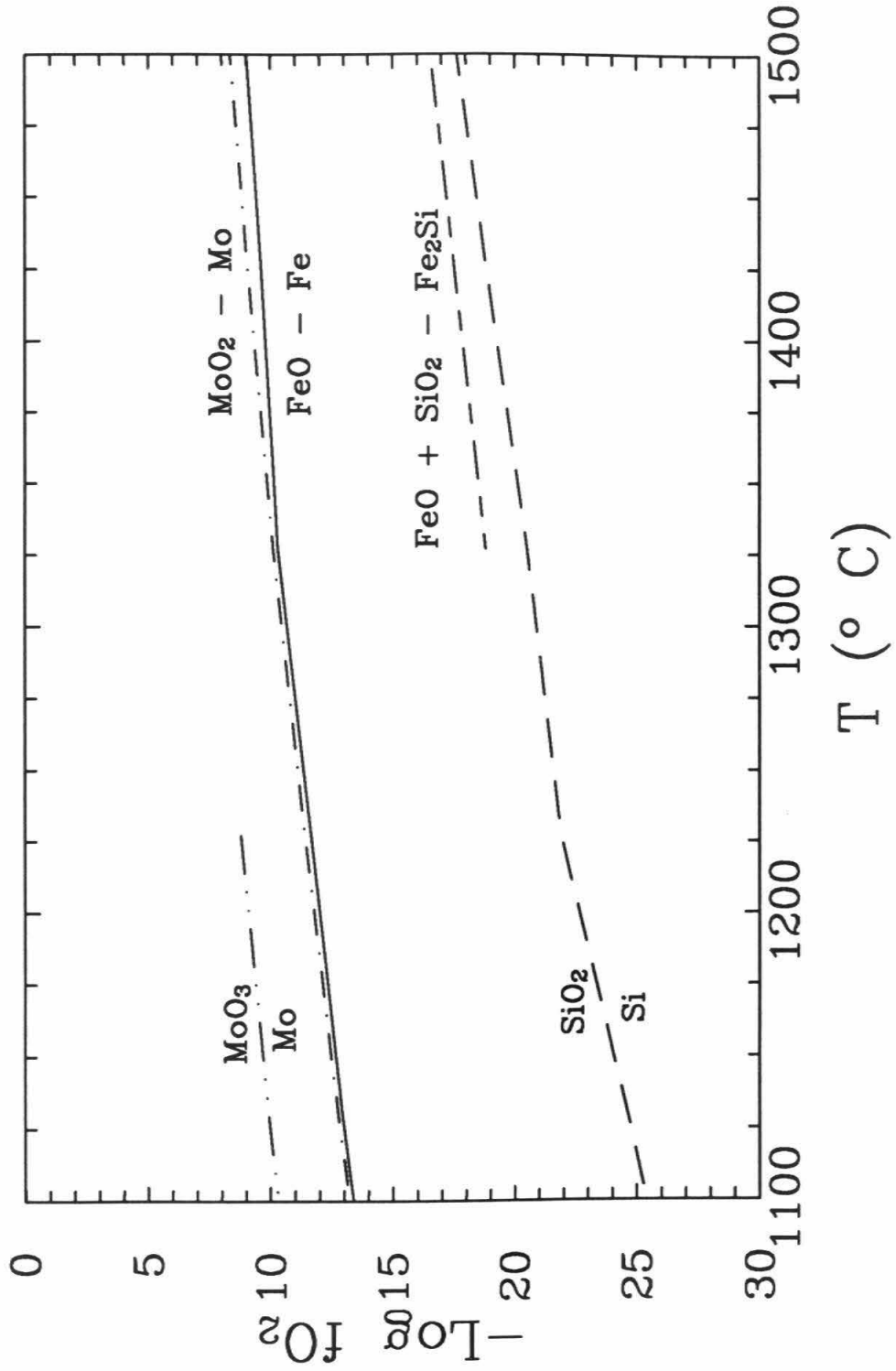
Other experiments done at high pressures and temperatures [*Ringwood and Hibberson* 1991; *Goarant et al.*, 1992, *Knittle and Jeanloz*, 1989] have looked at the reaction between Mg-Fe-Si-rich silicate and Fe-rich metals. In general these experiments show a drastic reduction of the most soluble oxide, FeO, from the silicate into the metallic phase and the formation of FeO-SiO_2-Fe_xSi_y phases. *Ringwood and Hibberson* [1991] indicated that SiO_2 will become soluble in Fe liquid when the activity of the major buffering oxide (FeO) falls to an appropriately low value.

By far the most analogous naturally occurring example of extreme reduction on a short time scale is the production of fulgurites (fused vesicular glasses produced by lightning strikes). *Essene and Fisher* [1986] studied a fulgurite deposit formed in a glacial till and noted the occurrence of metallic spherules (e.g., iron silicides and phosphides) in the glass. They estimated a substantial range of fugacity was needed to explain the phase relations [*Essene and Fisher*, 1986, see figure 3] and they suggested some possible reduction mechanisms. The presence of C from tree roots might provide a good oxidizing agent that would take up the oxygen released from the FeO and SiO_2 reduction in a process analogous to smelting. They noted that similar compositions have been produced experimentally by superheating silicates in the presence of C. Also the rapid formation of nitrous oxides due to passage of lightning through air might remove oxygen from the system. Another possibility would be degassing or vaporization of oxygen as indicated by the substantial vesicularity in the glass.

The strong reduction in our shocked liquid may be attributed to several possible mechanisms. The most obvious is reduction of FeO and SiO_2 accompanied or

followed by oxidation of Mo. Mo should oxidize very rapidly at relatively low temperatures (> 400°C) and sublimation of MoO_3 begins at temperatures >700°C in the presence of oxygen. Given the high temperatures experienced by the fragment, the reduction may have taken place first and rather rapidly providing a source of extra oxygen which was then quickly oxidized and degassed from the fragment before it could cool below the sublimation temperature of MoO_3 and also while the shocked silicate was still liquid. The problem with Mo oxidation is the lack of any significant increase in MoO_3 in the shocked glass, the spheres contain Mo metal and the exposed surfaces of the large pieces of metal show almost no evidence of oxidation. Even though most of the MoO_3 will sublime, some will oxidize as the fragment cools and tarnish the metal. Thus it seems that if Mo was oxidized, it was effectively degassed from the shocked liquid at high temperature and any surface film of Mo oxides on the metal surface are too thin to detect.

Other possible oxidizers include C and N residues from the gunpowder or the wood recovery system for shots 826 and 824. The recovered fragments from shots 826 and 824 were more vesicular than the glasses from shot 760 and this may be related to increased oxidation of the cooling melts within the wood recovery system.

2.4.3   Mass Balance

It is important to attempt to balance the starting element concentrations, Mo metal and MORB glass to get the bulk compositions of the spheres. Considering only the major elements Si, Fe and Mo we can balance the concentrations according to:

$$X \ (Mo) \ + \ Y \ (MORB) \ \rightarrow$$

Z (shocked glass) + W (Mo-rich sphere) + G (Fe-rich sphere)   (2.3)

for shot# 760 using the data from Tables 2.1 and 2.4 renormalized to 100% for the three elements. Since we would like a unique solution we chose to set the values of X and Y and solve the three equations (one for each element) for the three unknowns Z, W and G. This leads to three equations (one for each element) in the three unknowns Z, W and G with a solution:

5%(Mo) + 95%(MORB) →

70%(shocked glass) + 10%(Mo-rich sphere) + 20% (Fe-rich sphere).(2.4)

This solution was chosen from several choices using the additional observation that there is approximately twice as many Fe-rich regions as Mo-rich regions in the spheres. Only Eqn. 2.4 gave a mass ratio approximately consistent with the observed volume ratio of Mo-rich to Fe-rich spheres. The bulk composition of the spheres can be derived from these percentages (Table 2.4).

2.4.4 Cooling Time

The cooling time for fragment 7601 can be estimated by assuming it acts like an ideal black body and cools radiatively. This assumption is only realistic for this fragment because it cooled on the floor of the gun tank rather than in the wood recovery system like fragments from shots 826 and 824. We have assumed any thermal conduction from the metallic droplets within the shocked liquid is negligible because the spheres are very small, they occupy less than 5% of the volume of the liquid swath and the thermal conductivity of liquid metal is much lower than the conductivity of the

solid. Although there is some turbulent motion of metal particles in the liquid as indicated by the textures in Figure 2.6, convective cooling is ignored because there is not enough time to set-up any significant flow (i.e., no stable convection cells) in such a thin layer of liquid. For radiative cooling the heat loss is defined as:

$$q = \sigma(T^4 - T_o^4) \tag{2.5}$$

where q is the heat lost, σ is the Stefan-Boltzmann constant, T is the maximum post-shock temperature, which we conservatively assume to be 1700^oC and T_o is room temperature ($\sim 30^o$C). The conservation of energy equation is:

$$\rho C_v \frac{DT}{Dt} = -\nabla \cdot q \tag{2.6}$$

where ρ is the density, C_v is the heat capacity at constant volume and t is time. Substituting Eqn. 2.5 into Eqn. 2.6 yields:

$$\frac{DT}{Dt} = \frac{-A\sigma}{\rho C_v V}(T^4 - T_o^4) \tag{2.7}$$

where A is the area of the plate and V is the volume of the plate. Solving the derivative numerically, we obtain a cooling history for the fragment. The area is divided by the volume in Eqn. 2.7, so the only required dimension is the thickness of the plate. Separate calculations were done for the Mo plate and MORB plate because of differences in material properties and thicknesses. The cooling rate of the spheres will be controlled by the cooling rate of the liquid that surrounds them so we have not calculated a separate cooling time for the spheres. Using maximum and minimum dimensions estimated from the SEM photomicrographs and material

parameters given in Table 1.3, limits were placed on the maximum and minimum time needed to cool each material from a temperature of $1700^{\circ}C$ to $800^{\circ}C$. The lower temperature bound comes from our estimate of the liquidus temperatures for the Fe-Si-Al alloy in 7601c. It is assumed that once this alloy is below its liquidus, diffusion between the metal and silicate is restricted. Figure 2.13 shows that the MORB plates cool in $\sim$1.5 – 3.0 s, while the Mo plates cool to $800^{\circ}C$ in $\sim$6.5 – 13 s. The slower cooling rates of the thicker Mo plates will dominate the cooling rates of the fragment, so we assume a conservative cooling rate of 140 – 70 $^{\circ}C/s$.

2.4.5 Scenario for Sphere Formation

Based on the above post-shock conditions, we suggest the following scenario for the formation of the metallic spheres found in fragments recovered from shot# 760. Micron-size bits of hot Mo ejecta were ingested into the MORB liquid at temperatures between 1400 – $1700^{\circ}C$ and turbulently mixed with the shocked liquid. The motion of these particles is indicated by fluid streams of spheres as mentioned earlier. These microscopic fragments, reacted with the MORB liquid and leached out the more siderophile elements of the basalt under a very reducing environment ($\sim 10^{-17}$ bars at $1400^{\circ}C$). In particular, FeO was reduced to Fe and the Fe was strongly and rapidly drawn into the growing metallic liquid. Si, which is not normally viewed as a siderophile element, is also partitioned into the metal suspension because of the reduced conditions, its solubility in Fe and Mo and its stabilizing effect on the Mo-Fe-Si ternary alloys [*Raynor and Rivlin,* 1988]. The addition of Fe and Si lowers the melting point of Mo causing melting of the metal alloy. Once the metal is completely molten it forms the typical spherical shape of metallic liquids. These

Figure 2.13: Radiative cooling time (see Eqn. 2.7) for a MORB plate and Mo plate at two different thicknesses.
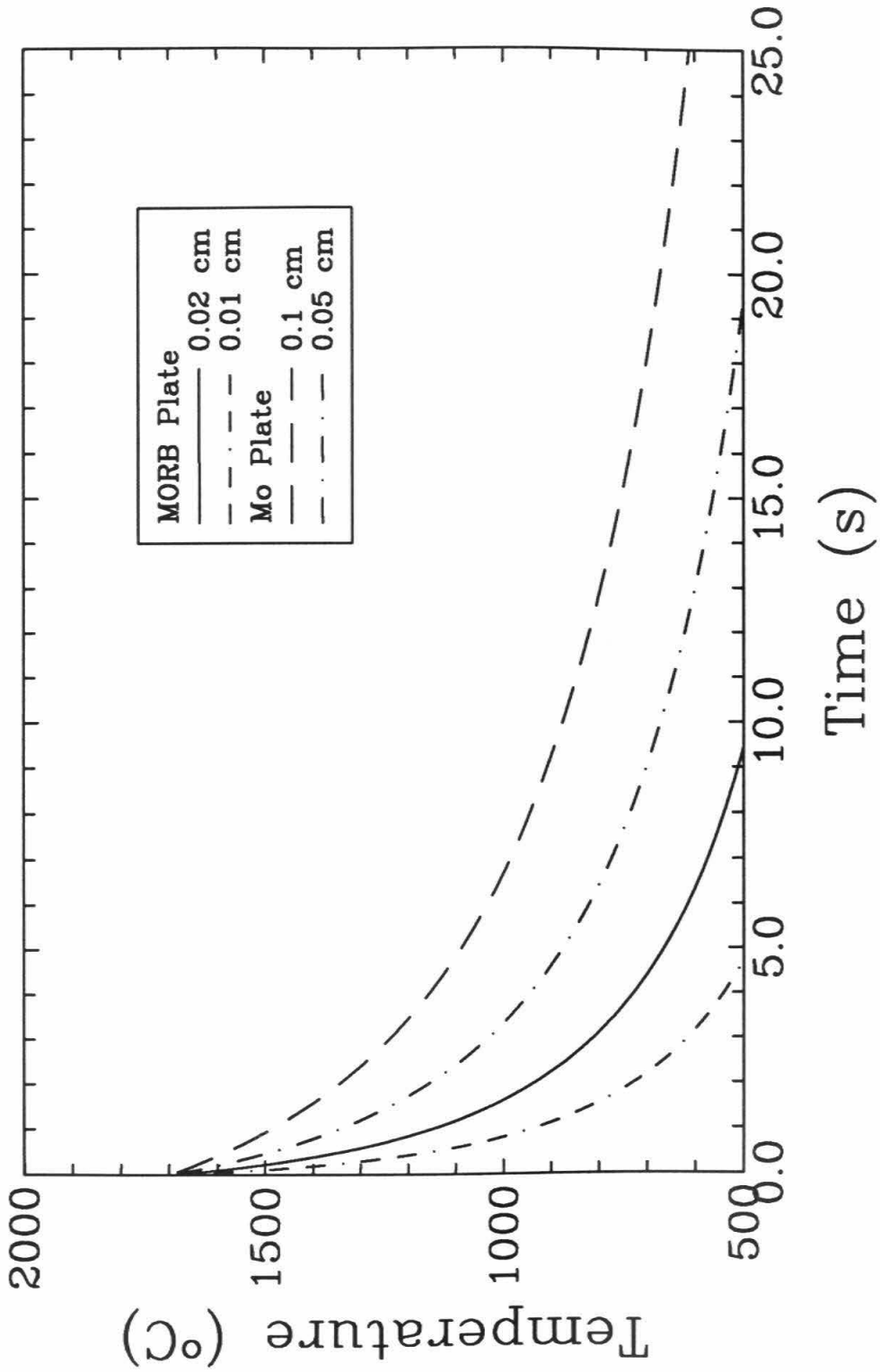
spheres will cool relatively slowly (70 – 140 ^{o}C/s) because they are surrounded by a thermal insulator, the shocked liquid. The slower cooling will allow further separation and homogenization of the binary and ternary alloys producing cellular to globular textures in the solidified spheres. However the cooling rate is probably fast enough to quench the metallic phases before they reach equilibrium. This is indicated by the presence of high-temperature alloys that are not stable at lower temperatures (essentially quench products), observed in many of the metallic particles. Also the skeletal crystal growing within the sphere in Figure 2.5 indicates this sphere cooled slow enough to allow crystal growth to start, but fast enough to quench the crystal before it could complete its growth.

We would like to emphasize that the rapid and significant changes in the texture and chemistry of the silicate and metal can be attributed to the initial liquid state of the silicate sample and the dynamic shock process. Starting with a completely molten sample allows the metal ejecta to more easily, turbulently flow through the liquid and react with it. The mobility of the elements within the molten silicate is also enhanced in the liquid state versus a partially molten or solid-state. The shock process increases the reactivity of the metal-silicate system by instantaneously pressurizing and superheating the target, then fragmenting and mixing the metal with the silicate. *Yu et al.,* [1992] have compared the rates of reactions for the production of silicides by dynamic shock compression versus static solid state diffusion and found that the diffusive rates are $10^7 - 10^9$ times faster for the dynamic, shock experiments. It is evident that the increased entropy and temperature of the mixed system is impact-induced and that slow cooling rates are necessary to allow the sys-

tem to equilibrate. The present system did not achieve equilibrium as evidenced by the variability in composition of the shocked glass and metallic spheres.

2.5 Discussion

2.5.1 Implications of Disequilibrium Textures

The textures observed in fragments from shot # 760 show the immiscibility of metal and silicate liquids and disequilibrium quench products produced on short time scales. Similar textures, although different chemistry, are seen in samples from impact sites on the earth and moon and in experiments designed to simulate materials found at these sites.

There are several meteoritic impact sites on earth that contain metallic particles with similar textures as the spheres in fragment 7601. Fe-Ni-rich metallic spherules found at impact craters such as Meteor Crater, Arizona [Kelly et al., 1974] Henbury, Australia [Brett, 1967] Ramsdorf, Germany [Begemann and Wlotzka, 1969] and Wabar, Saudi Arabia [Spencer, 1933] are attributed to shock melting of a meteoritic impactor. Studies of the shocked glasses found at Meteor [Mittlefehldt et al., 1992] and Wabar [Hörz et al., 1989] also indicate mixing of the iron meteorite with the target. Thus for many impact sites on earth the origin of the metallic particles is clearly related to dissemination of the meteorite and its subsequent mixing with the melted target material. These conclusions are consistent with our observations that the Mo-Fe-Si spheres are formed by mixing the comminuted impactor with the melted target. In our case, we assume the Mo driver is the impactor and the molten basalt is the target. Disequilibrium mixing and melting on extremely short time

scales is characteristic of the shock process because the supersonic compression wave causes rapid, irreversible compression accompanied by superheating and turbulent mixing of the target and impactor. Although the origin of many metallic particles found at impact sites on the earth are well understood, there are some heterogeneous spherules whose origin is more complicated. For example, metallic particles from East Clearwater Crater, Quebec may have a more complicated formation mechanism because they consist of sulphides, magnetite and refractory silicates [*Grieve et al.*, 1980]. *Grieve et al.* [1980] suggested an origin with limited mixing between the projectile and target in the initial stages of the impact in order to explain the refractory silicate phases, but it seems likely from our results that intimate mixing between the target and impactor was significant very early in the shock process.

Fe-rich metallic spherules found in lunar samples have textures similar to the spheres found in our recovered fragments. *Blau and Goldstein* [1975] used the textures of Fe-Ni-rich spherules from lunar rocks and soils to determine their thermal history. They compared lunar spherules to experimentally-produced spherules to derive cooling rates for the spheres. Their experiments produced spherules with fine-scale dendritic to cellular textures and cooling rates of $7 \times 10^2 - 10^6$ °C/s. Less than 10% of the sampled lunar spherules have dendritic textures indicating fast cooling, attributed to radiative cooling of isolated, ejected metal droplets. These fine scale dendritic textures and their origin as isolated, superheated particles in an atmosphere are consistent with the textures observed in cosmic spheres found in sediments which are suggested to have formed by melting of planetary dust and other extraterrestrial particles as they enter the earth's atmosphere before deposition [*Taylor and Brown-*

lee, 1991]. The majority of the lunar spherules have globular textures, unlike those observed in *Blau and Goldstein's* [1975] experiments. *Blau and Goldstein* [1975] suggest these globules formed during slower cooling of the liquid metal spherules within a silicate melt. Thus the spherules do not cool quickly by radiating their heat directly to the atmosphere, but are limited to slower cooling dependent on the cooling rate of the surrounding silicate. The spheres produced in our experiments have globular textures and are enclosed in the shocked liquid. We have also determined a relatively slow cooling rate for the entire fragment which limits the cooling of the spherules to be relatively slow. Therefore the cellular to globular textures of our insulated, slowly cooled spherules confirms the hypothesis of slow cooling for lunar particles with similar textures and indicates that these spherules may have cooled within a silicate liquid (*i.e.,* a melted target).

2.5.2   Implications of Chemical Changes

The chemistry of our spheres is not analogous to impact melts or experimental studies because of the presence of Mo, however the substantial reduction reaction that allows the formation of iron silicides within a SiO_2 -rich liquid may be related to reaction processes on the earth and moon. There are few natural examples of such a change in oxidation state from near IW to Si-SiO_2 (a change of $\sim$8 log units of fO_2) with the exception of fulgurites [*Essene and Fisher,* 1986].

Experiments carried out at high pressure and temperature have produced Fe-Si phases indicating the solubility of Si in Fe and implying that Si may be a good candidate for a light element in the earth's Fe-rich core. *Ringwood and Hibberson* [1991] noted in their high pressure ($\sim$16 GPa) and temperature ($>1700^\circ$C) experiments be-

tween silicates and Fe metal that FeO is extracted into molten Fe until the activity of FeO is decreased enough so that SiO_2 becomes soluble in molten Fe and Fe-Si alloys can form. They noted that SiO_2 becomes more soluble in molten Fe with increasing temperature and pressure. *Knittle and Jeanloz* [1989] also noted the dissolution of SiO_2 from perovskite to form disequilibrium quench products of stishovite, FeO and Fe_xSi_y in their diamond anvil melting experiments. *Goarant et al.* [1992] noted the drastic depletion of FeO from oxides in contact with metal phases in their diamond anvil melting experiments between solid silicates and molten Fe-alloys. Our experiments were performed at much lower pressures and slightly lower temperatures in the presence of Mo metal rather than Fe, but the Mo and Fe buffers are close enough to assume that conditions of formation of the iron-silicides are similar in terms of oxygen fugacity. The main difference may be that Mo enhances the reduction of FeO and SiO_2 by providing a good oxidizer. Therefore the efficient reduction of oxides and the solubility of Si in molten Fe can occur at ambient pressures and high temperatures in the presence of a strong oxidizer.

Another key parameter used to model core formation on the earth is siderophile abundances and partition coefficients. The partition coefficients are dependent on the temperature and oxygen fugacity of the system in which they partition and no one has developed a model that satisfies the siderophile element abundances in the upper mantle of the earth. Barring the appropriate experiments, the next best method to solve the siderophile excess problem in the earth's upper mantle is to determine the trends of the partition coefficients as a function of temperature and oxygen fugacity using experimental results determined under different conditions. Once the general

trends have been estimated for each element then the higher temperature partition coefficients can be extrapolated using these trends.

Partition coefficients are determined by measuring the concentration of the element in the two adjacent phases under equilibrium conditions. In our case, the system has not reached equilibrium, but the mass balance calculation gives us the bulk composition of the spheres for a closed system that achieved equilibrium. Therefore using the bulk composition of the spheres (Table 2.4) and the composition of the shocked glass (Table 2.1) we can calculate partition coefficients for Fe between the silicate liquid and the molten metal spheres. The partition coefficient is defined as:

$$D_x^{\frac{LM}{LS}} = \frac{C_x^{LM}}{C_x^{LS}} \tag{2.8}$$

where x is the element of interest (i.e., Fe), C_x^{LM} is the concentration of that element in the liquid metal and C_x^{LS} is the concentration of the element in the liquid silicate. The results are compared to the partition coefficients measured by *Schmitt et al.* [1989] in Table 2.5. *Schmitt et al.* measured partition coefficients of siderophile elements between solid metal (Fe-Ni-rich, with minor amounts of various siderophile elements including Mo) and a tholeiitic melt at $1300^\circ C$ over a range of fO_2's ($10^{-13} - 10^{-11}$ bars). Table 2.5 shows that the siderophile character of Fe increases as temperature increases and oxygen fugacity decreases. Although we were unable to determine partition coefficients of Fe for each of the three shots studied here, the systematic decrease in FeO in the shocked glass (Figure 2.10) suggests that the liquid metal-liquid silicate partition coefficient for Fe increases as

the temperature increases. *Schmitt et al.* [1989] compared their results for Fe to *Seifert et al.'s* [1988] for partitioning between metal, olivine and melt at $1260^{\circ}C$ and $1420^{\circ}C$. They found that the extrapolated trends indicate increasing partition coefficients with increasing temperature along a given oxygen fugacity buffer. *Schmitt et al.* [1989] have noted that other siderophile elements (particularly those more siderophile than Fe) show the same temperature dependence as Fe, namely increasing D's with increasing temperature. This same dependence was not seen for all the siderophile elements however, and is not consistent with the extrapolation of *Murthy* [1991] which requires all elements more siderophile than Fe to have decreasing D's as temperature increases. *Murthy's* method basically ignores the dependence on oxygen fugacity and would only be accurate if the siderophile element entered the melt as a neutral species. *Colson's* [1992] experiments have shown that Ni may partition into a silicate melt as a neutral species (Ni^{o}) at reducing fO_2 and once the element is neutral it does not depend on the oxygen fugacity anymore. For this case, Murthy's method is appropriate. The production of neutral species may occur at high temperatures and reducing atmospheres, such as produced in an impact. The impact can cause the production of microscopic, isolated neutral species at high temperature, due to disequilibrium deformation and sharp, localized increases in irreversible energy. Large temperature gradients and the presence of many microscopic fragments of the target and impactor could allow neutral species to form and become isolated within the magma ocean as it equilibrates. *Ringwood and Hibberson* [1991] noted that a large impact may cause large temperature and pressure gradients within the earth. These gradients may not be reduced on the same time scale as core formation. Thus

Data from Schmitt *et al.*, 1989

1300°C

logfO$_2$	D$_{(SM/LS)}$
-11.3	4.1 - 3.6
-12.0	7.3 - 7.5
-13.29	29.6 - 28.3

This Study

1400 – 1700°C

logfO$_2$	D$_{(LM/LS)}$
∼-17	52.9

Table 2.5: Partition coefficients for liquid Fe/ liquid MORB

shock-induced fragmentation and disequilibrium may allow microscopic, metallized particles to remain in the upper mantle after the core has formed. It is also possible that because of the large temperature and pressure gradients, it is hard to model the temperature and pressure-dependence of the siderophile elements. If the equilibrium occurred in local domains between the local liquid composition and metal particles as the core formed, the temperatures might vary a great deal, making isothermal models of siderophile partitioning inadequate.

Finally, the extreme reduction in our samples may help explain the origin of very small ($< 0.1\mu$m) Fe particles (in either single-domain or superparamagnetic state)

found in lunar soils. The majority of this fine-grain Fe is found in agglutinates (i.e., welded fragments of impact melts, *Heiken et al.,* 1991). *Pearce et al.* [1973] have approximated the total amount of Fe metal that should be present in the lunar soil by adding up the indigenous and potential meteoritic sources of Fe and they find that the actual measured amount of Fe in lunar samples is greater than their calculated amount. Various workers have tried to explain this apparent Fe excess by invoking different reduction mechanisms to obtain more Fe metal from either the impactor and/or target, including solar wind reduction of disseminated target or impactor [*Housley et al.,* 1973; *Hapke et al.,* 1975], shock-induced subsolidus reduction [*Cisowski et al.,* 1973], shock-induced reduction of impact melts [*Pearce et al.,* 1972] or shock-induced comminution of metallic Fe from the impactor [*Gibbons et al.,* 1975]. Although our results cannot address the viability of all these mechanisms and thus we cannot determine the exact oxidation-reduction reaction, we can address the plausibility of some of these possibilities. As discussed earlier, the efficient Fe reduction in our recovered fragments probably occurs while the phases are molten and thus subsolidus reduction is not a significant process. *Gibbons et al.* [1975] argued against shock reduction as a viable mechanism based on shock experiments. The usual stainless steel sample holder was replaced by a Cu container, so any Fe spherules that formed in the sample (bronzite, En_{86}) must come from reduction of Fe in the sample rather than the stainless steel container. The recovered sample contained Cu spherules but no Fe spherules, leading the authors to conclude that Fe in the bronzite was not shock reduced. In our shock experiments, the container is Mo so any Fe in the recovered sample must come from reduction of FeO in the sample.

Although we did not observe any isolated, pure Fe metal particles, there were some relatively small, Fe-Si-rich spheres with minor Mo formed by shock-induced reduction of the molten mixture. Therefore shock-induced reduction of impact melt should be considered a viable mechanism until further experiments can address this issue more quantitatively. The presence of Mo in the shocked melt complicates our analysis and indicates that reduction may occur in the impact melt due to fractionation and mixing. Clearly our experiments and *Gibbon et al.'s* [1975] experiments show that oxidation-reduction reactions are dependent on the composition of the metal container and sample. The possibility of shock-induced fractionation of the meteoritic metal cannot be addressed by our experiments since Fe was only present in the sample. However, the intimate mixing of the Mo from the impactor indicates that metal from the meteorite is likely to influence the final quench products.

2.6   Conclusions

Liquid metal–liquid silicate interactions are observed in impact experiments in which a molten silicate (MORB) has been in contact with a siderophile element (Mo). The recovered shocked glass shows important changes in major element chemistry with the most significant change being a systematic decrease in the FeO content as a function of increasing pressure from initially 9 wt% at zero pressure to 0.1 wt% at 6 GPa pressure in the shocked liquid. The other intriguing textural and chemical change is the formation of metallic spheres enriched in Fe, Mo and Si in the sample recovered from a MORB shock pressure of ~2.8 GPa.

The scenario we envisage for sphere formation is as follows: After impact, FeO

and SiO_2 in the superheated MORB liquid (1400 - 1700°C) are reduced to Fe and Si respectively in a very reducing atmosphere ($\sim 10^{-17}$ bars) formed either by incongruent vaporization of oxygen into the evacuated gun tank or in the formation of Mo-oxides that are quickly volatilized. The Fe and Si react and combine with micron-size ejecta of Mo as the metal droplets turbulently flow through the shocked liquid. Upon cooling (<140°C/s) the metallic phases may coalesce into larger globules within the shocked liquid.

The globular textures of our slowly cooled spheres are similar to the textures found in metallic particles from lunar rocks and soils, meteorites (*e.g.*, Canyon Diablo meteorite *Blau et al.*, [1973]) and some chondrites (e.g., Ramsdorf *Begemann and Wlotzka*, [1969]). These similarities may be used to compare and understand the evolution of these metallic particles from impact processes. Our observations imply that the majority (60%) of lunar metallic spheres with globular textures require some silicate insulator and may have had time to react and mix with the silicate liquid.

The substantial reduction and efficient segregation of the metal-silicate liquids has important implications for impact-produced chemical changes in the earth and moon. The origin of isolated, sub-microscopic Fe particles in lunar soils may be related to the origin of our Fe-rich spheres. The significant reduction of FeO in the shocked glass may occur by shock reduction, shock melting and/or fragmentation and mixing of the target and impactor. These oxidation-reduction mechanisms should be considered viable options for the production of the lunar Fe particles until further work is done.

On a larger scale, the implied kinetics of these reactions before the system

achieved equilibrium is also a relevant condition that has been neglected in giant impact models. Most models start with some isothermal, equilibrated system and use partition coefficients determined at one temperature from static, controlled experiments. The real system is likely to have significant initial thermal gradients, rapid, turbulent motion, changes in oxygen fugacity and faster reaction rates. These effects will be important for determining how the equilibrated system should be approached. It is possible that the impact produced very small isolated siderophile rich particles that did not have enough time to equilibrate and remained in suspension in the magma ocean. These particles might remain in the upper mantle and account for the siderophile excess in the present day earth. Furthermore, if these particles were present in the magma ocean as neutral species then *Murthy's* [1991] high temperature partition coefficient extrapolations may be appropriate since he assumes no dependence on the oxygen fugacity. Given the renewed interest in giant impacts as viable mechanisms for producing the earth's Fe-rich core and for the origin of the moon, continued study of impact-induced metal-silicate interactions may be helpful for testing dynamic models.

Bibliography

Asphaug, E., H. J. Melosh, and E. Ryan, A numerical laboratory for fragmentation studies: Some insights into collisional processes and outcomes (abstract), in *Lunar and Planetary Science XXII*, pp. 37 - 38, Lunar and Planetary Institute, Houston, 1991.

Badjukov, D. D., and T. L. Petrova, Shock induced interaction between metal iron and silicates (abstract), in *Lunar and Planetary Science XXII*, pp. 41 - 42, Lunar and Planetary Institute, Houston, 1991.

Begemann, F., and F. Wlotzka, Shock induced thermal metamorphism and mechanical deformations in the Ramsdorf Chondrite, *Geochim. Cosmochim. Acta, 33*, 1351 - 1370, 1969.

Blau, P. J., H. J. Axon, and J. I. Goldstein, Investigation of the Canyon Diablo metallic spheroids and their relationship to the breakup of the Canyon Diablo Meteorite, *J. Geophys. Res., 78*, 363 - 374, 1973.

Blau, P. J., and J. I. Goldstein, Investigation and simulation of metallic spherules from lunar soils, *Geochim. Cosmochim. Acta, 39*, 305 - 324, 1975.

Brett, R., Metallic spherules in impactite and tektite glasses, *Am. Mineral., 52*, 721-733, 1967.

Bunch, T. E., and W. A. Cassidy, Impact induced deformation in the Campo del Cielo meteorite, in *Shock Metamorphism of Natural Materials*, edited by B. M. French and N. M. Short, pp. 601-612, 1968.

Cameron, A. G. W., and W. R. Ward, The origin of the moon (abstract), in *Lunar and Planetary Science VII*, pp. 120 - 122, The Lunar Science Institute, Houston, 1976.

Carter, J. L., and I. D. MacGregor, Mineralogy, petrology and surface features of some Apollo 11 samples, *Proc. Apollo 11 Lunar Sci. Conf., Geochim Cosmochim. Acta Suppl. 1, 1*, 247-265, 1970.

Cisowski, C. S., M. Fuller, M. E. Rose, and P. J. Wasilewski, Magnetic effects of experimental shocking of lunar soils, *Proc. Lunar Sci. Conf. 4th*, 3003-3017, 1973.

Colson, R. O., Solubility of neutral nickel in silicate melts and implications for the Earth's siderophile element budget, *Nature, 357*, 65-68, 1992.

Deamer, G. H., and J. I. Goldstein, Experimental study of shock melted metallic particles (abstract), in *Lunar and Planetary Science XI*, pp. 198 - 200, Lunar and Planetary Institute, Houston, 1980.

Delaney, J. R., H. P. Johnson, and J. L. Karsten, The Juan de Fuca Ridge - Hot-Spot - propagating rift system: New tectonic, geochemical, and magnetic data, *J. Geophys. Res., 86*, 11,747 - 11750, 1981.

Essene, E. J., and D. C. Fisher, Lightning strike fusion: Extreme reduction and metal-silicate liquid immiscibility, *Science, 234*, 189-193, 1986.

Gibbons, R. V., and T. J. Ahrens, Shock metamorphism of silicate glasses, *J. Geophys. Res., 76*, [23], 5489-5498, 1971.

Gibbons, R. V., R. V. Morris, F. Horz, and T. D. Thompson, Petrographic and ferromagnetic resonance studies of experimentally shocked regolith analogs, *Proc. Lunar Planet. Sci. Conf. 6th*, 3143-3171, 1975.

Goarant, F., F. Guyot, J. Peyronneau, and J. P. Poirier, High-pressure and high-temperature reactions between silicates and liquid iron alloys, in the diamond anvil cell, studied by analytical electron microscopy, *J. Geophys. Res., 97*, [B4], 4477-4487, 1992.

Goldstein, J. I., E. P. Henderson, and H. Yakowitz, Investigation of lunar metal particles, in *Proc. Apollo 11 Lunar Sci. Conf.*, vol. 1, Mineralogy and Petrology, pp. 499 - 512, Pergamon, Houston, 1970.

Gray, M. L., C. R. Abermathy, R. Caruso, A. S. Jordan, and J. J.M. Parsey, Surface polygonization on GaAs wafers, *J. Appl. Phys., 64*, [3], 1468-1471, 1988.

Grieve, R. A. F., Terrestrial impact: The record in the rocks, *Meteoritics, 26*, 175-194, 1991.

Grieve, R. A. F., H. Palme, and A. G. Plant, Siderophile-rich particles in the melt rocks at the E. Clearwater Impact Structure, Quebec: Their Characteristics and Relationships to the Impacting Body, *Contrib. Mineral. Petrol.*, *75*, 187-198, 1980.

Gubbels, G. H. M., Interfaces in composites of alumina in a molybdenum matrix, *Mater. Sci. Eng.*, *A135*, 135-139, 1991.

Hapke, B., W. Cassidy, and E. Wells, Effects of vapor-phase deposition processes on the optical, chemical, and magnetic properties of the lunar regolith, *The Moon*, *13*, 339-353, 1975.

Hartmann, W. K., and D. R. Davis, Satellite-sized planetesimals and lunar origin, *Icarus*, *24*, 504 - 515, 1975.

Heiken, G. H., D. T. Vaniman, and B. M. French (Ed.), *Lunar Sourcebook, a User's Guide to the Moon*, pp. 1-736, Cambridge Univ. Press, Cambridge, 1991.

Hörz, F., T. H. See, A. V. Murali, and D. P. Blanchard, Heterogeneous dissemination of projectile materials in the impact melts from Wabar Crater, Saudi Arabia, *Proc. Lunar Planet. Sci. Conf. 19th*, 697-709, 1989.

Housley, R. M., R. W. Grant, and N. E. Paton, Origin and characteristics of excess Fe metal in lunar glass welded aggregates, *Proc. Lunar Sci. Conf. 4th*, 2737-2749, 1973.

Kelly, W. R., E. Holdsworth, and C. B. Moore, The chemical composition of metallic spheroids and metallic particles within impactites from Barringer Meteor Crater, Arizona, *Geochim. Cosmochim. Acta*, *38*, 533-543, 1974.

King, E. A., Reduction, partial evaporation, and spattering: Possible chemical and physical processes in fluid drop chondrule formation, in *Chondrules and their Origins*, edited by E. A. King, pp. 180-187, Lunar and Planetary Institute, Houston, 1983.

Knittle, E., and R. Jeanloz, Simulating the core-mantle boundary: An experimental study of high-pressure reactions between silicates and liquid iron, *Geophys. Res. Let.*, *16*, [7], 609-612, 1989.

Lange, R. A., and I. S. E. Carmichael, Densities of Na_2O-K_2O-CaO-MgO-FeO-Fe_2O_3-Al_2O_3 -TiO_2 -SiO_2 liquids: New measurements and derived partial molar properties, *Geochim. Cosmochim. Acta*, *51*, 2931 - 2946, 1987.

Mehta, S., and J. I. Goldstein, Metallic particles in the glass of lunar highland samples 65315, 67435 and 78235 (abstract), in *Lunar and Planetary Science XI*, pp. 720 - 722, Lunar and Planetary Institute, Houston, 1980.

Melosh, H. J., *Impact Cratering, A Geologic Process*, Oxford University Press, New York, 1-245, 1989.

Miller, G., E. M. Stolper, and T. J. Ahrens, The equation of state of a molten komatiite I: Shock wave compression to 36 GPa, *J. Geophys. Res.*, 1991.

Mittlefehldt, D. W., T. H. See, and F. Horz, Projectile dissemination in impact melts from Meteor Crater, Arizona, in *Lunar Planet. Sci. Conf. XXIII*, pp. 919-920, Lunar and Planetary Institute, Houston, 1992.

Murthy, V. R., Early differentiation of the Earth and the problem of mantle siderophile elements: A new approach, *Science, 253*, 303 - 306, 1991.

Newsom, H. E., and K. W. W. Simms, Core formation during early accretion of the Earth, *Science, 252*, 926-933, 1991.

O'Neill, H. S. C., The origin of the Moon and the early history of the Earth – A chemical model. Part 1: The Moon, *Geochim. Cosmochim. Acta, 55*, 1135-1157, 1991a.

O'Neill, H. S. C., The origin of the Moon and the early history of the Earth – A chemical model. Part 2: The Earth, *Geochim. Cosmochim. Acta, 55*, 1159-1172, 1991b.

Pearce, G. W., W. A. Gose, and D. W. Strangway, Magnetic studies on Apollo 15 and 16 lunar samples, *Proc. Lunar Sci. Conf. 4th*, 3045-3076, 1973.

Pearce, G. W., R. J. Williams, and D. S. McKay, The magnetic properties and morphology of metallic iron produced by subsolidus reduction of synthetic Apollo 11 composition glasses, *Earth Planet. Sci. Let., 17*, 95-104, 1972.

Raynor, G. V., and V. G. Rivlin, Critical evaluation of constitution of iron-molybdenum-silicon alloys, in *Phase Equilibria in Iron Ternary Alloys* , p. 398-413, Institute of Metals, London, 1988.

Reimold, W. U., and D. Stoffler, Experimental shock metamorphism of dunite, *Proc. Lunar Planet. Sci. Conf. 9th*, 2805-2824, 1968.

Rigden, S. M., T. J. Ahrens, and E. M. Stolper, Shock compression of molten silicate: Results for a model basaltic composition, *J. Geophys. Res., 93*, 367-382, 1988.

Ringwood, A. E., and W. Hibberson, Solubilities of mantle oxides in molten iron at high pressures and temperatures: implications for the composition and formation of Earth's core, *Earth Planet. Sci. Let.*, *102*, 235-251, 1991.

Robie, R. A., B. S. Hemingway, and J. S. Fisher, Thermodynamic properties of minerals and related substances at 298.15 K and 1 bar (105 Pascals) pressure and at higher temperatures, *U. S. Geol. Surv. Bull.*, *1452*, 163,201,217, 1978.

Scarlett, B., and R. E. Buxton, Particle size distribution of spherical particles in Apollo 12 samples, *Earth Planet. Sci. Lett.*, *22*, 177-187, 1974.

Schaal, R. B., Disequilibrium features in experimentally shocked mixtures of olivine plus silica glass powders, *Contrib. Mineral. Petrol.*, *81*, 39-47, 1982.

Schaal, R. B., and F. Horz, Experimental shock metamorphism of lunar soil, *Proc. Lunar Planet. Sci. Conf. 11th*, 1679 - 1695, 1980.

Schaal, R. B., F. Horz, T. D. Thompson, and J. F. Bauer, Shock metamorphism of granulated lunar basalt, *Proc. Lunar Planet. Sci. Conf. 10th*, 2547-2571, 1979.

Schmitt, W., H. Palme, and H. Wanke, Experimental determination of metal/silicate partition coefficients for P, Co, Ni, Cu, Ga, Ge, Mo, and W and some implications for the early evolution of the Earth, *Geochim. Cosmochim. Acta*, *53*, 173 - 185, 1989.

Schuster, J. C., and H. Ipser, The $Al-Al_8Mo_3$ section of the binary system aluminum-molybdenum, *Metall. Trans. A*, *22A*, 1729-1736, 1991.

Scott, E. R. D., Origin of rapidly solidified metal-troilite grains in chondrites and iron meteorites, *Geochim. Cosmochim. Acta*, *46*, 813 - 823, 1982.

Seifert, S., H. S. C. O'Neill, and G. Brey, The partitioning of Fe, Ni and Co between olivine, metal, and basaltic liquid: An experimental and thermodynamic investigation, with application to the composition of the lunar core, *Geochim. Cosmochim. Acta*, *52*, 603-616, 1988.

Spencer, L., Meteoritic iron and silica glass from the meteorite craters of Henbury (Central Australia) and Wabar (Arabia), *Mineral Mag.*, *23*, 387-404, 1933.

Stebbins, J. F., I. S. E. Carmichael, and L. K. Moret, Heat capacities and entropies of silicate liquids and glasses, *Contrib. Mineral. Petrol.*, *86*, 131 - 148, 1984.

Stevenson, D. J., Fluid dynamics of core formation, in *Origin of the Earth*, edited by H. E. Newsom and J. H. Jones, pp. 231 - 249, Oxford Univ. Press, New York, 1990.

Taylor, G. J., and D. Heymann, Postshock thermal histories of reheated chondrites, *J. Geophys. Res.*, *76*, 1897 - 1893, 1971.

Taylor, S., and D. E. Brownlee, Cosmic spherules in the geologic record, *Meteoritics*, *26*, 203-211, 1991.

Tonks, W. B., and H. J. Melosh, Core formation by giant impacts (abstract), in *Lunar and Planetary Science XXII*, pp. 1405 - 1406, Lunar and Planetary Institute, Houston, 1991.

Unal, O., J. J. Petrovic, D. H. Carter, and T. E. Mitchell, Dislocations and plastic deformation in molybdenum disilicide, *J. Am. Ceram. Soc.*, *73*, [6], 1752-1757, 1990.

Wanke, H., F. Wlotzka, E. Jagoutz, and F. Begemann, Composition and structure of metallic iron particles in lunar "fines", in *Proc. Apollo 11 Lunar Sci. Conf.*, vol. 1, Mineralogy and Petrology, pp. 931 - 936, Pergamon, Houston, 1970.

Yu, L., M. A. Meyers, and K. S. Vecchio, Shock synthesis of silicides: Microstructures and mechanisms, in *Proc. Int. Symp. on Intense Dynamic Loading and its Effects*, pp. 741-748, China, 1992.

Zaitsev, A. I., M. A. Zemchenko, and B. M. Mogutnov, Thermodynamic properties of (1-x)Si + xFe), *J. Chem. Thermo.*, *23*, 831-849, 1992.

Chapter 3

Three-Dimensional Structure of Kilauea Volcano

A linear, travel time tomography study of the most active shield volcano of the world, Kilauea Volcano, Hawaii, was undertaken to determine the lateral heterogeneities produced by its intricate magmatic and tectonic environment. Kilauea provides an ideal setting to do tomography because of its dense seismograph array and many local earthquakes that allow excellent ray coverage of complex subsurface features. Local P wave data from $\sim$12,295 events were inverted using a one-dimensional layered velocity model. Inversions were done for two cell sizes ($5 \times 5 \times 5$ km and $1 \times 1 \times 1$ km) to resolve structural regions on different length scales. This study provided a view of the average velocity variations relative to a one-dimensional velocity model. Analysis and interpretation of the tomographic images allowed us to infer the following model. The main shallow magma reservoir is delineated by a slow velocity region southeast of the summit from 0 to 2 km depth. There is a distinct high velocity region centered

northwest of the summit from 0 to 2 km depth that represents a cap of dense, intrusive dikes surrounding the magma chamber. We suggest that the shallow reservoir is a narrow, compartmentalized region of sills and dikes, centered just south-southeast of Halemaumau caldera. Below the main reservoir, the summit is imaged as a slightly fast region from 5 to 10 km in the coarse model indicating that the main conduit is structurally defined by an intrusive dike complex until about 10 km. The rift zones of Kilauea are imaged as major, high velocity entities, widening to the south with depth until 6 km. These fast anomalies are related to the sheeted dike complexes along the rifts. On a finer scale, slow anomalies suggest the presence of magma pockets centered at 0–2 km depth beneath Mauna Ulu, Makaopuhi and Puu Oo, along the east rift zone (ERZ). Two significant high velocity regions along the lower ERZ near Kalalua and Kaliu are inferred to represent intrusive barriers to magma injection along the shallow (0–4 km) ERZ conduit. The southwest rift zone may have an intrusive barrier related to a high velocity region just southwest of Mauna Iki. The Hilina and Kaoiki fault zones are imaged as slow features at shallow depths (< 5 km) related to the open fractures and scarps along the normal faults. The Koae fault system is imaged as a slightly fast shallow structure (< 6 km) possibly related to intrusive diking from the adjacent rift zones that fill and may even induce the extensional structures associated with this complex fault zone. Continued inversions with the immense amount of seismic data collected for Hawaiian events will allow the detailed development of a three-dimensional structural model for Kilauea. Such a model will be extremely useful to seismologists and petrologists alike for understanding the tectonic growth and magmatic evolution of this dynamic shield volcano.

3.1   Introduction

Kilauea is the youngest, most historically active shield volcano of the Hawaiian -
Emperor Volcanic Chain. Located on the southeastern coast of the Island of Hawaii
(Figure 3.1), its subtle relief represents the southernmost subaerial volcano created
by the hotspot swell beneath the island. Kilauea's isolation from continental crustal
structure and contamination, as an intraplate, oceanic volcano, and its relation to
hotspot theory make it one of the most intensely studied volcanoes of the world.
Its accessibility, relative simplicity compared to interplate boundaries and the large
amount of data obtained through years of study, make Kilauea the most logical and
feasible volcano to attempt to model in three dimensions. Our goal is to provide a
detailed image of the lateral and vertical velocity heterogeneities of Kilauea that can
be used to infer its magmatic structure. Such insight may improve our understanding
of other processes such as hotspot dynamics, magma genesis and propagation, magma
chamber structure, fault structure mechanisms and dike formation and propagation.

3.1.1   Surface Structure

Kilauea is a broad, subtle shield volcano rising to a summit elevation of about 1.24
km and covering about 1500 km^2 (Figure 3.1). There are six prominent structural
provinces, the summit caldera, two rift zones and three fault systems (Figure 3.2) that
have been defined and studied by various workers [e.g., *Swanson et al.,* 1976]. We
have organized and concentrated our study on extending the structural interpretation
of these surface features into the shallow subsurface ($\sim$20 km).

The southwest rift zone (SWRZ) and east rift zone (ERZ) extend from the summit

Figure 3.1: Topographic map of the Island of Hawaii showing the five volcanoes and the seismographic array. Each station is labeled by a triangle except for two stations that are on other islands. The two solid triangles are stations on which we centered the caldera symbols in our model images. The large and small rectangles show the areal extent of the coarse and fine model, respectively, used for the inversion.

ISLAND OF HAWAII

Kohala

Mauna Kea

Hualalai

MAUNA LOA

KILAUEA

Fine

Coarse

0   15   30 km

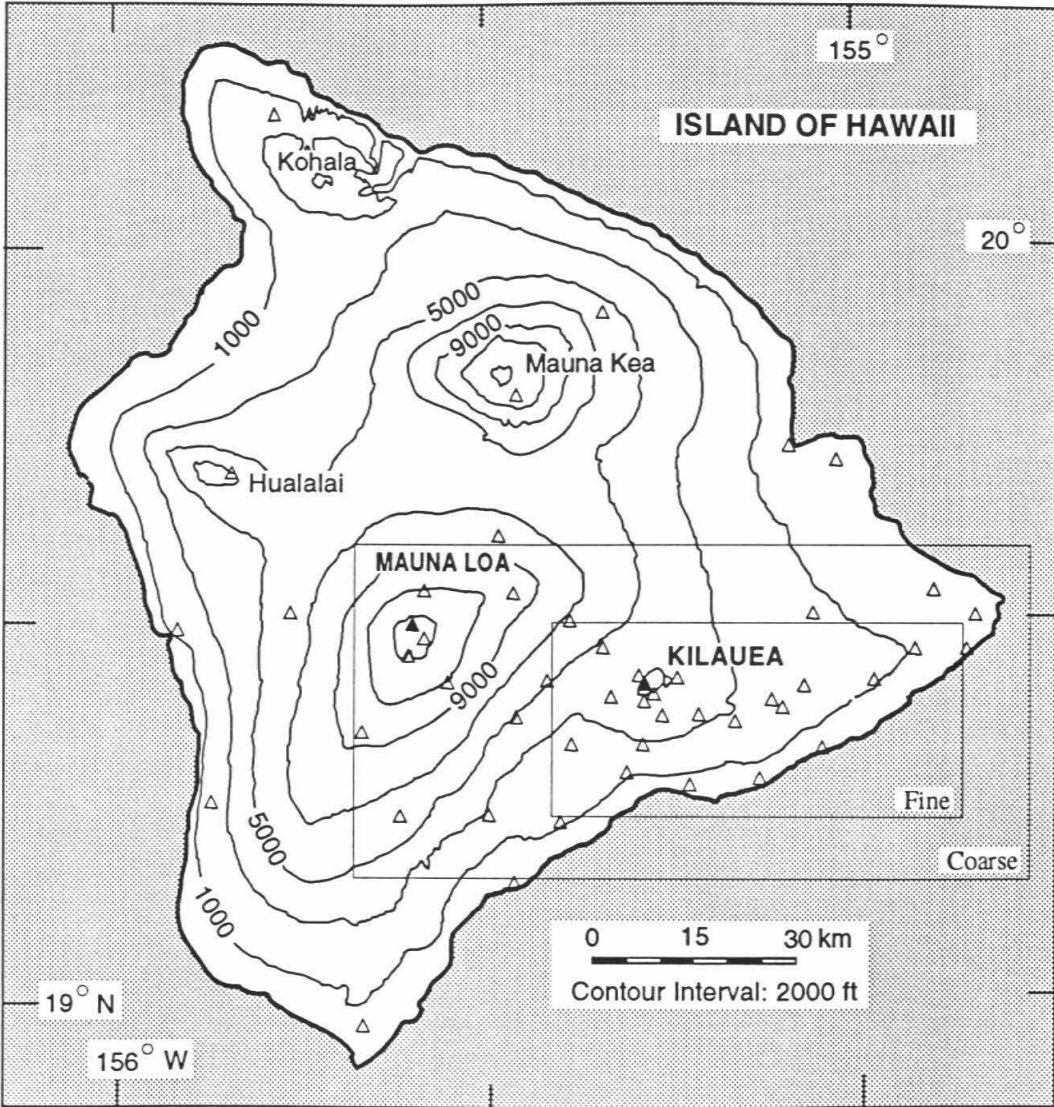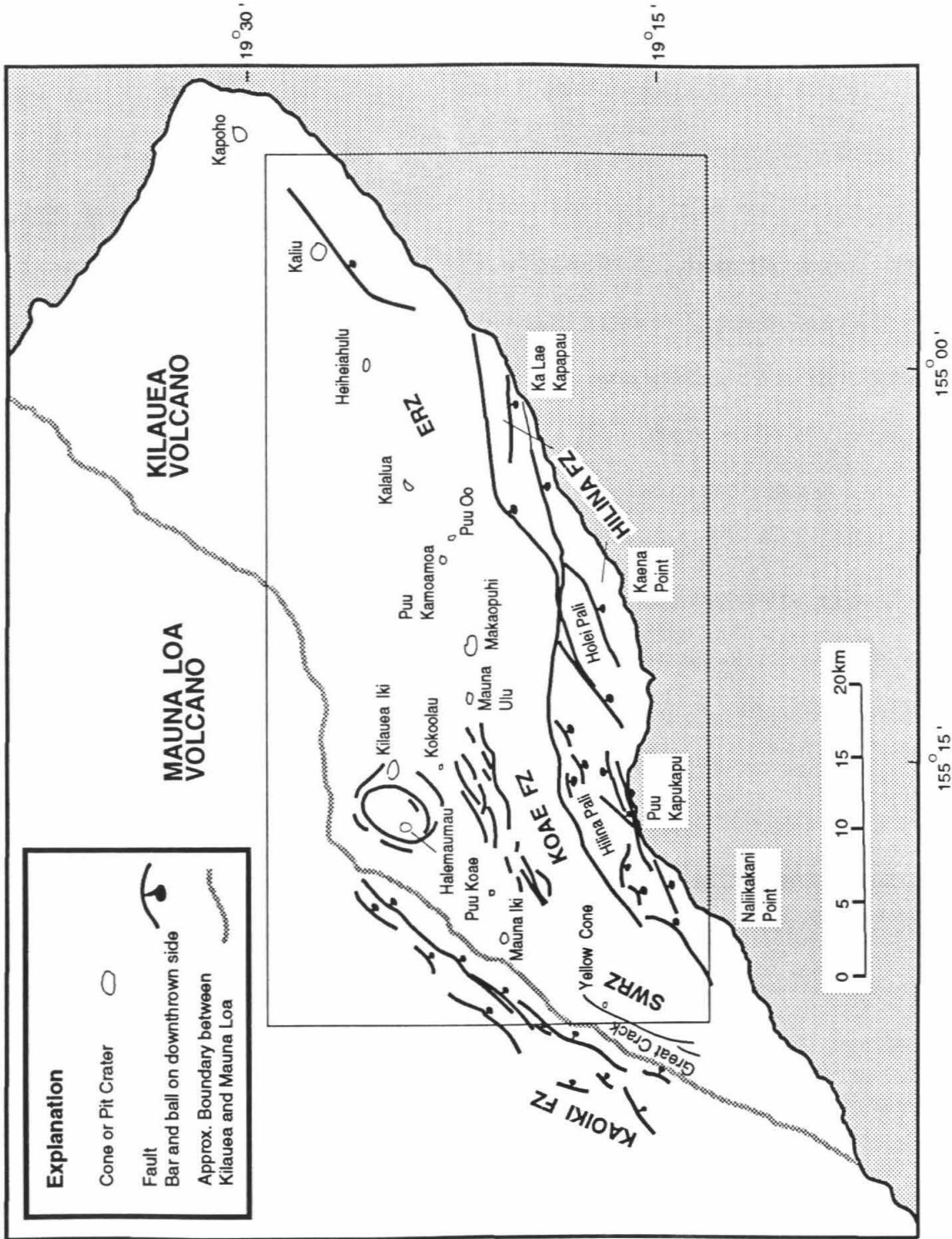Contour Interval: 2000 ft

155°

20°

19° N

156° W

Figure 3.2: Map of Kilauea Volcano and the adjacent part of Mauna Loa Volcano covered by the coarse model. Important structural regions (i.e., fault traces, cones and craters). discussed in this paper are marked. The areal extent of the fine model is shown by the smaller rectangle. Map modified from *Swanson et al.* [1976].

Explanation

Cone or Pit Crater

Fault
Bar and ball on downthrown side

Approx. Boundary between
Kilauea and Mauna Loa

KILAUEA
VOLCANO

MAUNA LOA
VOLCANO

Kapoho

Kaliu

Heiheiahulu

ERZ

Kalalua

Puu Oo

Puu
Kamoamoa

Makaopuhi

Mauna
Ulu

Kilauea Iki

Kokoolau

Halemaumau

Puu Koae

Mauna Iki

Yellow Cone

Great Crack

Ka Lae
Kapapau

HILINA FZ

Kaena
Point

Holei Pali

Hilina Pali

Puu
Kapukapu

Naliikakani
Point

KOAE FZ

SWRZ

KAOIKI FZ

19°30'

19°15'

155°00'

155°15'

0   5   10   15   20km

as subtle constructional ridges. They are delineated along their crests by cones, craters and fissures and are the source of almost all non-summit eruptions. The rift zones separate Kilauea into a stable north flank, buttressed by Mauna Loa, and a mobile south flank, which extends into the ocean. The subaerial ERZ is 60 km long, 4–6 km wide and has been divided into three segments. The upper segment (from Halemaumau Caldera to Makaopuhi Crater) is separated from the middle segment (from Makaopuhi to Heiheiahulu) and the lower segment (from Heiheiahulu to the coast) by a significant bend in the rift that has been attributed to the southward migration of the south flank [*Kinoshita et al.*, 1963; *Swanson et al.*, 1976]. The SWRZ extends approximately 30 km southwest from the summit and is a maximum of about 4 km wide on the surface. Unlike the ERZ, it does not form a well-defined constructional ridge and has fewer intrusions and eruptions than the ERZ [*Duffield et al.*, 1982]. The lack of volcanic activity and morphological development of the SWRZ is due to its more direct and significant buttressing by Mauna Loa [*Duffield et al.*, 1982; *Fornari*, 1987; *Casadevall and Dzurisin*, 1987; *Thurber and Gripp*, 1988].

The Koae fault system, a 12 km long and 3 km wide zone of scarps and fractures south of the summit, obliquely intersects both rift zones. Together with the rift zones it separates the mobile south flank from the summit of Kilauea. Most of the Koae consists of east-northeast striking normal faults that form asymmetric grabens with steep, north-facing scarps. Several workers have described the Koae as a passive tear away zone that is being moved southward as a hinge between the two rift zones by intrusion of magma into the rifts [*Duffield*, 1975; *Swanson et al.*, 1976].

The Hilina and Kaoiki are two other important fault zones, that affect the growth

of the shield volcano. The Hilina fault system, located along the southern coast of the island, is a series of normal faults with south-facing scarps. These structures are controlled by gravity and sliding of the south flank seaward [*Swanson et al.*, 1976; *Crosson and Endo*, 1982; *Dvorak et al.*, 1986; *Eissler and Kanamori*, 1987; *Thurber and Gripp*, 1988]. The Kaoiki fault system parallels the SWRZ and consists of normal faults with south-facing scarps. This fault zone is part of Mauna Loa Volcano and may have served the same structural function for Mauna Loa that the Hilina system now serves for Kilauea [*Koyanagi et al.*, 1966]. We include the Kaoiki in our discussion of Kilauea because of its proximity to Kilauea and because it is currently the most seismically active fault zone on Hawaii.

3.1.2 Previous Studies

Early models of the summit magma reservoir are based mainly on geodetic data [*Eaton*, 1962; *Dieterich and Decker*, 1975; *Swanson et al.*, 1976; *Duffield et al.*, 1982; *Dvorak et al.*, 1983]. Several of these studies noted that the transient features of ground deformations makes it hard to determine the exact depth of the reservoir. These complex ground motions indicate a complex magma chamber consisting of sills and dikes over a 3 km wide area [*Fiske and Kinoshita* 1969; *Duffield et al.* 1982]. *Yang et al.* [1992] eliminated the transient features found during many inflationary periods at Kilauea's summit from 1970–1985 by introducing dike intrusion as a secondary mechanism for ground motions. If the dike intrusion-related deformations are excluded from the geodetic data, a single magma reservoir at ~2.6 km depth, centered 2 km southeast of Halemaumau is obtained.

The complexity of the magma reservoir, as indicated by the geodetic studies, is

one of the main reasons no one has imaged a large, obvious reservoir beneath the summit in previous three-dimensional seismic models [*Ellsworth and Koyanagi*, 1977; *Crosson and Koyanagi*, 1979; *Ryan et al.*, 1981; *Klein et al.*, 1987]. *Ellsworth and Koyanagi* [1977] and *Crosson and Koyanagi* [1979] inverted teleseismic and local P waves, respectively, and imaged high velocity features beneath the summit related to intrusive structures. *Ryan et al.* [1981] used accurately determined hypocenters to infer the intrusive outline of the magma chamber, notably a roof at 1.1–1.9 km depth, a floor at 5.7–6.5 km depth and an aseismic zone at 2–6 km depth inferred to be the shallow reservoir. More recent three-dimensional inversions have imaged some small, low velocity zones at different depths beneath Halemaumau [*Thurber*, 1984, 1987; P. Ho-Liu et al., preprint, 1991]. Thus the main shallow magma reservoir is inferred from models of ground deformation, an aseismic gap, patterns of high velocity intrusives that form the skeletal framework of the reservoir and some small, low velocity features. These observations or models do not necessarily require a large, homogeneous magma chamber.

Previous velocity models have been more successful at delineating Kilauea's rift zones than finding a shallow magma reservoir. The rifts zones stand out as dominant high velocity features in many models [*Ellsworth and Koyanagi*, 1977; *Crosson and Koyanagi*, 1979; *Thurber*, 1984 and 1987; *Hill and Zucca*, 1987]. Hill and Zucca's cross sections (Figures 37.9 and 37.10), which summarize their refraction studies and *Kinoshita et al.*'s [1963] gravity survey, suggest triangular-shaped, tholeiitic, sheeted dike complexes that extend to a depth of at least 6 km. The widening with depth of the dense intrusives agrees with *Swanson et al.*'s [1976] model of volcanic growth

by the forceful intrusion of magma along the rift zones. *Klein et al.* [1987] and P. Ho-Liu et al. (preprint, 1991) have added to this model several distinct magma pockets along the rifts, including a small reservoir beneath the currently active Puu Oo eruption center. The magma is inferred to enter the ERZ through a complex pipe-shaped conduit that taps the lower part of the shallow summit magma reservoir [*Ryan et al.*, 1981; *Klein et al.*, 1987].

3.1.3 Our Approach

P wave travel times from local events on Kilauea and Mauna Loa recorded in 1986 were used to conduct a large-scale, linear tomographic inversion. For one set of inversions we used data from the Hawaiian Volcano Observatory (HVO) and for the second set of inversions we relocated these events using HYPOINVERSE [*Klein*, 1989]. Images produced using both data sets are presented to delineate robust anomalies that are not significantly effected by hypocenter mislocations or differences in parameters (i.e., station delays and weighting schemes) used by the location procedures. It is inappropriate to use our three-dimensional images to derive a three-dimensional velocity model, use this new model to relocate hypocenters and reinvert for new three-dimensional images because these images are ultimately dependent on the one-dimensional velocity model. A three-dimensional tomographic inversion would be more accurate and the resulting images more meaningful if an independently derived three-dimensional velocity model was used. Even with the important improvements in three-dimensional ray tracing, hypocenters are not fixed and ray paths are only approximate, making it difficult to describe the precise ray path taken around sharp velocity contrasts inferred to exist at Kilauea. A more accurate three-dimensional

velocity model may be obtained by doing a detailed refraction survey where source locations and ray paths are relatively well known.

Other problems common to tomographic inversions include appropriateness of the model space, influence of ray bending and nonuniform distribution of stations and/or sources. Our approach is to describe the data, the method and define and discuss the noise introduced into our images via errors in the data and/or method. Finally, we present the average three-dimensional velocity variations of Kilauea relative to the one-dimensional velocity model and our preferred structural interpretations of these anomalies.

3.2 Data Description

Hawaii is ideal for travel time tomography using local events because it has a dense seismograph array and abundant local seismicity, particularly around Kilauea. The array consists of 54 stations, of which, 42 were used for our inversions (Figure 3.1). Station coverage is more than adequate around Kilauea, although the network is somewhat unevenly spatially distributed with a higher density of stations on the summit and rift zones. P wave phase data from HVO for 12,295 local events in 1986 were used for the inversions. Most of the earthquakes were shallow (<15 km), small magnitude (<2.5) events directly related to magma movement and eruption episodes during the year. Figure 3.3a shows the distribution of hypocenters for the HVO data for one month. The general pattern of seismicity is representative of the pattern for the entire year's worth of data, so only these hypocenters are shown for clarity. The relocated hypocenters (Figure 3.3b) showed the same patterns, although the clusters

are tighter and the distribution of events with depth are different from the HVO
locations (see discussion in resolution and errors section).

Shallow events (<15 km) are concentrated along the Kaoiki fault system, Kilauea
summit, the upper ERZ and the south flank of Kilauea. The concentration between
Mauna Loa and Kilauea forms a very dense, north-south trending, linear zone from
5 to 15 km depth called the Kaoiki earthquake zone because this elongate cluster
of hypocenters trends along the right-lateral strike-slip fault plane solution of the
November 16, 1983, 6.6 magnitude Kaoiki earthquake (i.e., the aftershock zone).
Thus these earthquakes are more tectonic in nature, representing the continued stress
the dominant Mauna Loan edifice places on the smaller, very active Kilauea Volcano.
Kilauea's summit shows significant activity, in two clusters, on Halemaumau caldera
from 0 to 5 km depth. The eastern cluster has been attributed to the center of
summit deformation and does not extend below 5 km. The western cluster has not
been attributed to any specific physical process and may not be distinctly different
from the eastern cluster as will be discussed later. Events on the south flank are
concentrated from 0 to 10 km depth between the summit and Kalalua Cone, which
marks the eastern boundary of eruptive activity for Puu Oo. These earthquakes may
be correlated directly to stresses induced by magma intrusion and propagation along
the ERZ's current eruption site. It has also been suggested that the slightly more
dense cluster of earthquakes along the western end of the south flank concentration,
extending from just west of the bend in the ERZ southward to Puu Kapukapu, is
more highly stressed. This linear zone may represent a line of breakage between
different mobile blocks of the south flank [*Ryan*, 1988].

Figure 3.3: *a.* Plot of hypocenters from the original HVO data for events in January in 5-km depth slices within the coarse model. The number of events in each layer is marked on the top. Kilauea's rift zones are marked by the dashed lines. The southeastern coastline of Hawaii is marked by the solid line. Kilauea caldera, centered on station NPT, the north pit of Halemaumau, (Figure 3.1) is shown by the small caldera symbol. Mauna Loa caldera, centered on station MOK, Mokuaweoweo caldera (Figure 3.1), is shown by the larger caldera symbol. *b.* Plot of relocated hypocenters (determined using the standard layered velocity model, Figure 3.4, and the relocation program HYPOINVERSE [*Klein,* 1989]) for events in January in 5-km depth slices within the coarse model.
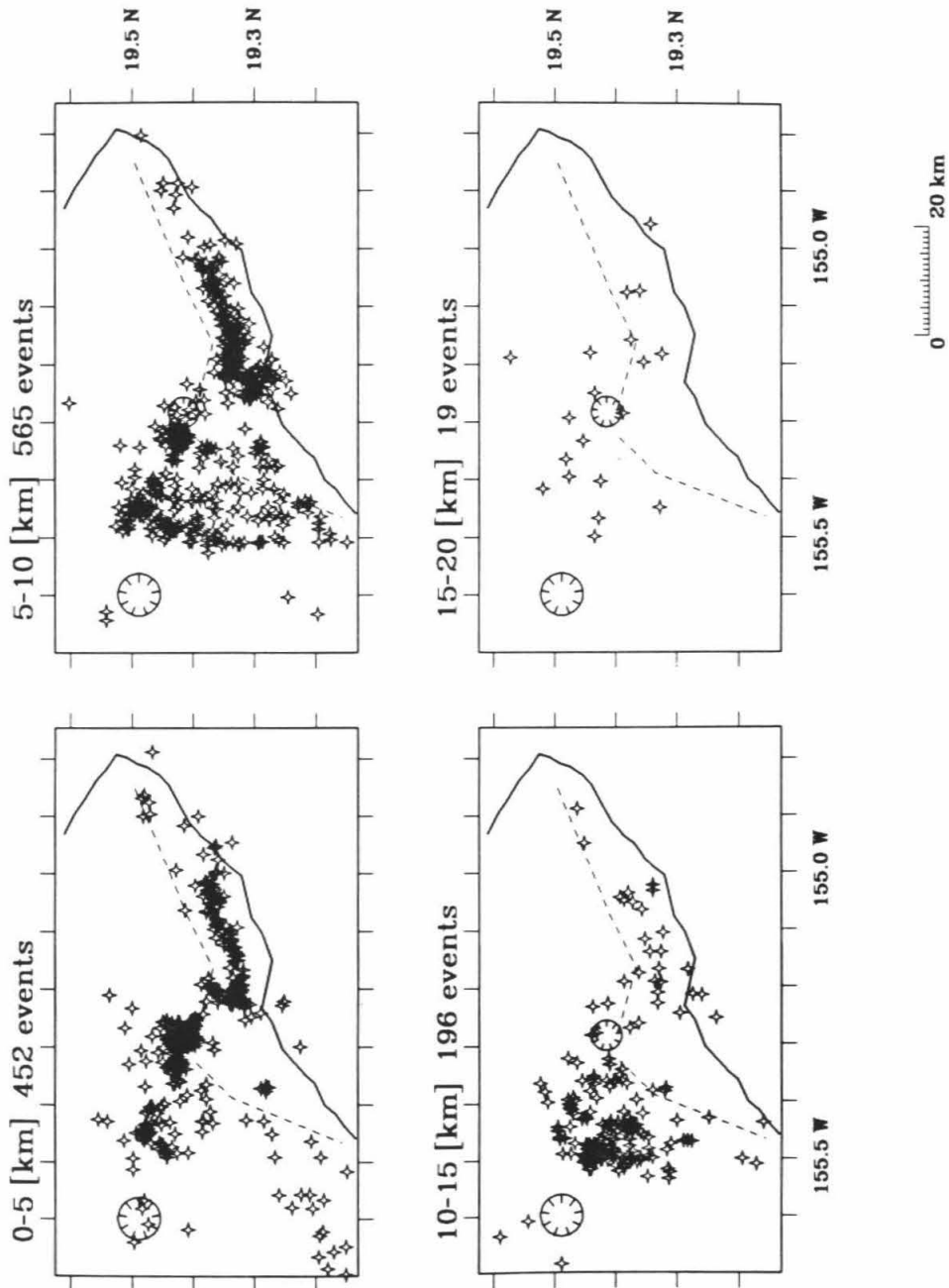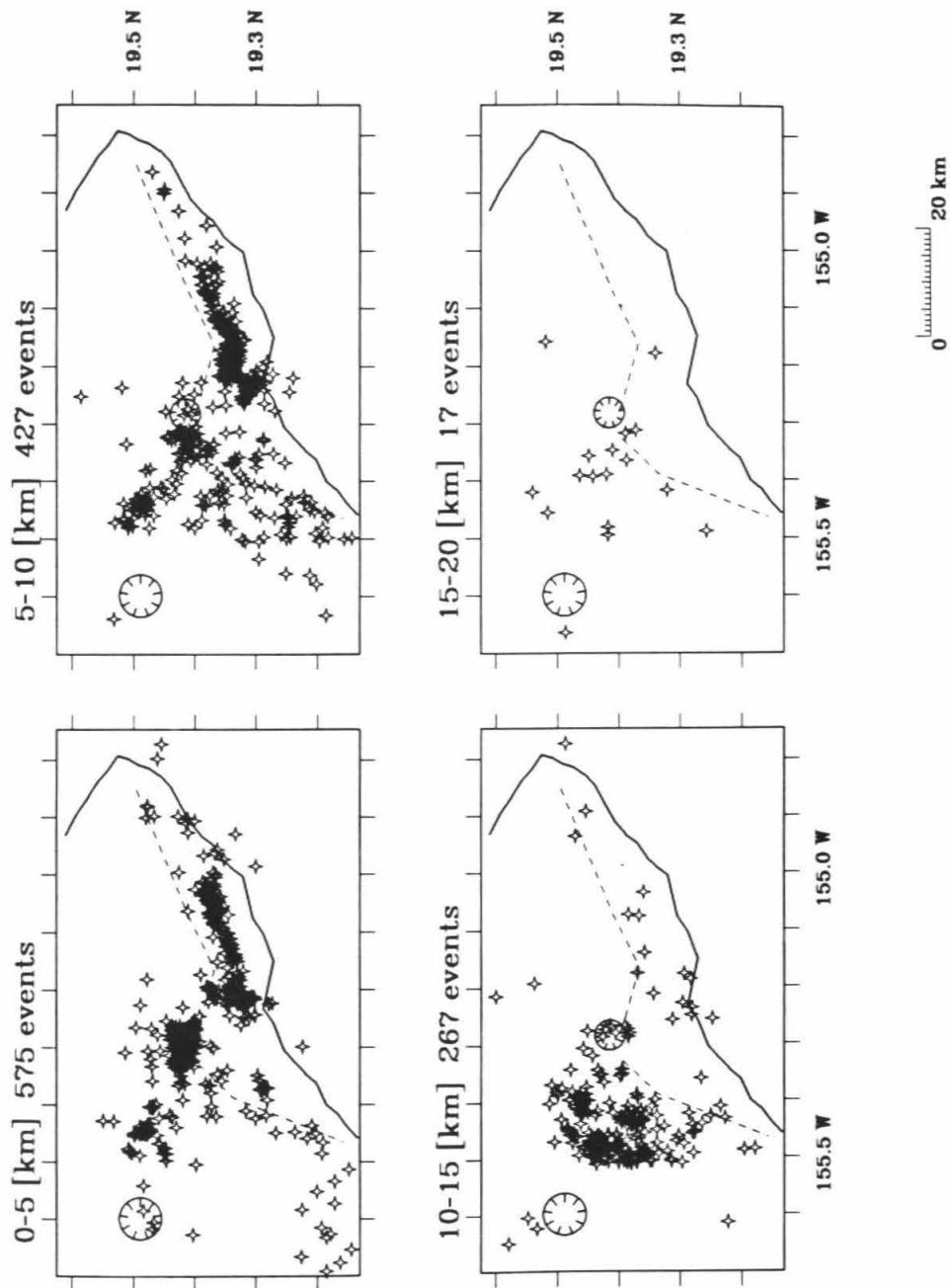
3.3   Method

Travel time tomography involves inverting a data set of travel time residuals ($\triangle t$) into a change of slowness ($\triangle s$) field, where slowness is the inverse of velocity. The initial travel time residual ($\triangle t^o$) is

$$\triangle t^o = TT^{obs} - TT^{raytr} \tag{3.1}$$

where TT^{raytr} is the calculated travel time determined by ray tracing. The velocity model used for the ray tracing is a one-dimensional, layered model modified from *Klein* [1981] (Figure 3.4) and is the same velocity model used by the HVO to locate earthquakes in 1986. TT^{obs} is the observed travel time computed from the data. For the HVO data, TT^{obs}, is the observed arrival time of the P wave minus the observed origin time of the event. This model uses the HVO data as if the hypocenters were fixed and does not correct for errors in location or origin time. For the relocated hypocenters, TT^{obs}, is the observed arrival time of the P wave minus the calculated origin time of the event. The origin time of the earthquake is adjusted during the relocation to provide the best fit to the picks [see *Klein*, 1989].

Discretization is accomplished by defining a model space of three-dimensional cells over a change of slowness field. Two models with different cell sizes (Figures 3.1 and 3.2) were chosen for the tomographic inversions. The coarse model is 100 km (E-W) by 55 km (N-S) by 50 km (depth) with cell sizes of $5 \times 5 \times 5$ km and it covers Kilauea and the southeastern part of Mauna Loa, including its summit. The fine model is $60 \times 30 \times 50$ km with cell sizes of $1 \times 1 \times 1$ km and it covers Kilauea's summit, rift zones, south flank and part of the Kaoiki fault system. Given the relatively gentle topography of Kilauea, no correction is made for elevation and

Figure 3.4: One-dimensional velocity model used for the inversion. The solid line shows the standard layered velocity model modified from *Klein et al.* [1981]. It was routinely used by the HVO to locate earthquakes in 1986. The thin solid line shows the modified layered velocity model used to determine the appropriateness of lower velocity layers. The shallow part of this velocity model is modified from *Hill* [1969] and *Crosson and Koyanagi* [1979], who suggested a P wave velocity of as low as 1.8 km/s for the shallowest velocity layer. Below 1.5 km the model is the same as the original model.
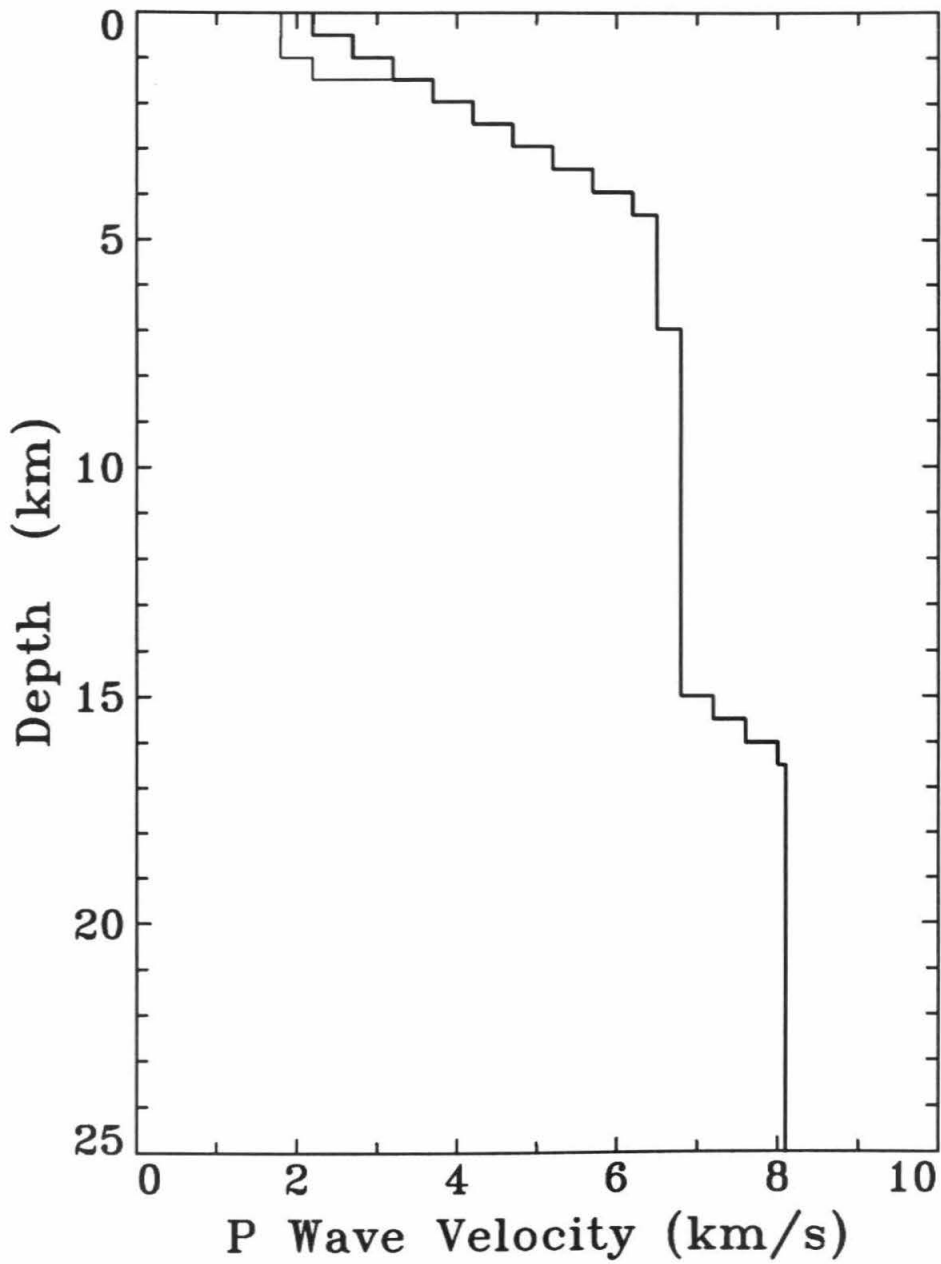
therefore the model spaces start at sea level (i.e., 0 km = sea level) and all depths are relative to sea level. Each cell contains a constant $\triangle s$ and the travel time residual of the ith ray is:

$$\triangle t_i = \sum_j l_{ij} \triangle s_j \tag{3.2}$$

where l_{ij} is the length of the ith ray in the jth cell and $\triangle s_j$ is the slowness residual in the jth cell. To solve for the change of slowness in each cell, an iterative back projection technique is used [*Clayton and Comer*, 1983; *Hager and Clayton*, 1991]. This method can handle large $\triangle s$ models with small cell sizes, providing better resolution and/or large data sets, providing more complete coverage. The basic algorithm for each iteration, k, is:

$$\triangle t_i^k = \triangle t_i^o - \sum_j l_{ij} \triangle s_j^k \tag{3.3}$$

$$\triangle s_j^{up} = \frac{\sum_i (w_i^t \triangle t_i^k / L_i) l_{ij}}{\sum_i w_i^t l_{ij} + \mu} \tag{3.4}$$

$$\triangle s_j^{k+1} = \triangle s_j^k + \triangle s_j^{up}. \tag{3.5}$$

The travel time residual, $\triangle t_i^k$, of the ith ray after the kth iteration, is the amount of time unaccounted for by the previous iteration. The initial residual, $\triangle t_i^o$, is defined by Eqn. 3.2, while w_i^t is the weight given to the travel time residual. The updated change of slowness, $\triangle s_j^{up}$ in the jth cell, is determined by distributing the kth travel time residual into each cell the ray passes through. This is done by dividing $\triangle t$ by its total path length L_i and multiplying each fractional time by the length of the ith ray in the jth cell, l_{ij} (Eqn. 3.4). The numerator is then normalized by the sum of the ray lengths in each cell plus a damping factor, μ. The last equation, Eqn. 3.5,

updates the change in slowness for the next iteration. The process is repeated until the standard deviation in $\triangle s_j^{up}$ has converged to the point where it is changing insignificantly between iterations. For the two models presented, 50 iterations is sufficient to reduce the change in standard deviation in $\triangle s_j^{up}$ between iterations by $<2\%$.

The damping factor, μ, in the second iterative step (Eqn. 3.5) restricts the excitation of unconstrained regions of the model. It is the only adjustable input parameter and it is determined in two ways. As a first approximation, the inversion is done at a range of μ values and the resulting images are compared. Damping factors that produce images with almost no amplitude of $\triangle s$ are rejected as too large (e.g., $\mu=100$), while μ's that produce images with too many high amplitude $\triangle s$'s are rejected as too small (e.g., $\mu=25$). Secondly, the variance in $\triangle s$ for a half-space velocity model, for a range of μ's, is calculated using a random number set, with Gaussian distribution and variance of unity, for the initial $\triangle t$'s. As μ increases, the variance in $\triangle s$ decreases until $\mu=50$. Above $\mu=50$ there is no significant reduction in the variance of $\triangle s$. Therefore $\mu=50$ is chosen because it gives an average amplitude signal of $\triangle s$ in the images and is the smallest damping factor limiting the variance of $\triangle s$ for a random noise data set. The data are also filtered to limit the effect of $\triangle t$'s greater than 1.0 s by clamping these noisier residuals to $\pm$ 1.0 s.

The resulting images are contoured to highlight velocity anomalies. The $\triangle s$ images for the fine model are smoothed in two steps, because of the small size of the cells. First, the $\triangle s$ values are averaged in depth by combining the anomalies of two levels to give cell sizes of $1 \times 1 \times 2$ km. Second, the $\triangle s$ values are averaged in three

dimensions by taking the average of the $\triangle s$ for each cell with 25% of the $\triangle s$ from its adjacent cells.

3.4   Resolution and Estimated Errors

It is important to consider the errors introduced into the inversion by noisy data, approximate ray tracing techniques and/or inadequate velocity models and to estimate the resolving power of the given models and model sizes. By doing a linear inversion we have inherently introduced noise into the resulting images so interpreting any anomaly must be done with care. Several variations of the inversion, including relocating the hypocenters, using different weighting schemes in the inversion, using a different one-dimensional velocity model, using different cell sizes and shifting the coarse and fine models, were done to estimate how much noise there is in the different images and to delineate robust anomalies. The idea is to eliminate poorly resolved areas using the model resolution tests and reject noisy or unstable anomalies in well-resolved areas by comparing the different strengths and weaknesses of the different inversions. We have not shown the results of all the different inversions because many of these images are similar to one another. We have presented the residual slowness images that show the most variation and in the following discussion we have tried to explain why these differences occur.

3.4.1   Model Resolution

It is impractical to calculate the entire resolution matrix for each model because of its immense size. An estimate of the resolution in each cell can be made using impulse tests, although how the resolution correlates between cells cannot be specifically

addressed by these tests. In order to interpret the results of these tests, ray coverage in the model spaces must be determined. Good ray coverage is necessary to provide adequate resolution and to limit the effect of errors in the data.

A large number of rays crossing the cell at a wide range of azimuths indicates good ray coverage. The ray coverage is depicted in Figures 3.5 and 3.6 for the two models, using the two data sets (HVO and relocated hypocenters) where each plot shows the density of rays traveling through each cell. Coverage is excellent for both models, using either data set, with >75% of the cells being hit by rays to a depth of at least 20 km. The poorest spatial density occurs along the north flank of Kilauea and some regions along the lower ERZ, particularly with increasing depth. Thus lateral velocity variations in these border regions are suspect and should not be interpreted as structures.

Impulse testing involves putting a synthetic change of slowness anomaly in certain cells, setting the other cells to zero Δs, forward modeling and inverting the data. If the resolution is good, the synthetic anomalies input should be reproduced with the same intensity and shape. The shape of the anomaly is contoured so well-resolved features produce a bull's eye-shaped pattern with the maximum amplitude in the center and the smallest amplitude defining the edge of the cell. Poor resolution is indicated by a loss of amplitude or smearing of the synthetic anomalies. Smearing is due to biased azimuthal coverage, where most of the rays are traveling in one general direction and/or poor ray coverage.

The value of each synthetic anomaly is just larger than the maximum Δs obtained in the actual inversion, so these tests approach a realistic limit of the maximum sig-

Figure 3.5: *a*. Hit count plots showing the ray coverage of the HVO hypocenters for the coarse model shown in 5-km depth slices. The hit count is the number of rays passing through each cell of the three-dimensional model. *b*. Hit count plots showing the ray coverage for the relocated hypocenters (determined using the standard layered velocity model and HYPOINVERSE [*Klein*, 1989].)
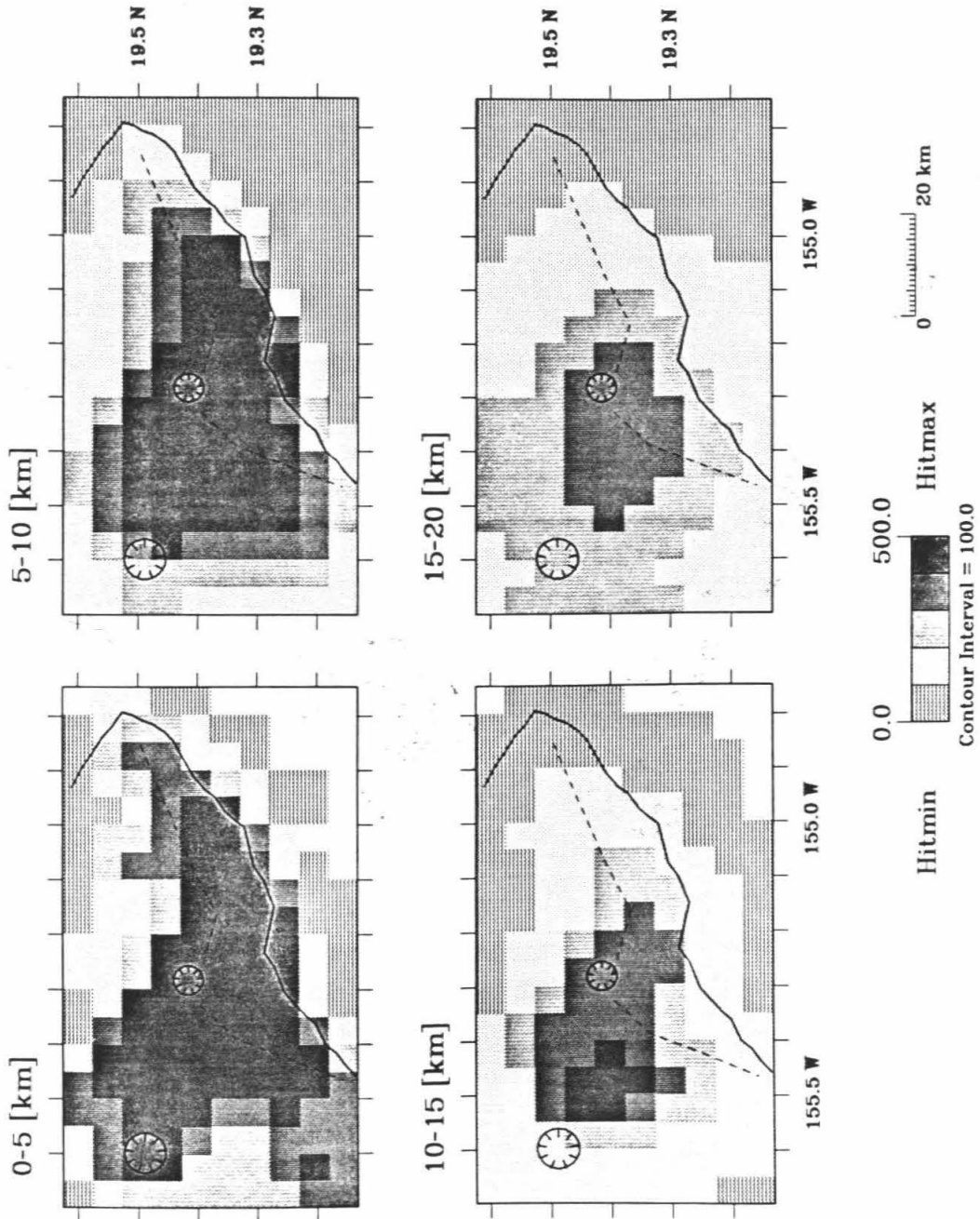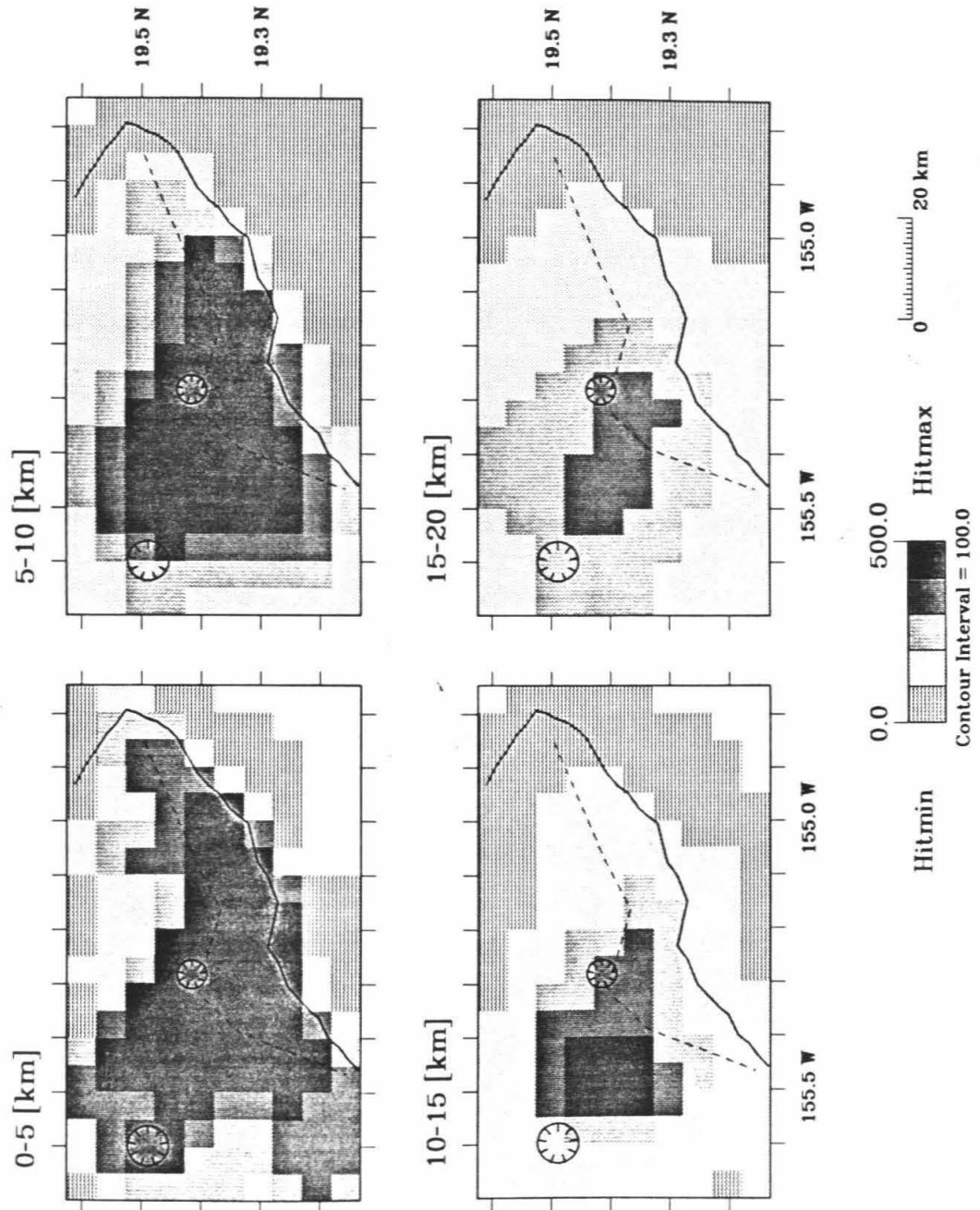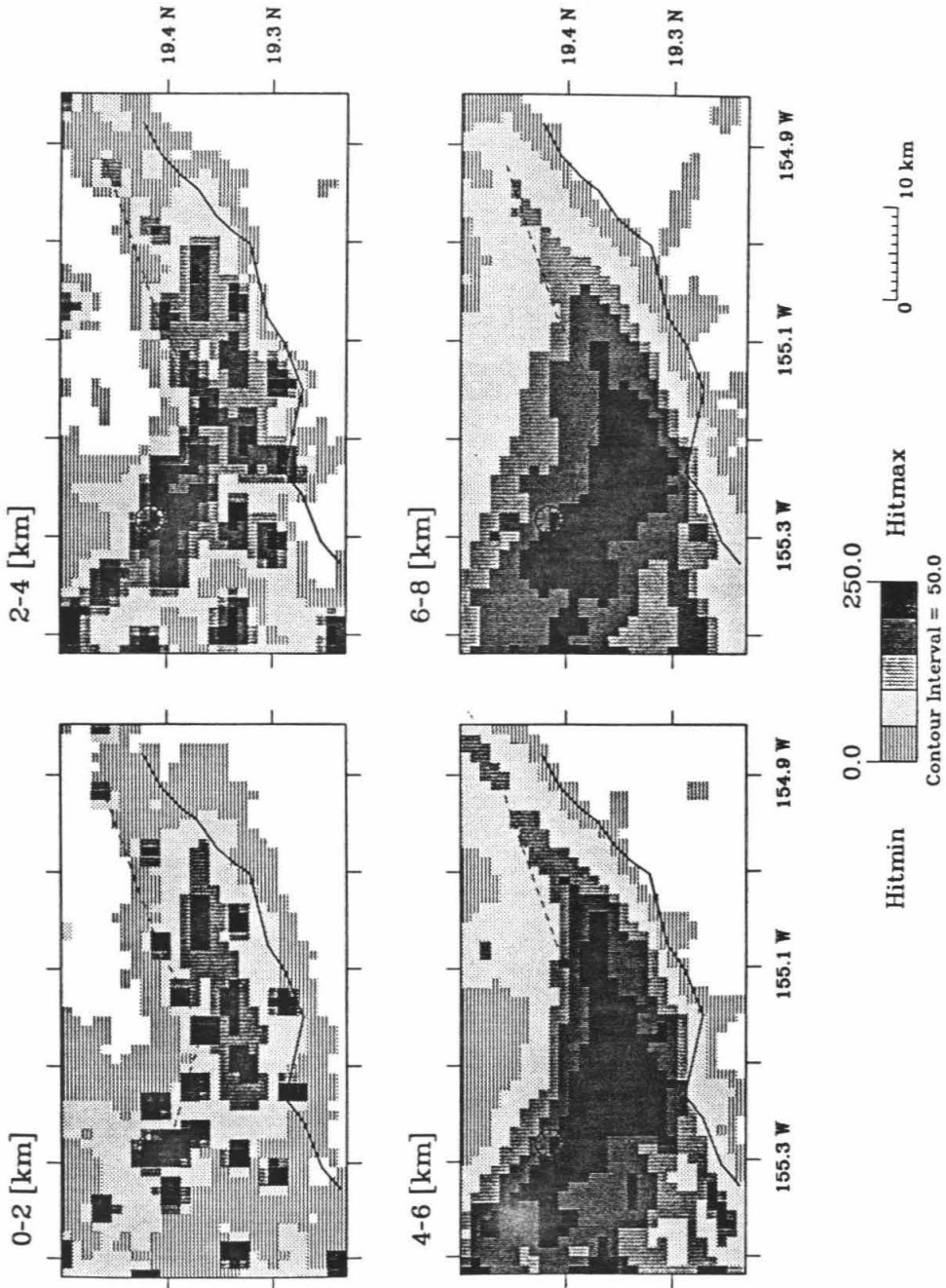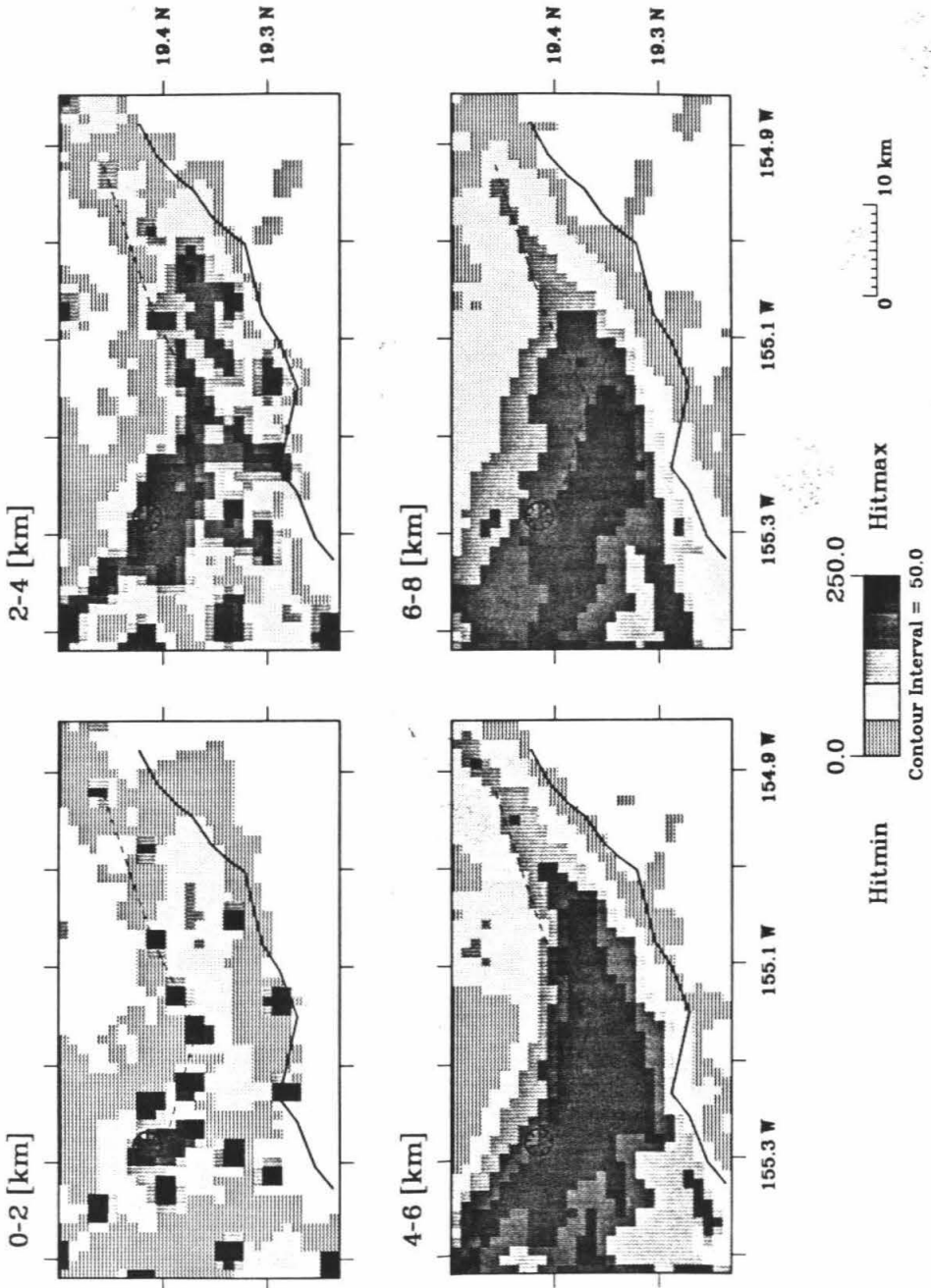
Figure 3.6: *a.* Hit count plots showing the ray coverage of the HVO hypocenters for the fine model shown in 2-km depth slices. *b.* Hit count plots showing the ray coverage for the relocated hypocenters (determined using the standard layered velocity model and HYPOINVERSE [*Klein,* 1989]).

0-2 [km]

2-4 [km]

4-6 [km]

6-8 [km]

19.4 N 19.3 N

154.9 W 155.1 W 155.3 W

Hitmin   Hitmax

0.0   250.0

Contour Interval = 50.0

0   10 km

nal or noise in the data. Synthetic anomaly locations are chosen to provide coverage
of the important, inferred structures (i.e., the summit magma reservoir) and ques-
tionable anomalies (i.e., the north flank of Kilauea). Choosing specific locations may
bias the tests, but enough different locations were tested to insure adequate and
even coverage of the models. Since the ray coverage is similar for the HVO hypocen-
ters and the relocated hypocenters, only the impulse test results using the relocated
hypocenters are shown.

Synthetic anomalies are relatively well resolved in the coarse model (Figure 3.7).
A slowness residual, $\triangle s$, of 0.05 s km^{-1}, was inserted into each depth slice separately.
The results indicate that many large amplitude anomalies add noise to the slowness
images. The noise produces small, slightly fast features along the edges of the covered
areas. For the real inversions, there are few large amplitude anomalies, so this added
noise is insignificant. To check this hypothesis, only 4 synthetic $\triangle s$'s were introduced
in the shallowest layer and no added noise (i.e., fast regions in other cells) was
produced in the images. Overall, the resolvability is excellent around Kilauea until
about 30–35 km depth where the intensity of the anomalies is significantly reduced.
Slownesses on the northern boundary of the coarse model are smeared and poorly
resolved. Anomalies along the lower ERZ and near Mauna Loa also indicate poorer
resolution at about 15–20 km and resolution decreases with depth. Beginning at 15
km depth, there is also a slight east-west smearing of some features.

Impulse tests applied to the fine model (Figure 3.8) with a $\triangle s$ of 0.1 s km^{-1}
produced poorer resolution than the coarse model. From 0 to 1 km the resolution is
good around the summit but rather poor near the bend in the ERZ and near Yellow

Figure 3.7: Impulse tests shown in 5-km layers for the coarse model to a depth of 20 km. A slowness of 0.05 s km^{-1} was input for all the locations for each depth separately. Ray paths used are from the relocated hypocenters.
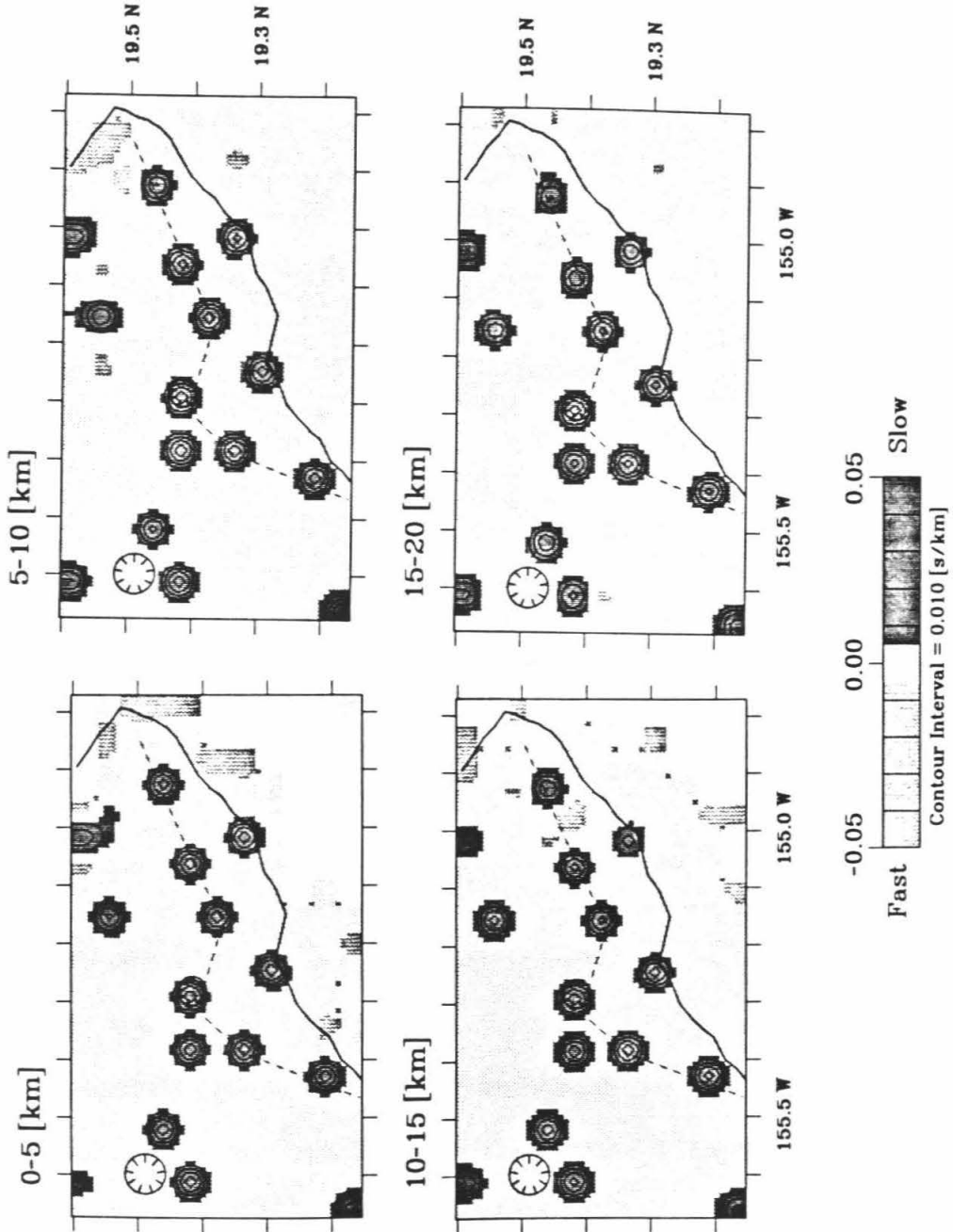
Cone on the SWRZ. Only 20–30% of the synthetics in these areas are reproduced and there is lateral smearing of some anomalies, with small fast zones added to the images. The best resolution is obtained at Kilauea summit, with >85% of the anomaly reproduced in the first 3 km, >60% recovered to 6 km and >30% recovered to 8 km. Below 2 km, the three synthetics near the bend in the ERZ and the synthetic near Yellow Cone on the SWRZ are fairly well resolved (most > 50%) with a small amount of east-west smearing of the anomalies. For the other synthetics less than half of the Δs is recovered and on average only 20–30% is reproduced, with some smearing of the anomaly. There is also some minor (less than 10% of the initial synthetic) smearing into different depth levels, which is not seen in the coarse model impulse tests. Thus the summit area is well resolved to ~8 km, but some of the shallow (< 2 km) anomalies on the rift zones show less resolution and significant smearing.

3.4.2 Data Errors

Data errors may propagate into the inversion as noise and may produce artificial velocity variations. Noisy data include bad picks and poorly determined hypocenter locations and origin times.

The HVO picks are used to define the travel time of the P wave (TT^{obs} in (1)) and are generally of high quality. The quality of the pick is indicated by a factor representing the picker's confidence in determining the start of the P wave arrival on the seismogram. The quality factor ranges from 0 to 4 where 0 indicates high confidence and 4 indicates very low confidence. The HVO picks in the data set are mostly 0's (68%) and 1's (22%), with some 2's (6%), 3's (4%) and 4's (<0.1%).

Figure 3.8: Impulse test results shown in 1-km depth slices for the fine model. A slowness of 0.1 s km^{-1} was input. Ray paths used are from the relocated hypocenters.
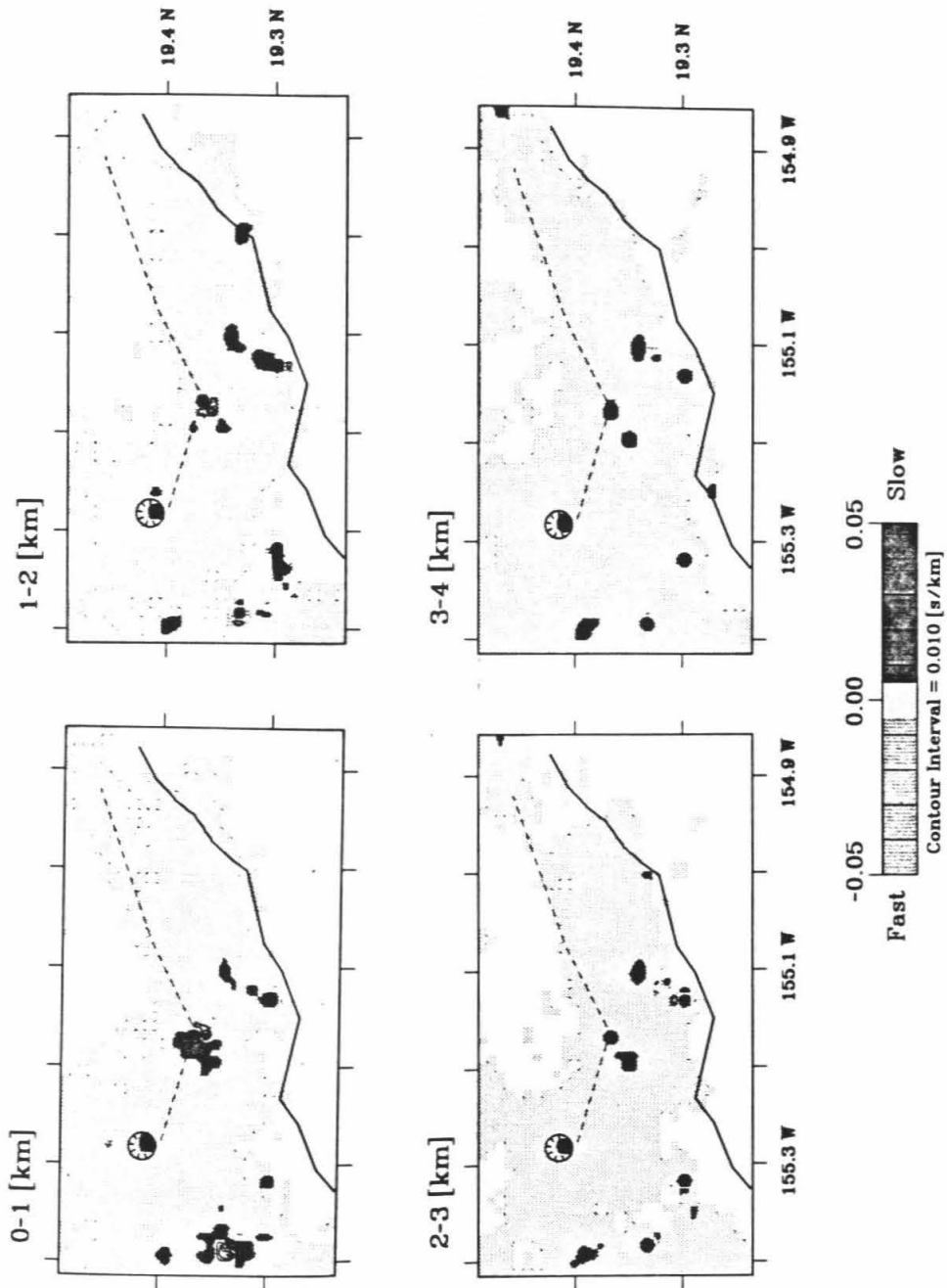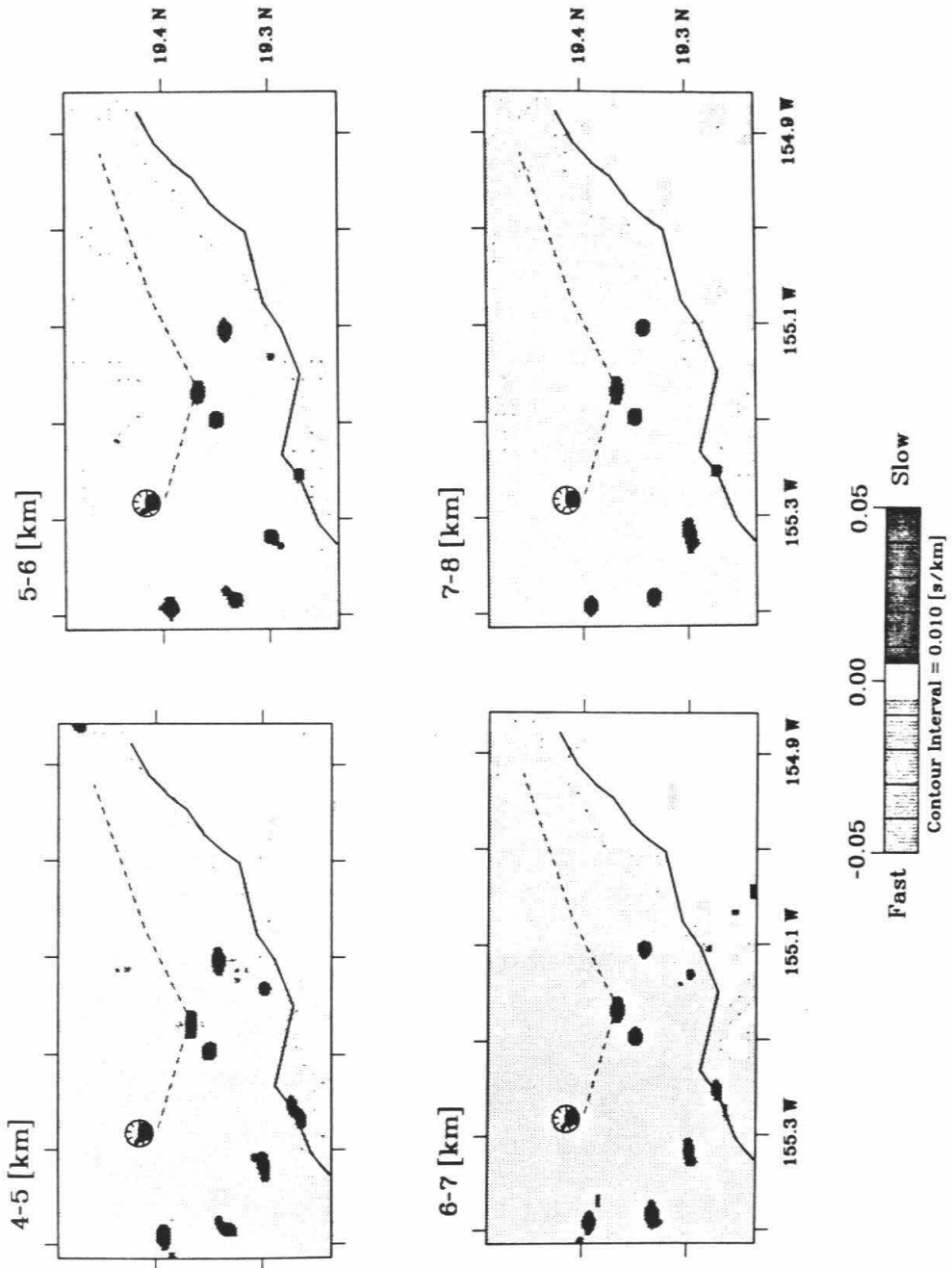
Originally the inversions were done for the HVO data without any weighting of the Δt's (i.e., $w_i^t = 1.0$ for all rays). Inversions were redone with weighting for two reasons. One, to test the effect of decreasing the significance of poorly determined picks. Two, to reduce the differences between the HVO location method, which included time and distance weighting, and our original inversion which did not. Travel times in the inversion are weighted according to the quality factors, such that a quality factor of 0 is given a weight of 1.0 and the weighting is decreased by 0.25 as the quality factor increases. A quality factor of 4 is given a weight of 0.0. The resulting images are almost exactly the same as the original images with a few, very small changes in the amplitude of a few anomalies. Large amplitude anomalies were not reduced, probably because only 10% of the picks were poor enough to be significantly down-weighted in the inversion. Therefore the quality of the HVO picks does not appear to contribute much noise to the images.

Even though the picks are relatively well determined, the hypocenters and their origin times may not be. To check the accuracy of hypocenter locations and origin times, the events were relocated using HYPOINVERSE [*Klein,* 1989] and the standard HVO layered velocity model (Figure 3.4). Travel times were weighted using the quality factors, but in addition the relocation program applies a progressive down-weighting of events that have large travel time residuals [see *Klein,* 1989]. Poor data are also filtered out by eliminating events or picks that cannot be fit within the error limits of the program. The average mean errors and their standard deviations for the relocated events (12,090) determined in HYPOINVERSE are: hypocenter depth $= 3.58$ km, horizontal distance $= 1.89$ km and the root mean square of the travel

time residuals = 0.12 s. Station delays are not applied in the relocations because they implicitly include corrections for small-scale structures near the stations that we want to image and their exclusion does not significantly reduce relocation accuracy.

The results of the relocations (Figure 3.3b) indicate that events are shifted slightly from the locations given in the original HVO phase data (Figure 3.3a). Events from January are used to compare differences in hypocenter depth and origin time between the HVO data set and the relocated events. The mean difference in depth is 1.86 ± 2.15 km and the mean difference in origin time is 0.22 ± 0.51 s. These are the absolute values of the differences; 57% of the events are shallower than the HVO locations and 67% of the origin times are earlier than the HVO times. Many of the relocated hypocenters along the summit, ERZ and south flank are shallower, while the relocated hypocenters along the Kaoiki fault zone from 5 to 10 km depth are generally shifted deeper (Figure 3.3). In terms of lateral changes, the HVO locations are shifted by <2 km. Events on the south flank, Kaoiki fault zone and LERZ tend to be shifted toward Kilauea summit, while the two shallow (< 10 km), summit clusters are less distinct after relocation (Figure 3.3b).

We have not relocated hypocenters in our three-dimensional velocity model, but *Thurber's* [1987] results indicate how significant these changes may be. The one-dimensional velocity model (similar to *Klein's,* [1981]) relocations compared to his three-dimensional velocity model relocations were more similar along the summit and USWRZ and less similar along the Kaoiki fault zone, LSWRZ and ERZ than the HVO locations compared to his three-dimensional relocations. This may be attributed to the implicit inclusion of station delays in the HVO locations and the

fact that the one-dimensional velocity model is most appropriate for Kilauea summit. In fact, *Thurber* [1987] may have avoided some of the problems related to using a one-dimensional velocity model to obtain a new three-dimensional starting model for his inversion, by reinverting over only the summit area, where the one-dimensional velocity model is most appropriate, and using a smaller set of well-located events. While it is unclear that his three-dimensional images are significantly more accurate than ours, the resulting lateral velocity variations around the summit of Kilauea are similar between the two studies.

Comparing the unweighted inversion of the original HVO data (Figures 3.9*a* and 3.10*a*) with the weighted inversion of the relocated data (Figures 3.9*b* and 3.10*b*) shows the amplitude (which partially corresponds to noise) of most of the HVO anomalies are reduced in the HYPOINVERSE images. These two sets of residual slowness images also show the most significant changes in sign and shape of the anomalies compared to inversions done using only the HVO hypocenters or the relocated hypocenters. The most obvious and important difference is that the summit area is fast in the shallow layers (0–5 km, Figure 3.9*a* and 0–2 km, Figure 3.10*a*) in the images derived from the HVO data, while the summit is slow in the same shallow layers (Figures 3.9*b* and 3.10*b*) in images derived from the relocated data. Differences at the summit cannot be explained by just adding noise to the HVO data, but are due to a combination of effects including source distribution bias, station distribution bias, station delay bias, ray path bending and velocity model.

Figure 3.9: *a.* Slowness residual plots for the HVO hypocenters for the coarse model in 5-km depth slices. The dark shaded areas represent slow velocity zones while the lighter shades represent fast velocity zones. *b.* Slowness residual plots for the relocated hypocenters for the coarse model in 5-km depth slices.
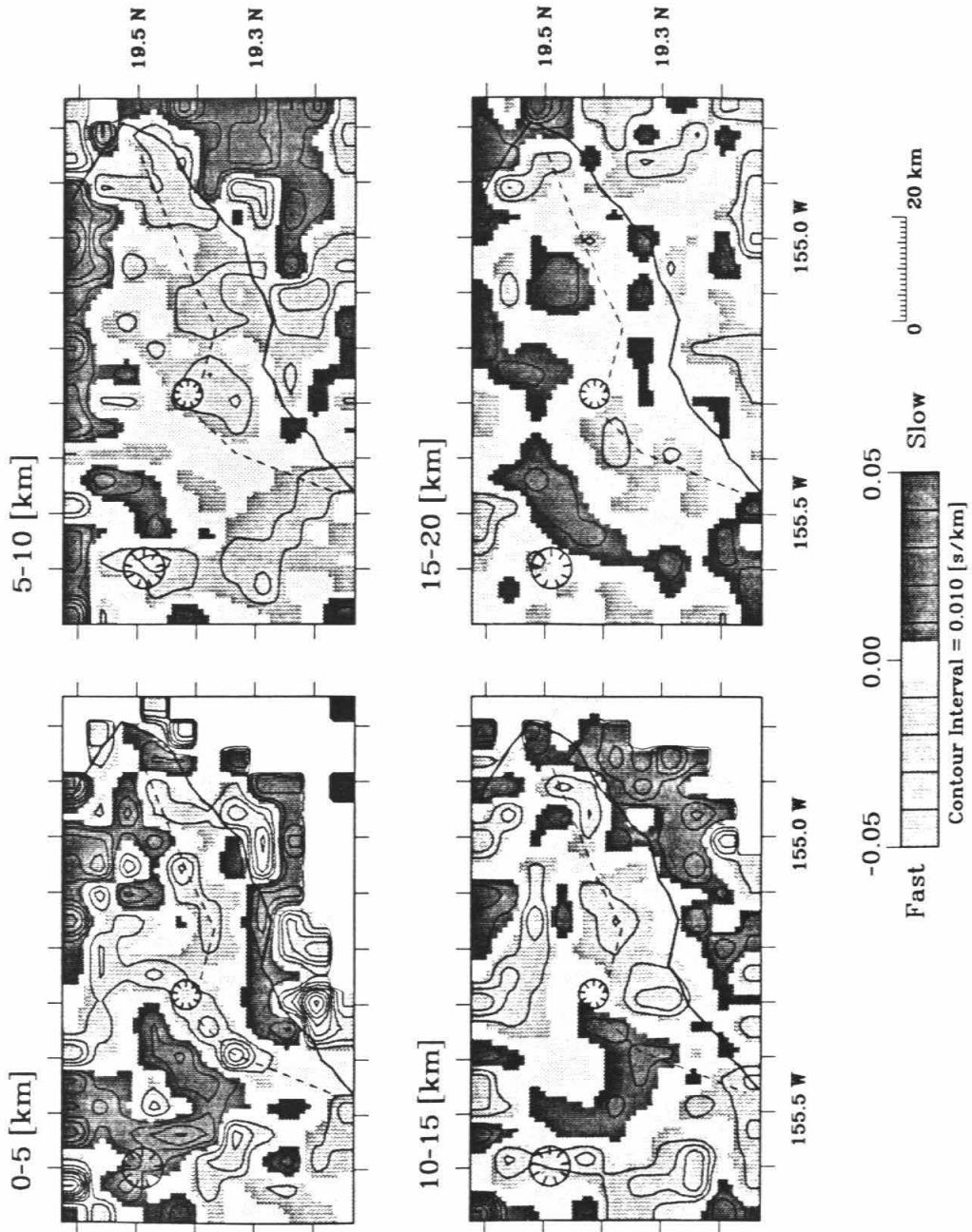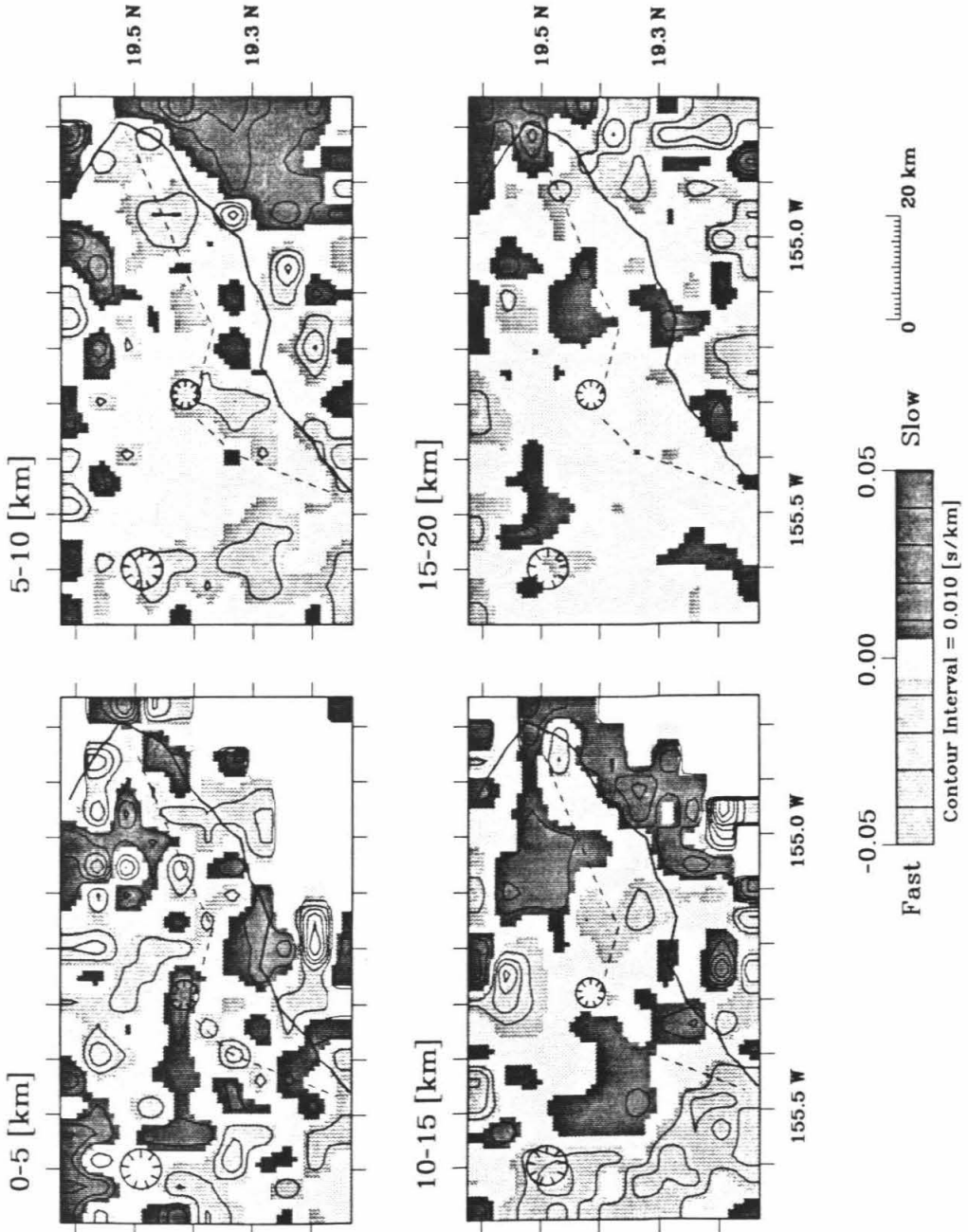
Figure 3.10: *a.* Slowness residual plots for the HVO hypocenters for the fine model in 2-km depth slices. *b.* Slowness residual plots for the relocated hypocenters for the fine model in 2-km depth slices. *c.* Slowness residual plots for the relocated hypocenters determined using the modified layered velocity model (slower shallow velocities) for the fine model in 2-km depth slices.
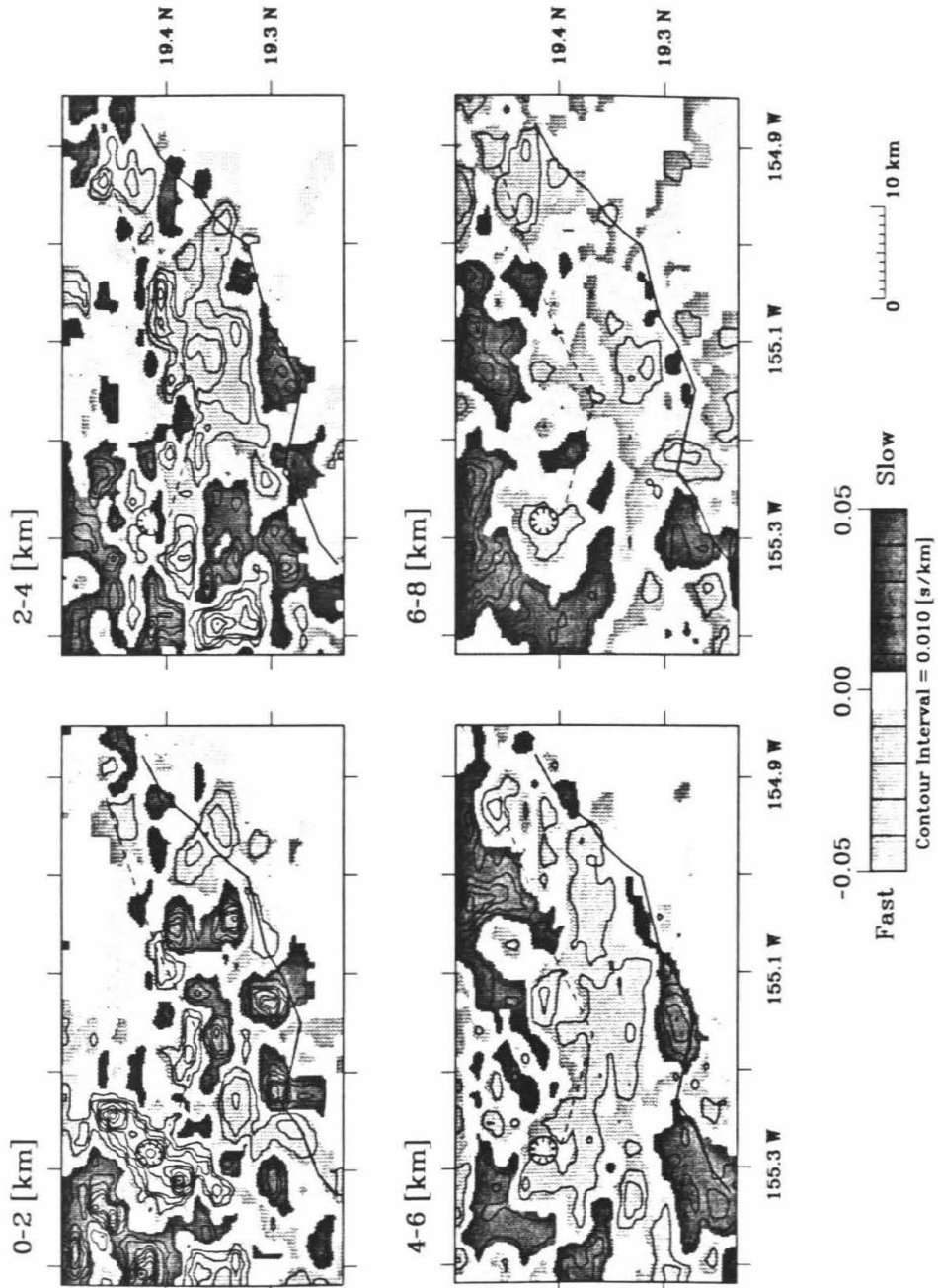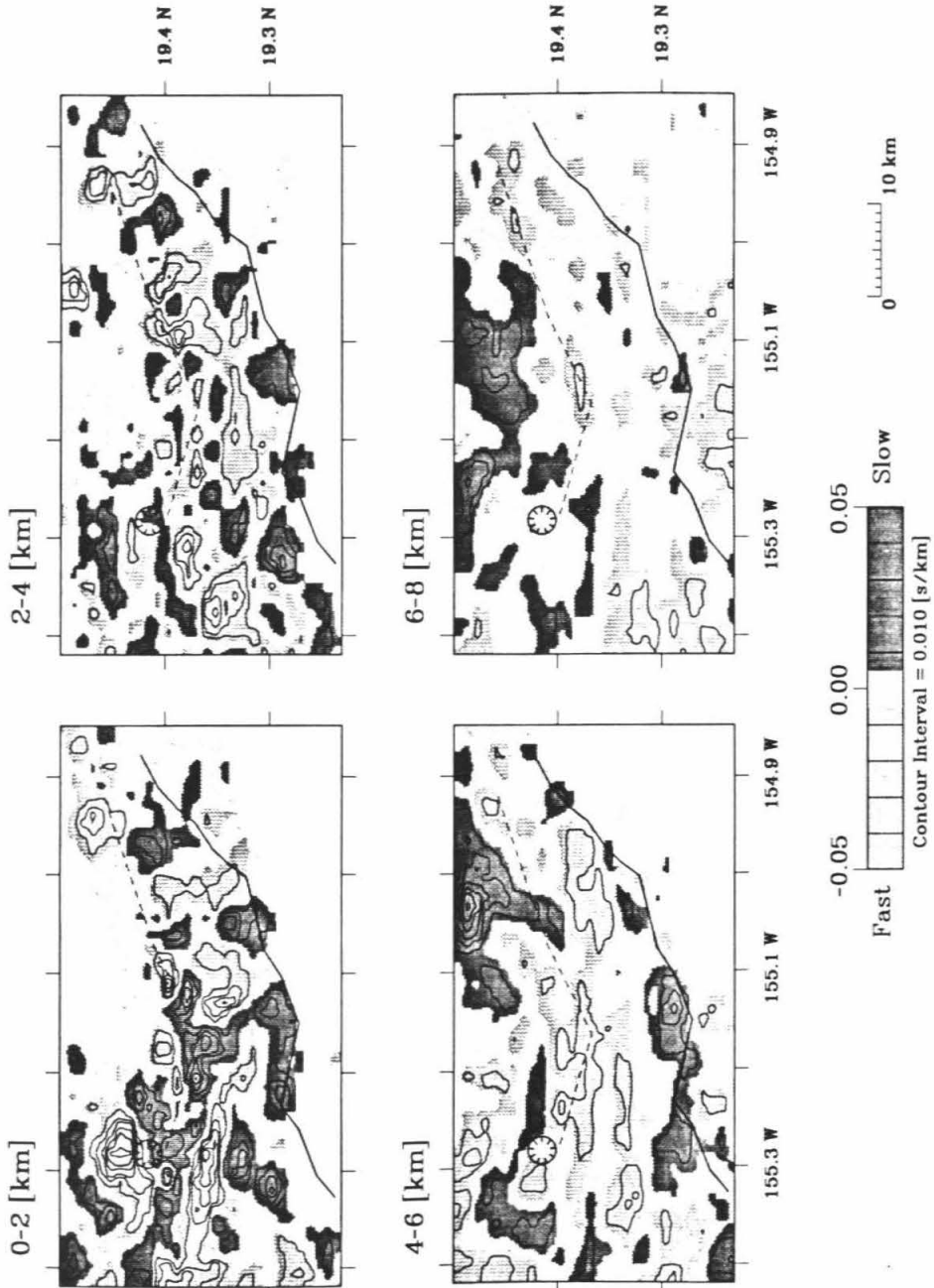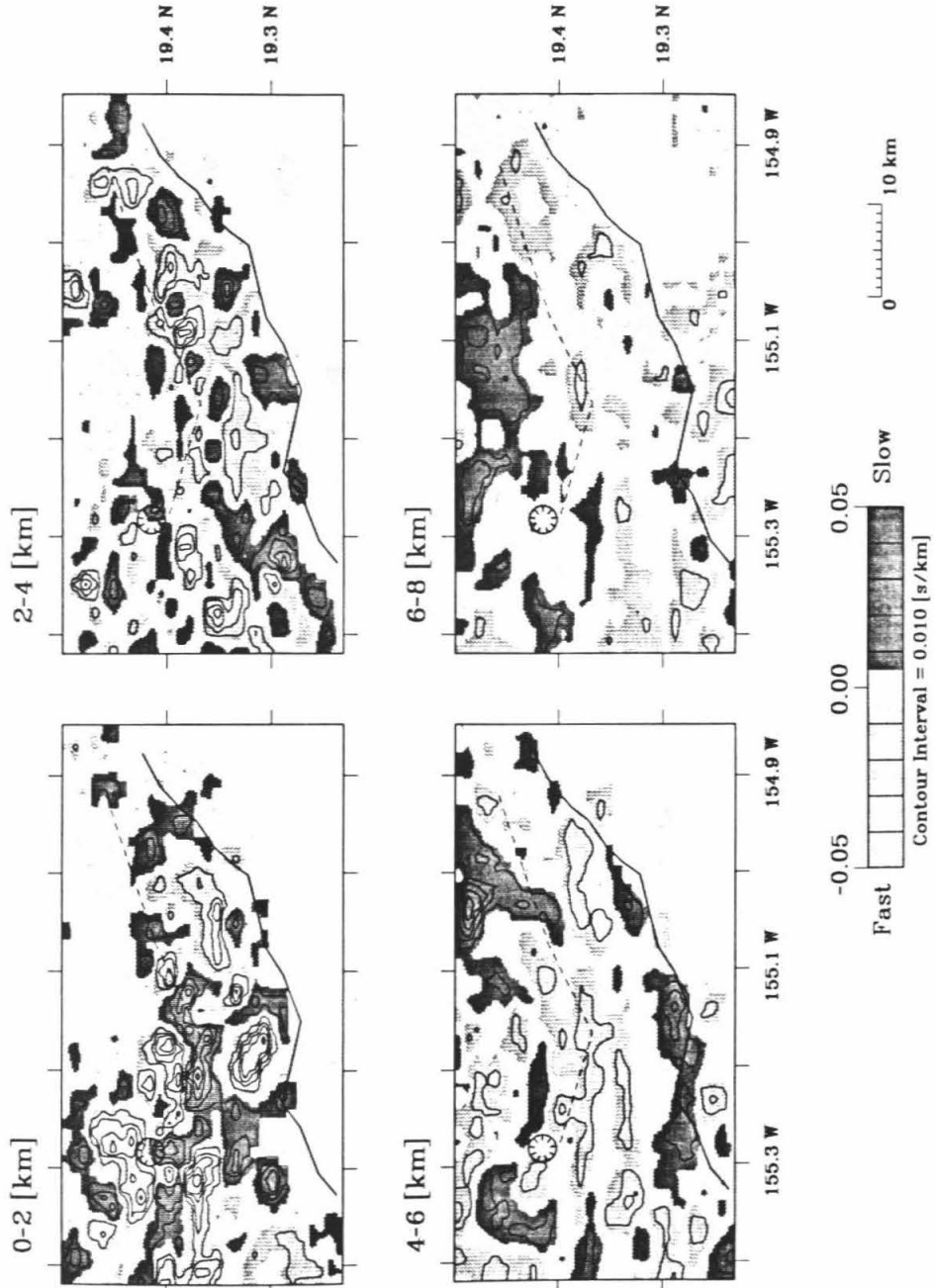
3.4.3   Model Errors

Model errors include the nonuniformity of the earthquake and station distribution and the inappropriateness of station delays, velocity models, ray tracing and model spaces. The amount of noise introduced into residual slowness images by various model errors is estimated through a series of tests. In some cases, these tests can isolate one source of model error associated with a noisy anomaly, but in most cases the inferred noise in the images comes from more than one source.

Source distribution bias refers to the clustering of hypocenters along the summit and rift zones of Kilauea (Figure 3.3). These clusters may artificially add signal to anomalies defined in these regions. To test this effect, we removed events in populated areas between 0–10 km depth. Events with magnitudes <1.25 were removed because this magnitude cutoff provided the most uniform spatial coverage. The resulting images showed some small decreases in the amplitude of some anomalies. Using the HVO hypocenter locations, with 4,892 low-magnitude events removed, the most significant changes in residual slowness occurred at the summit and along the ERZ. The large fast zone on the summit in Figure 3.10a decreased in amplitude, while the slow zone southeast of the summit increased in size and amplitude. The fast zone along the UERZ was significantly reduced and most of it was replaced with a low amplitude slow zone connected to the slow region southeast of the summit and the slow region at the bend in the ERZ. Therefore, the largest changes were near the summit in the shallowest layer (0–2 km) of the fine model and this is expected since the worst clustering occurs there (Figure 3.3). Unfortunately, it is hard to avoid this source distribution biasing without losing model resolution. *Thurber* [1987] noted

this clustering problem in his inversion of a much smaller area, covering only the summit region with less resolution.

Station distribution and station delay biases are most obvious in the shallow layers (0–4 km) of the fine model. We have uneven hit count distribution in the shallow layers (Figure 3.5) because the rays must approach the stations. Comparing the slowness images (Figure 3.10a) for the inversion of the HVO data at these shallow layers with their corresponding hit count plots (Figure 3.5a) shows that about 60% of the high hit count blocks are correlated with high amplitude anomalies and most of these anomalies are slow. These anomalies may represent the local structure beneath each station (i.e., the station delay) relative to our velocity model. We want to determine these structures, but we do not want to overinterpret anomalies that are partially or completely enhanced artifacts of the station distribution. Since we cannot move or add stations to check this biasing we tried changing the one-dimensional velocity model.

Changing the velocity model allows us to look at station biases and more importantly, the appropriateness of the standard layered velocity model. We decreased the shallow layer velocities according to the velocity models of *Crosson and Koyanagi*, [1979] and *Hill and Zucca* [1987], but left the deeper velocities the same as in the original model (See Figure 3.4). The variation in the shallow layer velocities ($> 18\%$) is larger than the largest velocity variation (14%) caused by the highest amplitude slow anomaly (~ 0.5 s km^{-1}) in the 0–2 km depth of Figure 3.10a. The events were relocated using this modified velocity model in HYPOINVERSE and the inversion was done using the same parameters as before (i.e., same damping factor and same

weighting scheme). Comparing the shallow layers (0–2 km) in Figures 3.10*b* and *c* we note a decrease in the amplitude of slow anomalies and an increase in the amplitude of fast anomalies along the south flank and the upper and middle ERZ in Figure 3.10*c*. We believe these differences are caused by changing the velocity model and do not reflect station distribution bias. There are two areas in the 0–2 km depth that are different between the inversions and may be artifacts of the station distribution. The two slow anomalies near Mauna Iki and Kilauea Iki are significantly reduced in signal by changing the velocity model, while the other slow features along the summit and ERZ are not dramatically reduced (Figure 3.10*c*). This suggests that station distribution and clustering of ray paths to Mauna Iki and Kilauea Iki stations has artificially enhanced the signal in these two regions. Given the instability of these two slow anomalies, they may not be related to the structural character of these areas.

The appropriateness of the model space was checked by shifting the model grids by one half their cell size and by using different cell sizes (3x3x3 km and 4x4x4 km). Shifting the model grids did not change the slowness images although the shape of some of the anomalies varied. Using different cell sizes did not change the slowness images either and given that the resolution tests indicate anomalies can be resolved using the smaller cell size of the fine model we have shown these results in this paper. So, in general, the model spaces chosen for the inversion are reasonable and do not add any significant biasing to the inversion.

The approximate ray tracing technique (ART) can only approximate the real path so it is important to estimate the effect of slightly different ray paths on the

images. Two sets of slightly different ray paths and travel times were obtained for hypocenters from events in January. For one set, hypocenters were relocated and inverted with travel time residual weighting applied in both steps. For the second set, hypocenters were relocated and inverted without weighting applied in either step. The weighted ray paths tended to be more concentrated near the summit and at shallower levels, while the unweighted ray paths were more dispersed, traveling to the stations from a greater distance. Tighter clustering of events for the weighted case may add a small source distribution bias, while the longer ray paths for the unweighted case may reduce the travel time residual by distributing it over a longer ray segment, thus offsetting the larger errors in this case. The resulting images for the two cases are very similar suggesting that small differences in ray paths do not significantly effect the images. Therefore more accurate locations and more accurate ray paths can account for small changes in the size and shape of anomalies, but do not really change the sign (i.e., fast or slow) of the signal.

Although small changes in ray paths do not effect the resulting images, ray bending may not have such a subtle effect. The ART models straight line segments and cannot model rays that bend or curve around a large velocity variation. Ray paths around the summit of Kilauea at a shallow level (i.e., where the magma reservoir is inferred) may be significantly affected by the bending of these rays around a magma chamber through much faster intrusive dikes. Some important changes in the residual slowness anomalies for the fine model (Figure 3.10) in the shallow summit region may be partly due to this effect but only a more complete inversion with a three-dimensional velocity model and the appropriate ray tracing technique can address

this issue.

Returning to the original inversion using the HVO data, the large, high amplitude fast region on the summit in the fine model (0–2 km, Figure 3.10a) is partly an artifact of source distribution, station distribution and station delays. Unfortunately, because of its size and location it may be covering and averaging out slow anomalies that are imaged in the inversions using relocated hypocenters. This fast zone may also be partially due to the one-dimensional approximate ray tracing technique that cannot account for rays bending around a shallow reservoir between two sharp velocity discontinuities. Given these important concerns about the stability of the summit anomalies, we have chosen to interpret the shallow summit (0–4 km) as fast just north and northwest of the summit and slow just southeast of the summit.

3.5   Results and Discussion

The residual slowness images derived from the tomographic inversions are consistent with current models of Kilauea's conduit plumbing system and provide important insight into some of the small-scale structures that are poorly defined by previous workers [*Ellsworth and Koyanagi*, 1977; *Crosson and Koyanagi*, 1979; *Ryan et al.*, 1981; *Thurber*, 1984; *Hill and Zucca*, 1987]. The results show detailed lateral hetero-geneities and define structures in aseismic zones not covered by geophysical studies using only seismicity patterns [*Ryan et al.*, 1981]. *Hill and Zucca* [1987] summarized the range of P wave velocities expected from different Hawaiian rocks and using their table [*Hill and Zucca*, 1987, Table 37.2] as a guide, interpretations of velocity anomalies in the residual slowness images (Figures 3.9 and 3.10) have been inferred.

In general, a slow velocity may correspond to weaker, porous, subaerial lava, an area with large fractures or an area with a high fluid to rock ratio (e.g., magma or partial melt). A fast velocity may correspond to dense intrusive bodies, buried pillow basalts or possibly cumulate material. The features described below are mainly robust anomalies related to the subsurface structure of Kilauea and are not artifacts of noise in the data or the propagation of noisy data in the model. The following discussion summarizes the main structures inferred from the residual slowness images in the six major tectonic zones of Kilauea and compares the tomographic results to previous geophysical models.

3.5.1   Kilauea Summit

The coarse model (Figure 3.9) averages much of the significant small-scale structure of the shallow summit reservoir, but may define the extent of the vertical conduit. From 5 to 10 km depth, there is a fast zone centered due south of the summit that may represent part of the main vertical passageway for Kilauea's magma supply. *Ryan et al.* [1981] inferred a primary, elliptical-shaped conduit just southeast of Halemaumau extending from a depth of 6.5–14.6 km. Their conduit flares out to the south with depth. The fast region in our inversion is shorter, extending to ~10 km depth. More recent studies are consistent with a shorter conduit. *Hill and Zucca* [1987] described the main conduit as a sheeted, dike-like complex widening to the south until a depth of ~9 km. *Thurber* [1984 and 1987] also found a similar southward shift of the high velocity conduit with increasing depth to 8 km. *Delaney et al.* [1990] used the relatively steady, long term ground deformation data from Kilauea to suggest an extensive vertical conduit system to at least 9 km.

The cross sectional area of the fast region beneath the summit is larger than *Ryan et al.'s* [1981] inferred conduit and probably includes some structural information about the south flank. The high velocity region is in the same general location as a cluster of seismicity centered beneath the south flank from 5 to 10 km depth in *Klein et al.'s* [1987, Figure 43.18A] summary of Kilauea's seismicity. Klein et al.'s cross section is a little misleading because most of the earthquakes in this cluster define a linear zone just east of Halemaumau on the south flank in plan view. In fact, the fast zone (Figure 3.10) is centered where there is a lack of seismicity (Figure 3.3). Therefore part of the fast zone may be related to a relatively consolidated, mobile block separated from similar blocks by lines of breakage [*Ryan*, 1988] such as Klein et al.'s linear cluster. Furthermore, this high velocity region may be easily distinguished because it overlies a low velocity layer of oceanic sediments inferred to lie just beneath this zone of seismicity [*Crosson and Koyanagi*, 1979; *Furumoto and Kovach*, 1979; *Crosson and Endo*, 1982; *Li et al.*, 1992].

The fine model (Figure 3.10) provides more detail of the shallow reservoir and conduit structure to a depth of 8 km. From 0 to 2 km, a concentrated, high amplitude fast zone is centered north of the summit. This high velocity region probably represents a partial wall and/or cap of dense intrusive material surrounding and bounding the magma reservoir on its north side. Such a fast zone has been suggested by *Ryan et al.* [1981], who modeled an elliptical magma chamber crown at a depth of 1.1–1.9 km. *Thurber* [1984, 1987] also inferred a roof to the shallow reservoir from a high velocity region imaged just north of the summit extending to ~2 km depth.

Slightly southeast of the summit, a slow zone extending away from the summit

(Figures 3.10b and c) may represent the shallow magma reservoir. The summit reservoir is poorly defined in Figure 3.10a because the lower velocities are overwhelmed by the high velocity anomaly to the north. Previous workers have modeled a shallow reservoir at approximately 2–4 km depth southeast of the summit [*Ryan et al.,* 1981; *Thurber,* 1984, 1987; P. Ho-Liu et al., preprint, 1991]. *Thurber* [1984, 1987] imaged a localized, low-velocity zone from 1.5–2.5 km. Many workers have suggested that the shallow magma reservoir of Kilauea is a laterally elongate, planar, compartmentalized body of dikes and sills rather than a simple, spherical magma chamber [*Fiske and Kinoshita,* 1969; *Swanson et al.,* 1976; *Ryan et al.,* 1981; *Duffield et al.,* 1982; *Wilson and Head,* 1988]. The residual slowness images complement these models since the slow zone is laterally extensive to the southeast but is surrounded by fast regions.

In the next depth level (2–4 km) the summit is slightly fast north of the caldera and slightly slow south of the caldera. These anomalies are remnants of the stronger anomalies in the shallower layer and probably do not extend to a depth of 4 km. Therefore the magma chamber beneath Kilauea is inferred to be a laterally extensive, southeastward trending zone of partial melt centered ~2 km south of Halemaumau crater at a depth of 0–3 km.

3.5.2   Rift Zones
ERZ

In the coarse model (Figure 3.9), the ERZ has two distinct fast anomalies along its surface trace near Makaopuhi and Kalalua Cone in the shallowest layer (0–5 km). The intensity of the anomaly near Kalalua suggests a high concentration of intrusive

dikes and it may be a transient magma barrier as *Klein et al.* [1987] have inferred. The depth to which the rift zones extend as structural entities is questionable. The images indicate that the ERZ may extend as deep as 15 km as a discontinuous high velocity region. *Ryan* [1988] used a finite element model to infer melt-filled rift zones from 6 to 10 km, supplied with picritic magmas (i.e., cumulate-rich mush) along the boundary with the oceanic crust while *Delaney et al.* [1990] indicated a dike-like structure for the rifts to 9 km depth.

The ERZ has a high velocity signal to at least 6 km depth, which is broken up by slow features in the fine model (Figure 3.10). We believe these slow anomalies are due mainly to magmatic activity but other structures may explain the low velocities (e.g., cracks, rifts, weathering, temperature variations or porosity). We prefer to interpret these slow velocities as zones of partial melts because there is strong evidence (described below) for concentrated magma pockets and very little evidence for significant, anomalous zones of high porosity basaltic rock or regions along the upper parts of the rifts that contain a greater density of cracks and fractures. The one exception is the Great Crack along the LSWRZ which is poorly delineated in the shallow layer of the coarse model by any significant velocity anomaly, although it is slightly slow in Figure 3.9*b*.

The fine model suggests small magma reservoirs at shallow levels (0–2 km) beneath Mauna Ulu, Makaopuhi and Puu Oo. The large amplitude slow region extending from Mauna Ulu to Puu Oo is most likely related to magma storage for the current eruption, which has been active since 1983, and past, relatively voluminous eruptions at Mauna Ulu and Makaopuhi. Extensive slow regions and lack of sig-

nificant fast regions, suggest a relatively open conduit system along the UERZ at shallow levels. Previous workers have suggested a similar structural model from a variety of geophysical studies [*Eaton and Murata,* 1960; *Jackson et al.,* 1975; *Swanson et al.,* 1976; *Ryan et al.,* 1981; *Decker,* 1987; *Klein et al.,* 1987; *Hoffmann et al.,* 1990; P. Ho-Liu et al., preprint, 1991]. P. Ho-Liu et al. found attenuating anomalies at Mauna Ulu and Puu Oo using seismic data from 1986, supporting our suggestion of shallow magma pockets. *Klein et al.* [1987] indicated magma zones near the summit, at Makaopuhi and along a region between Puu Kamoamoa and Kalalua. The inferred magma pocket under Mauna Ulu and Makaopuhi may be a more long-lived storage zone present before the Mauna Ulu eruptions of 1968–1971. *Jackson et al.* [1975] and *Swanson et al.* [1976] used geodetic and petrographic information to suggest a shallow magma reservoir beneath Makaopuhi Crater before the 1968 and 1969 eruptions. Their evidence included many shallow earthquakes (<5 km), uplift of the area and the eruption of hybrid and differentiated lavas which indicated prolonged storage before extrusion. The idea of a long-lived magma pocket near the bend in the ERZ is consistent with the seismic and geodetic history of Kilauea. Using the magma supply rate, 0.1 km^3yr^{-1} [*Swanson,* 1972; *Dzurisin et al.,* 1984] and the estimated volume of the magma reservoir, 11 km^3 [*Wright,* 1984] the average residence time for magma is 100 - 120 years [*Decker,* 1987]. Therefore some of the anomalies in the images may be due to long term magma storage zones along the ERZ that probably receive new injections of magma from the hotspot source.

At Kalalua, just east of the slow region, the fast area in the fine model (0–2 km) may represent an intrusive barrier to magma migration in the ERZ conduit.

From 2 to 4 km the ERZ is generally fast and the southward spreading of these fast regions suggests intrusive diking along the ERZ widens with depth. The fast regions at Kalalua and Kaliu probably represent a zone of dense intrusives acting to impede magma migration at this level. *Klein et al.,* [1987] indicated that intrusion of magma beyond these barriers is rare. Except for 1955 and 1960, most of the recent eruptive activity on Kilauea has been confined to the upper and middle east rift zone, west of Kalalua [*Dzurisin et al.,* 1984; *Decker,* 1987]. In fact, there have only been 2 out of 30 seismicity-related rift zone injections into the LERZ since the 1975 Kalapana earthquake [*Decker,* 1987].

SWRZ

The southwest rift zone in the coarse model (Figure 3.9, 0–5 km) is fast along its surface trace to near Mauna Iki. The fast region at the bend has a very high amplitude, indicating a relatively more concentrated zone of intrusives acting as a barrier to magma propagation [*Klein et al.,* 1987]. The presence of this feature at the bend is probably not a coincidence, but is related to increased stresses introduced by the change in structural character and direction of the rift and the rift's proximity to Mauna Loa. The lower SWRZ is average (Figure 3.9*a*) to slow (Figure 3.9*b*) possibly due to the presence of the Great Crack, a large grabenlike structure whose tensional rifts would tend to reduce velocities of rays traveling perpendicular to the cracks. From 10 to 15 km, the trace of the SWRZ is partially covered by a slightly slow zone paralleling the surface trace of the rift. This slow anomaly is similar to the attenuating anomaly imaged by P. Ho-Liu et al. (preprint, 1991) along the same region. Although we cannot explain this anomaly, we believe the seismic velocities

are slightly slower than average in this area and more work is needed to determine the structural character of this region.

The SWRZ shows a similar overall pattern as the ERZ in the fine model (Figures 3.10a and b). The rift is fast and the high velocity begins to diffuse below ~6 km. There are some slow patches that break up the fast regions but most of these anomalies are not robust between the different inversions. From 2 to 4 km depth, there are two large fast zones, one very close to the summit and the other near Mauna Iki, that are probably related to intrusives. These structures may act as barriers to eruptions or intrusions along the SWRZ. *Klein et al.* [1987] defined Mauna Iki as a major barrier to magma migration and our images suggest this barrier is within 2–4 km depth.

Deep Structure of Rifts

The deep structure of the rift zones is controversial because ground deformation studies, gravity data and refraction surveys cannot produce unique models. The residual slowness images have both fast and slow anomalies beneath the rifts related to the rift conduits structural complexity. It is generally agreed that dikes are intruded either vertically or steeply southward dipping and they tend to have tapered, blade-like ends because of the stresses placed on the dike tips [*Fiske and Jackson*, 1972; *Swanson et al.*, 1976; *Rubin and Pollard*, 1987; *Dieterich*, 1988]. The geometry and growth of the dike complex is problematic. *Swanson et al.* [1976] agreed with *Kinoshita et al.'s* [1963] interpretation of the dike complex having a shallowly dipping north flank and a steeply dipping south flank. They suggested the growing dike complex moves southward and intrudes younger dikes, on average, at a higher elevation,

thus producing a steep south side to the complex [*Swanson et al.*, 1976, Figure 19]. This geometry was modified by later workers whose data suggest a shallowly dipping south side of the rift complex [*Crosson and Endo*, 1982; *Thurber*, 1984; *Hill and Zucca*, 1987]. The south side may have a shallower dip, if vertical dikes are pushed southward as more dikes are intruded at the active crest and these dikes become buried by new lava flows from the topographically higher rift conduit as the ERZ grows [*Hill and Zucca*, 1987, Figure 37.12]. Thus, after a period of growth, the rifts have a triangular high velocity core. Our slowness images show a more asymmetric southward widening of the fast regions along the ERZ with almost no fast anomalies north of the rift. This suggests a more complicated, nonuniform growth of the rift with a greater build-up of intrusive dikes on the south side of the rift.

3.5.3   Fault Systems

The Hilina fault system is imaged as slow regions to ~6 km. In the coarse model (0–5 km) there are coastal slow zones at 155.34^{o}W along the Hilina Pali, at 155.12^{o}W along the Holei Pali and at 155.05^{o}W south of Kalalua, on the eastern segment of the Hilina fault system. These coastal slow anomalies are also seen in the fine model from 0 to 6 km and correlate with the attenuating anomalies from 0 to 6 km imaged by P. Ho-Liu et al. (preprint, 1991). These low velocity features are probably due to the subaerial lava flows and fractures created by the normal faults of the Hilina System. In general, slow velocities and high attenuation are associated with faulting. Many workers have indicated that the Hilina faults are very shallow features, extending only into Kilauea's hyaloclastic layer, from 1 to 3 km depth [*Moore and Fiske*, 1969; *Swanson et al.*, 1976; *Crosson and Endo*, 1982; *Hill and Zucca*, 1987]. The slow

anomalies extend deeper than 3 km indicating the Hilina faults may be deeper.

The Koae fault system is indistinguishable in the coarse model, but some of its structural complexity can be deciphered in the fine model (Figure 3.10). In the shallowest layer, 0–2 km, the northeastern end of the Koae is slow. In Figure 3.10a, the slow anomaly is isolated, while in Figure 3.10b the slow anomaly is connected to our inferred shallow reservoir slow anomaly. The evidence for an open, direct connection between the summit reservoir and the Koae fault system is inconclusive. Our preferred interpretation of the slow anomalies in Figure 3.10b is that these slow regions are not connected and have just smeared into one another due to smoothing and contouring. The rest of the Koae (southwestern three-fourths of the fault system) in the shallow layer, 0–2 km, is fast. In the next depth slice (2–4 km), the fault's surface trace has an average velocity bounded by the fast anomaly related to a SWRZ intrusive barrier to the north and a slow anomaly to the south that is possibly related to the subaerial basaltic flows on the south flank (Figure 3.10b). From 4 to 6 km the Koae is part of the high velocity region related to dike intrusions along the rifts. The Koae is a difficult fault zone to interpret from the images and its complicated history. It is an extensional fault system to approximately 10 km [*Duffield*, 1975], but because it is connected to the rift zones it is also a zone of intrusive diking [*Yang et al.*, 1992; *Klein et al.*, 1987; *Thurber*, 1987; *Ellsworth and Koyanagi*, 1977; *Swanson et al.*, 1976] and rare eruptions [*Duffield*, 1975]. The Koae may be an ancient caldera-rift system of Kilauea [*Holcomb*, 1987; *Duffield*, 1975] and its development may be directly related to the forceful intrusion of magma, like the current rift system. *Thurber* [1984 and 1987] and *Ellsworth and Koyanagi* [1977] imaged the Koae as a

high velocity region in their inversions. *Yang et al.* [1992] re-examined geodetic data and modeled many dike intrusions along the Koae to a maximum depth of 9 km. They defined a zone of intrusion (i.e., "South Intrusion Dike Zone") from the summit southward toward the Koae and then intruding southwestward along the Koae fault zone to 5 km depth which is consistent with the fast anomalies in our images. The shallow slow anomaly along the northeast end of the Koae may be related to tensional cracks or possibly a small zone of partial melt. *Swanson et al.* [1976] noted that dilation along the Koae increased to the east and *Thurber* [1987] noted that focal mechanisms of earthquakes at deeper depths (4–8 km) indicated north-south tension on the eastern Koae and north-south compression on the western Koae. There is also more melt currently being supplied and stored along the UERZ than the SWRZ [*Duffield et al.*, 1982] and *Klein et al.* [1987] have distinguished a "transition region" between the ERZ and the Koae fault zone where in 1973 magma intruded uprift. So a small zone of magma storage at the intersection of the Koae and the ERZ is a plausible cause for slow velocities.

The shallow Kaoiki fault system (0–5 km depth, Figure 3.9) has slow to average velocity anomalies in the coarse model possibly related to shallow tensional structures defined along the surface of the fault zone. Southeast facing en-echelon sets of normal faults may have performed the same structural function for Mauna Loa as the Hilina fault system currently performs for Kilauea [*Lipman*, 1980]. From 10 to 15 km depth, the Kaoiki has a slightly slow anomaly, which also covers part of the SWRZ, but as discussed earlier we do not have a structural interpretation for this small deviation in the average velocity. If the Kaoiki intersects the SWRZ near its boundary with

the oceanic crust [*Swanson et al.;* 1976] the velocities might be slowed down, but this cannot be determined without more work.

3.6 Conclusions

Travel time tomography provides detailed images of the lateral heterogeneity of Kilauea. Using a dense seismograph network and a large number of local events allowed excellent ray coverage of the six major structural entities of the edifice. Resolution and error analyses provided a semi-quantitative method for determining which features are questionable and poorly constrained.

The model suggests a shallow (0–2 km) magma reservoir centered 2 km southeast of Halemaumau caldera, with a plexus of discontinuous open tubes extending to 6 km. This primary conduit and shallow storage area is surrounded by high velocity anomalies representing dense intrusives that form containment boundaries for the reservoir. The rift zones are distinguished by high velocity dike complexes that widen southward to 6 km depth. On a finer-scale the rift zones are more intricate, being strong enough to support a constructional ridge on the surface and weak enough to allow the concentration and intrusion of magma in the subsurface. Small magma pockets are inferred beneath Mauna Ulu, Makaopuhi and Puu Oo on the ERZ.

Intrusive barriers are inferred at Kalalua and Kaliu at shallow levels along the ERZ because of high velocity anomalies in the images. These results are consistent with the lack of significant eruptions or intrusions along the lower ERZ since 1975 [*Decker,* 1987; *Klein et al.,* 1987]. An intrusive barrier is also inferred beneath Mauna Iki on the SWRZ, consistent with the seismicity study of *Klein et al.* [1987]. The

Koae fault system is mainly imaged as a high velocity region related to dike intrusion from the rift zones. The shallow Kaoiki (< 5 km depth) is slow, related to cracks and fractures along its normal faults. The Hilina is imaged as slow to about 6 km due to open fractures and scarps in young subaerial basalts.

Continued work on many aspects of these results would prove useful for refining the three-dimensional structure and dynamics of Kilauea. Inverting data from different time periods, particularly those reflecting the greatest contrast in the eruptive nature of Kilauea, may help define temporal variations in the volcanic subsurface. Details of transient structures from past eruptions would be useful for understanding not only the growth of the tectonic environment of the volcano, but for understanding the origin and differentiation of Hawaiian basalts. This model also lends itself to comparisons with heat flow models that define the sizes and cooling times of magma reservoirs beneath Kilauea. Therefore the velocity anomalies defined by this study should be viewed as a template to be refined and compared with other physical models of a very active, well studied volcano, Kilauea.

Bibliography

Casadevall, T. J., and D. Dzurisin, Intrusive rocks of Kilauea Caldera, *U.S. Geol. Surv. Prof. Pap., 1350,* 377-394, 1987.

Clayton, R. W., and R. P. Comer, A tomographic analysis of mantle heterogeneities from body wave travel times, *Eos, Trans. AGU, 64,* 776, 1983.

Crosson, R. S., and R. Y. Koyanagi, Three-dimensional crust and mantle structure of Kilauea Volcano, Hawaii, *J. Geophys. Res., 84,* 2331-2342, 1979.

Crosson, R. S., and E. T. Endo, Focal mechanisms and locations of earthquakes in the vicinity of the 1975 Kalapana earthquake aftershock zone 1970-1979: Implications for tectonics of the south flank of Kilauea Volcano, Island of Hawaii, *Tectonics, 1,* 495-542, 1982.

Decker, R. W., Dynamics of Hawaiian volcanoes: An overview, *U.S. Geol. Surv. Prof. Pap., 1350,* 997-1018, 1987.

Delaney, P. T., R. S. Fiske, A. Miklius, A. T. Okamura and M. K. Sako, Deep magma body beneath the summit and rift zones of Kilauea Volcano, Hawaii, *Science, 247,* 1311-1316, 1990.

Dieterich, J. H., Growth and persistence of Hawaiian volcanic rift zones, *J. Geophys. Res., 93,* 4258-4270, 1988.

Dieterich, J. H., and R. W. Decker, Finite element modeling of surface deformation associated with volcanism, *J. Geophys. Res., 80,* 4094-4102, 1975.

Duffield, W. A., Structure and origin of the Koae fault system, Kilauea Volcano, Hawaii, *U.S. Geol. Surv. Prof. Pap., 856,* 1-12, 1975.

Duffield, W. A., R. L. Christiansen, R. Y. Koyanagi and D. W. Peterson, Storage, migration and eruption of magma at Kilauea Volcano, Hawaii, 1971–1972, *J. Volcanol. Geotherm. Res., 13,* 273-307, 1982.

Dvorak, J. J., A. T. Okamura and J. H. Dieterich, Analysis of surface deformation data, Kilauea Volcano, Hawaii: October 1966 to September 1970, *J. Geophys. Res., 88,* 9295 – 9304, 1983.

Dvorak, J. J., A. T. Okamura, T. T. English, R. Y. Koyanagi, J. S. Nakata, M. K. Sako, W. T. Tanagawa and K. M. Yamashita, Mechanical response of the south flank of Kilauea Volcano, Hawaii to intrusive events along the rift systems, *Tectonophysics, 124,* 193-209, 1986.

Dzurisin, D. R. Y. Koyanagi and T. T. English, Magma supply and storage at Kilauea Volcano, Hawaii, 1956-1983, *J. Volcanol. Geotherm. Res., 21,* 177-206, 1984.

Eaton, J. P., Crustal structure and volcanism in Hawaii, *Am. Geophys. Soc. Mon. 6,* 13-29, 1962.

Eaton, J. P., and K. J. Murata, How volcanoes grow, *Science, 132,* 925-938, 1960.

Eissler, H. K., and H. Kanamori, A single-force model for the 1975 Kalapana, Hawaii, earthquake, *J. Geophys. Res., 92,* 4827-4836, 1987.

Ellsworth, W. L., and R. Y. Koyanagi, Three-dimensional crust and mantle structure of Kilauea Volcano, Hawaii, *J. Geophys. Res., 82,* 5379-5394, 1977.

Fiske, R. S., and E. D. Jackson, Orientation and growth of Hawaiian volcanic rifts: The effect of regional structure and gravitational stresses, *Proc. R. Soc. London, 329,* 299-326, 1972.

Fiske, R. S., and W. K. Kinoshita, Inflation of Kilauea Volcano prior to the 1967-68 eruption, *Science, 165,* 341-349, 1969.

Fornari, D. J. The geomorphic and structural development of Hawaiian submarine rift zones, *U.S. Geol. Surv. Prof. Pap., 1350,* 125 - 132, 1987.

Furumoto, A. S. and R. L. Kovach, The Kalapana earthquake of November 29, 1975: An intra-plate earthquake and its relation to geothermal processes, *Phys. Earth Planet. Inter., 18,* 197-208, 1979.

Hager, B. H. and R. W. Clayton, Constraints on the structure of mantle convection using seismic observations, flow models, and the geoid, in *Mantle Convection,* edited by W. R. Peltier, pp. 658-763, Gordon & Breach, New York, 1991.

Hill, D. P., Crustal structure of the island of Hawaii from seismic-refraction measurements, *Bull. Seismol. Soc. Am., 59,* 101-130, 1969.

Hill, D. P. and J. J. Zucca, Geophysical constraints on the structure of Kilauea and Mauna Loa volcanoes and some implications for seismomagmatic processes, *U.S. Geol. Surv. Prof. Pap., 1350,* 903-917, 1987.

Hoffmann, J. P., G. E. Ulrich and M. O. Garcia, Horizontal ground deformation patterns and magma storage during the Puu Oo eruption of Kilauea Volcano, Hawaii–Episodes 22-42, *Bull. Volcanol., 52,* 522-531, 1990.

Holcomb, R. T., Eruptive history and long-term behavior of Kilauea Volcano, *U. S. Geol. Surv. Prof. Pap. 1350, 1,* 261-350, 1987.

Jackson, D. B., D. A. Swanson, R. Y. Koyanagi and T. L. Wright, The August and October 1968 east rift eruptions of Kilauea Volcano, Hawaii, *U.S. Geol. Surv. Prof. Pap., 890,* 33 pp., 1975.

Kinoshita, W. K., H. L. Krivoy, D. R. Maby and R. R. MacDonald, Gravity survey of the Island of Hawaii, *U.S. Geol. Surv. Prof. Pap., 475-C,* C114-C116, 1963.

Klein, F. W., A linear gradient crustal model for south Hawaii, *Bull. Seismol. Soc. Am., 71,* 1503-1510, 1981.

Klein, F. W., User's guide to HYPOINVERSE, a program for computers to solve for earthquake locations and magnitudes, *U.S. Geol. Surv. Open File Rep., 89-314,* 1989

Klein, F. W., R. Y. Koyanagi, J. S. Nakata and W. R. Tanigawa, The seismicity of Kilauea's magma system, *U. S. Geol. Surv. Prof. Pap. 1350,* 1019-1186, 1987.

Koyanagi, R. Y., H. L. Krivoy and A. T. Okamura, The 1962 Kaoiki, Hawaii earthquake and its aftershocks, *Bull. Seismol. Soc. Am., 56,* 1317-1335, 1966.

Li, Y., C. H. Thurber, and C. G. Munson, profile of discontinuities beneath Hawaii from S to P converted seismic waves, *Geophys. Res. Lett., 19,* 111-114, 1992.

Lipman, P. W., The southwest rift zone of Mauna Loa: Implications for structural evolution of Hawaiian Volcanoes, *Am. J. Sci., 280-A,* 752-776, 1980.

Moore, J. G., and R. S. Fiske, Volcanic substructure inferred from dredge samples and ocean-bottom photographs, Hawaii, *Geol. Soc. Am. Bull. 80,* 1191-1202, 1969.

Rubin, A. M. and D. D. Pollard, Origins of blade-like dikes in volcanic rift zones, *U. S. Geol. Surv. Prof. Pap. 1350,* 1449-1470, 1987.

Ryan, M. P., The mechanics and three-dimensional internal structure of active magmatic systems: Kilauea Volcano, Hawaii, *J. Geophys. Res., 93,* 4213-4248, 1988.

Ryan, M. P., R. Y. Koyanagi and R. S. Fiske, Modeling the three-dimensional structure of macroscopic magma transport systems: Applications to Kilauea Volcano, Hawaii, *J. Geophys. Res., 86,* 7111-7129, 1981.

Swanson D. A., Magma supply rate at Kilauea Volcano, 1952 – 1971, *Science, 175,* 169–170, 1972.

Swanson, D. A., W. A. Duffield and R. S. Fiske, Displacement of the south flank of Kilauea Volcano: The result of forceful intrusion of magma into the rift zones, *U.S. Geol. Surv. Prof. Pap., 963,* 1-39, 1976.

Thurber, C. H., Seismic detection of the summit magma complex of Kilauea Volcano, Hawaii, *Science, 223,* 165-167, 1984.

Thurber, C. H., Seismic structure and tectonics of Kilauea Volcano, *U.S. Geol. Surv. Prof. Pap. 1350,* 919-934, 1987.

Thurber, C. H., and A. E. Gripp, Flexure and seisimicity beneath the south flank of Kilauea Volcano and tectonic implications, *J. Geophys. Res., 93,* 4271-4278, 1988.

Wilson, L., and J. W. Head III, Nature of local magma storage zones and geometry of conduit systems below basaltic eruption sites: Puu Oo, Kilauea East Rift, Hawaii, example, *J. Geophys. Res., 93,* 14,785-14,792, 1988.

Wright, T. L., Origin of Hawaiian tholeiite: a metasomatic model, *J. Geophys. Res., 89,* 3233 – 3252, 1984.

Yang, X., P. M. Davis, P. T. Delaney and A. T. Okamura, Geodetic analysis of dike intrusion and motion of the magma reservoir beneath the summit of Kilauea Volcano, Hawaii: 1970-1985, *J. Geophys. Res., 97,* 3305-3324, 1992.